Doctoral Dissertation
Doctoral Program in Energy Engineering (36th Cycle)

Optimization of additive manufacturing processes for copper and its alloys

By

Matteo Vanzetti

*****

Supervisor(s):
Prof. F. Bondioli, Supervisor
Prof. D. Manfredi, Co-Supervisor

Doctoral Examination Committee:
Prof. R. Casati, Politecnico di Milano
Prof. P. Rizzi, Università degli studi di Torino

Politecnico di Torino
2024

Declaration

I hereby declare that the contents and organization of this dissertation constitute my own original work and does not compromise in any way the rights of third parties, including those relating to the security of personal data.

Matteo Vanzetti

2024

* This dissertation is presented in partial fulfillment of the requirements for **Ph.D. degree** in the Graduate School of Politecnico di Torino (ScuDo).

Acknowledgment

I would like to express my gratitude to Prof. Federica Bondioli for providing me with the opportunity to work within this dynamic research group, for guiding me towards a profoundly significant research topic, for her meticulous planning of research activities, and for her insightful interpretation of experimental results. I am grateful for the time she dedicated to engaging in discussions, exchanging thoughts, and fostering new stimulating ideas. Special thanks are also due to Prof. Elisa Padovano for her invaluable assistance across various fields throughout my entire PhD journey. I am indebted to Diego Manfredi for generously sharing his knowledge and for his unwavering encouragement over the years.

I express my sincere appreciation to the Istituto Italiano di Tecnologia of Torino for their support in my research endeavors. I am deeply grateful to Prof. Luke Brewer of the University of Alabama for granting me the opportunity to join his research group and for allowing me to delve into an extensive characterization of metal powders. I would like to acknowledge Dr. Lorena Perez Andrade of the University of Alabama for her assistance during my visiting period at her university and for her support in my research activities.

Throughout these three years, I have had the privilege of working alongside many friends and colleagues. I extend my gratitude to Francesco, Michele, Alessandro, Stefano, Mirko, Samuele, Daniele, Matteo, Giorgia, Niccolò, Vincent, Jayant, and Josip for their support in our research endeavors and for the enjoyable moments we shared together. I am thankful to Alberta, Giulio, Giovanna, and Luca

for their assistance across various situations and fields. My heartfelt appreciation goes to Alessia for her unwavering support throughout this journey. Lastly, I wish to express my deepest gratitude to my friends and family, whose kindness, encouragement, and inspiration have been constant pillars throughout all my studies.

Abstract

In recent times, the utilization of additive manufacturing technologies has risen to prominence as a revolutionary method for fabricating metallic components, presenting unmatched design freedom and efficiency. Among these technologies, powder bed fusion methods stand out as particularly compelling and extensively researched. However, a notable limitation of these technologies arises from the restricted availability of commercial alloys, primarily tailored for conventional casting, which poses challenges for seamless adaptation to these groundbreaking processes. Notably, pure copper and copper alloys present a significant challenge when processed using powder bed technologies due to their inherent reflectivity to optical power sources such as lasers. This thesis explores the processing of pure copper and the CuNi2SiCr alloy via Electron Beam Powder Bed Fusion (EB-PBF) and Laser Powder Bed Fusion (L-PBF) methods, optimizing the process parameters and subsequently investigating their microstructural evolution, mechanical properties, and post-processing heat treatment optimization.

Initially, the processability of pure copper through the EB-PBF process was investigated. After the process parameters optimization, full dense samples were successfully achieved. Following this, comprehensive characterization of the produced samples was conducted, focusing on microstructural analysis, phase composition, and mechanical properties evaluation.

Subsequently, the thesis shifted its focus to the CuNi2SiCr alloy, investigating its processability across various L-PBF machines. Specifically, three machines were employed for this investigation: two equipped with a red laser source (with low and medium power sources), and one equipped with a green laser source. The

optimization of process parameters was conducted across all machines, yielding varying outcomes. Samples produced using the low-power red laser exhibited incomplete densification, attributed to insufficient laser power. Conversely, the medium-power red laser and green laser machines facilitated the production of fully dense samples. Afterwards, all optimized samples underwent comprehensive characterization resulting in very similar microstructure, depending on the specification of the machine, and comparable mechanical properties.

Furthermore, two distinct post-processing heat treatments tailored for the precipitation hardening of the CuNi2SiCr alloy, fabricated via the L-PBF process, were optimized. The first heat treatment, involving direct aging, yielded comparable performance to the second, which comprised a short T6 heat treatment.

Moreover, the feasibility of employing the hot isostatic pressing (HIP) process to densify the incompletely dense samples was evaluated. Concurrently, this process served as the initial step of the optimized short T6 heat treatment. However, it was observed that the HIP process was unable to achieve complete densification within the short timeframe required for the short T6 treatment. Nevertheless, it was determined that extending the duration of the HIP process could potentially lead to the complete densification of the samples.

Finally, suggestions for future development and analyses were proposed.

Contents

List of Figures

List of Tables

Chapter 1

Introduction

This thesis explores the fabrication of pure copper and the CuNi2SiCr alloy using Electron Beam Powder Bed Fusion (EB-PBF) and Laser Powder Bed Fusion (L-PBF) techniques. It centers on refining process parameters, analyzing their effects on microstructural development and mechanical properties, and optimizing post-processing heat treatments. Copper and its alloys are extensively researched due to their exceptional physical properties, especially their high electrical and thermal conductivity. However, processing copper and its alloys via powder bed fusion technologies poses challenges, primarily due to the interaction between the optical power source and copper's high reflectivity, but also because of its high thermal conductivity, which dissipates heat very quickly. Moreover, the unique microstructure achieved through additive manufacturing processes offers opportunities to tailor specific heat treatments to enhance mechanical and electrical properties. The thesis is structured as follows:

- Chapter 2 begins by introducing fundamental concepts regarding additive manufacturing processes. Then, the focus shifts to metal additive manufacturing, with particular attention given to powder bed technologies. At the end of this chapter, defects in laser powder bed fusion and electron beam powder bed fusion are explored in detail.
- Chapter 3 examines the current state of art concerning the properties and classification of copper and copper alloys. Special attention is dedicated to the CuNiSi alloy, which holds significant relevance for this thesis.

- Chapter 4 assesses the current state of art in additive manufacturing of copper and copper alloys, with a particular focus on various powder bed fusion technologies.
- Chapter 5 reports the materials, process technologies, and characterization methods utilized throughout the experimental work.
- Chapter 6 thoroughly examines and discusses the experimental results obtained from the processing of pure copper using electron beam powder bed fusion (EB-PBF).
- Chapter 7 meticulously explores and discusses the experimental findings derived from the processing of CuNi2SiCr using laser powder bed fusion (L-PBF). The chapter is divided into five sections, focusing on low-power and medium-power red laser, as well as green laser. The final two sections are dedicated to the study of a tailored heat treatment for this alloy and the possibility of densifying the porous samples using the hot isostatic pressing (HIP) process.
- Chapter 8 draws conclusions from the outcomes obtained through the conducted work and suggests potential ideas for future research directions.

Chapter 2

Additive Manufacturing

Additive manufacturing (AM), also known as 3D printing, is a groundbreaking manufacturing process that has revolutionized the way it is possible to produce objects and parts.

AM is defined by ASTM F2792-12a as "*a process of joining materials to make objects from 3D model data, usually layer upon layer, as opposed to subtractive manufacturing method*ologies" [1].

This technology has opened up endless possibilities, allowing to fabricate complex geometries, intricate designs, and custom-made components with unprecedented ease and efficiency. The roots of additive manufacturing can be traced back to the 1980s when early experiments with layer-by-layer fabrication began. At the core of additive manufacturing lies the digital design, a crucial starting point that defines the very essence of what can be realized. Designers, engineers, and artists use powerful computer-aided design (CAD) software to construct complex virtual models, which serve as the blueprints for the physical objects that will later make. The seamless transition from digital concept to tangible reality allows for rapid prototyping, iterative design improvements, and unparalleled levels of customization to meet the diverse needs of various industries. Over the decades, this innovative technology has matured and diversified, finding applications in a wide range of industries, including aerospace, automotive, healthcare, jewelry, consumer goods, and more [2,3]. Its versatile nature and ability to work with various materials, such as polymers, metals, ceramics, composites and

even biomaterials, have led to the creation of diverse products, from small-scale prototypes to large-scale functional parts [4].

The following chapters of this dissertation will offer a comprehensive overview of the current Metal Additive Manufacturing (MAM) beam-based landscape and the state of the art of pure copper and its alloys. A particular focus was placed on Laser Powder Bed Fusion (L-PBF) and Electron Beam Powder Bed Fusion (EB-PBF) technologies used in this research to process these materials. Within this context, the investigation delves into the optimization of process parameters and post-processing treatments to enhance the mechanical and physical properties of these alloys.

2.1 Additive Manufacturing process chain

The product development process involving additive manufacturing machines follows a specific procedural sequence. The additive manufacturing process chain is shown in Figure 1 and encompasses several steps from concept to final product production. Each step plays a crucial role in the successful creation of a 3D- printed object.

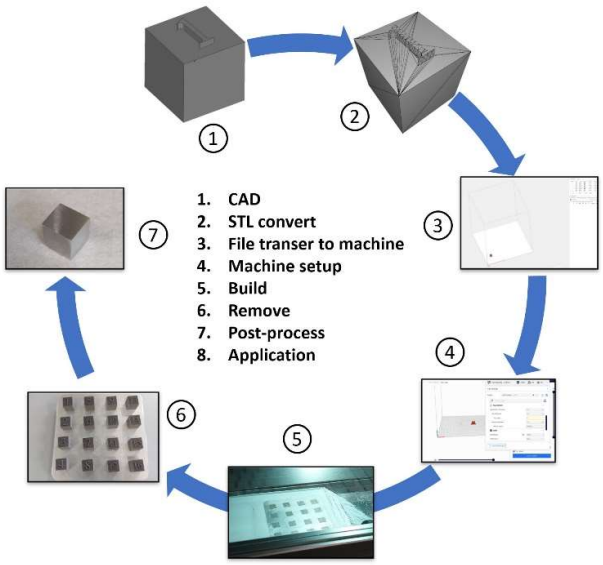

Figure 1. General Additive Manufacturing process chain [internal repository].

Initially, a CAD model is created to represent the desired geometry of the part intended for printing. This CAD model can be obtained through various methods, such as a designer using CAD software or by 3D scanning an existing part. The second step represents the conversion of this model in a STL file format. STL is the standard format for this application and provides a straightforward method to describe a CAD model solely in terms of its geometry [5]. It achieves this by approximating the model's surfaces using a collection of triangular facets. After creating the STL file, it can be directly transmitted to the selected AM machine. Each AM machine will have specific setup parameters tailored to its unique machine or process. During this stage, the slicing operation occurs, where the model is divided into thin slices (layers) with the specified thickness (layer thickness). Upon completing the aforementioned steps, the process transitions to the automated building phase, during which the layer-based manufacturing occurs. In this phase, all AM machines follow a comparable layering sequence, which involves a height-adjustable platform or deposition head, material deposition or spreading mechanisms, and the formation of each layer's cross-section. Finally, when the building process concludes, the part needs to be taken off the building platform and could undergo post-processing steps, such as removal of support structures, surface polishing, application of coatings and heat treatment [6].

2.2 Metal Additive Manufacturing beam-based processes

Metal Additive Manufacturing (MAM) encloses a variety of production processes classified based on the mechanism used to join material layers, the nature of the raw material, and the method of feeding the machines. The energy sources commonly employed in MAM beam-based processes include lasers or electron beams. Regarding the raw material nature, it is typically in powder form, although less commonly, it may be in wire form. Additionally, the primary technologies for supplying raw material in MAM beam-based are categorized as powder-bed, blown powder, and wire-feed processes. These processes will be briefly introduced in the next pages and a schematic of the main MAM beam-based technologies is illustrated in Figure 2.

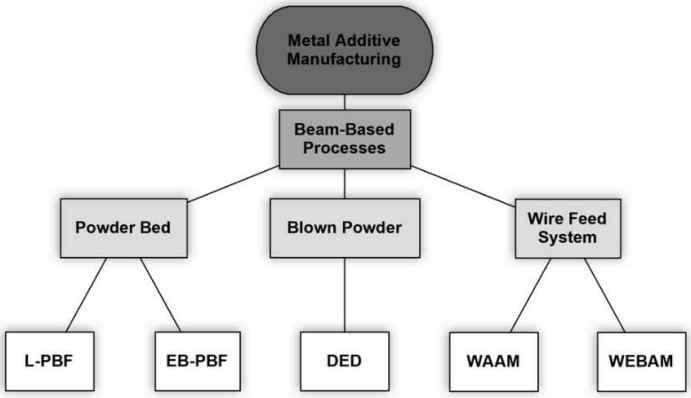

Figure 2. Overview of MAM beam-based technologies [internal repository].

2.2.1 Blown powder

Blown powder technology comprises the process of layer-by-layer object construction through the deposition of powdered material onto a substrate or onto previously added layers or parts [7]. This process employs a powder delivery system that propels the powdered material onto the build area and the schematic representation is depicted in Figure 3.

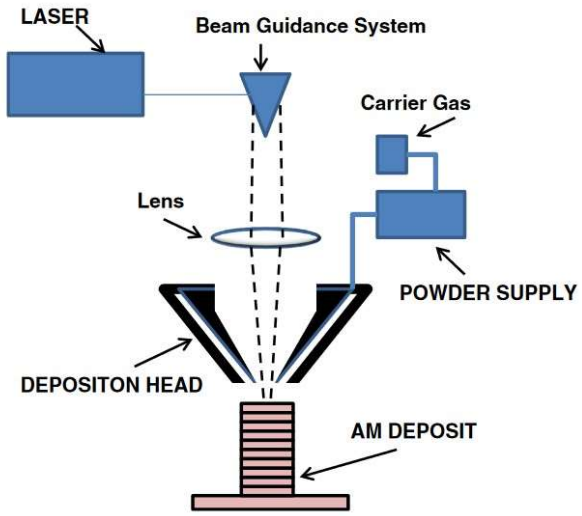

Figure 3. Illustration depicting the schematic of a blown powder process [8].

The powdered material is stored in a reservoir, and it is delivered to the build area using a carrier gas or another suitable medium. The delivery mechanism can involve a nozzle or a powder dispenser that directs the flow of powder particles toward the target substrate. An energy source, typically a laser or an electron beam, is used to melt or sinter the deposited powder. The energy source is precisely controlled to fuse the powder particles together and adhere them to the previous layers or substrate. The process is repeated iteratively, with each layer of powder being deposited, melted, and solidified before the next layer is added. This layering process continues until the desired object is fully constructed. The primary method employing this approach is known as Direct Energy Deposition (DED), and its advantages comprise a sizable build volume, swift building rates, and the ability to effectively repair damages [8].

2.2.2 Wire feed system

Wire-Feed Additive Manufacturing is an advanced manufacturing technique that involves the deposition of material layer by layer employing a metal wire as the feeding material. Depending on the energy source used for metal deposition, the wire-feed process can be categorized into three groups based on the energy source: laser-based, arc welding-based, and electron beam-based. A schematic drawing of the wire-feed process is reported in Figure 4.

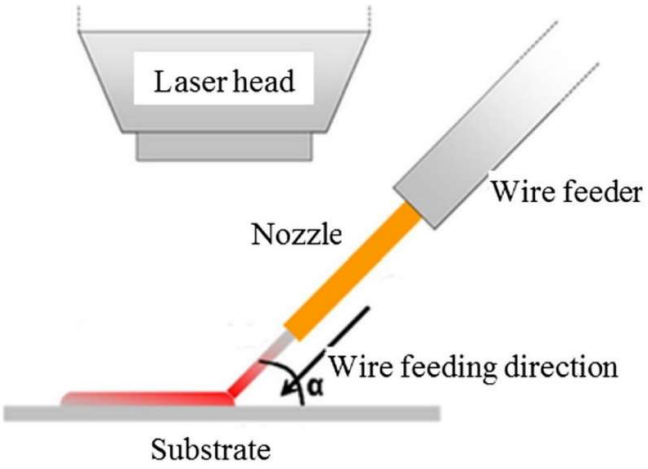

Figure 4. Schematic drawing of the wire-feed process [9].

The additive manufacturing system, which includes a robotic arm, CNC machine, is prepared with the necessary components such as the wire feeder, energy source, and control systems. The process begins with the deposition of the initial layer of material. This involves the use of a "head," which comprises an energy source and a wire feeder. The wire is melted using the energy source and is then accurately deposited onto the workpiece, adhering to the layer beneath it. The motion of the head and workpiece is carefully controlled to create the desired shape and dimensions. The process is repeated for each subsequent layer, gradually building up the object's shape. This process boasts a remarkable material utilization efficiency of up to 100%, ensuring that all the metal material utilized is deposited into the component. As a result, it proves to be an environmentally friendly and safer process, with operators being spared exposure to dusty environments, unlike powder-bed or blown powder processes. The wire-feed process demonstrates a significantly higher deposition speed, surpassing 2500 cm^3/h (330 g/min for stainless steel), enabling both elevated deposition rates and exceptional resolution. It holds potential for fabricating large-sized components with moderate complexity, such as flanges or rigid panels. Nonetheless, this process encounters certain challenges in component design due to residual stresses, leading to distortion of the final part. It is also characterized by relatively lower precision caused by the "stair step" effect and a less smooth surface finish [9]. WAAM (Wire Arc Additive Manufacturing) and WEBAM (Wire Electron Beam Additive Manufacturing) belong to this category [10].

2.2.3 Powder bed

Powder bed technology, also known as powder bed fusion or powder-based additive manufacturing, involves the layer-by-layer creation of objects using a powdered material [8]. There are a few different variations of powder bed technology, but they all share some common principles, and their scheme is shown in Figure 5.

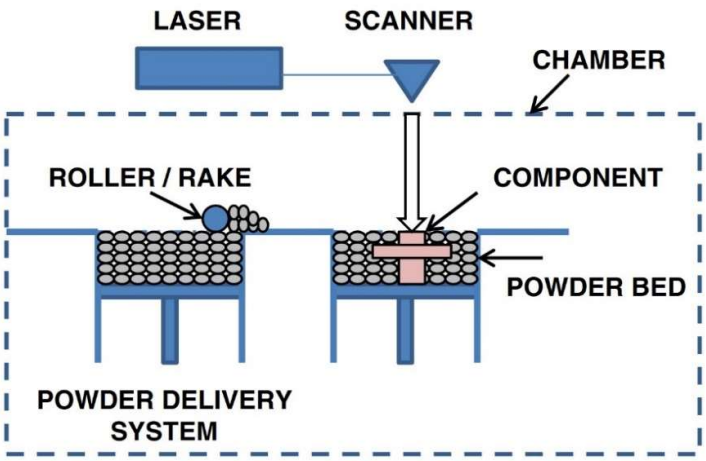

Figure 5. Scheme of a powder bed process [8].

The process begins with a thin layer of powdered material evenly across the build platform. An energy source, such as a laser or an electron beam, is used to locally melt or sinter specific areas of the powder in a pattern that corresponds to the cross-section of the object being created. Once a layer is completed, the build platform is lowered by a fraction of the layer's thickness, and a new layer of powder is spread on top using a powder leveling roller [11]. The energy source then works on this new layer to fuse it with the previous one. This process is repeated until the entire object is fully constructed.

The main powder bed processes can be classified into two categories depending on the energy source employed to melt the powder bed: electron beam or laser beam. The Electron Beam Powder Bed Fusion (EB-PBF) method falls within the first category, utilizing a high-energy electron beam within a high vacuum environment to achieve powder bed melting. Conversely, the Laser Powder Bed Fusion (L-PBF) process employs a laser beam to selectively and locally melt the powder bed in an inert environment. Powder bed technology enables the creation of highly detailed and complex geometries with exceptional accuracy. The layer-by-layer approach allows for intricate features that might be challenging or impossible to achieve through traditional manufacturing methods. Moreover, it is inherently more material-efficient than traditional machining processes and the unused powder can be collected, sieved, and reused for subsequent builds, minimizing waste and material costs [12].

2.3 Laser Powder Bed Fusion (L-PBF)

Laser Powder Bed Fusion (L-PBF) operates on the basis of a powder bed process, where metal powder is spread in thin layers. These layers typically have a thickness (l_t = *layer thickness*) ranging from 20 µm to 100 µm, covering a building platform with dimensions that currently range from 50 x 50 mm^2 to 800 x 400 mm^2 [11]. A schematic representation of a standard L-PBF machine and its process cycle is provided in Figure 6.

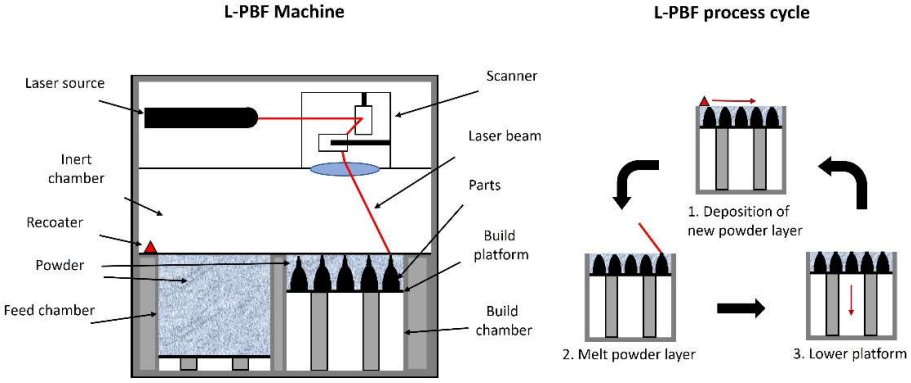

Figure 6. Schematics of an L-PBF machine and its process cycle [11].

The powder, normally ranging in size from 20 µm to 63 µm, is introduced through a tank located adjacent to the work area, in the feed chamber [13]. To ensure an even distribution of the powder, a recoater blade is employed. Guided by a scanner, a laser beam with a optimized power (P = *power*) is precisely directed on the previously deposited powder layer using a scanning speed (v = *scanning speed*) of up to 15 m/s. Considering the cross-sectional area of the component, the powder experiences precise laser irradiation in the x-y plane, leading to its melting. Typically, the arrangement of individual molten paths adheres to a predefined pattern, referred to as the scanning strategy. These molten tracks are deliberately overlapped, maintaining a specific distance known as the "hatch distance" (h_d = *hatching distance*). The energy applied to the volume is carefully modulated to achieve the desired melting effect to obtain the higher relative density. The equation (0.1) computes the volumetric energy density (VED) [14]. When this energy is applied to the powder layer, it not only causes the fusion of the exposed material, but also affects neighboring areas due to heat conduction.

$$VED = P/(v * h_d * l_t) \qquad \left[\frac{J}{mm^3}\right] \tag{0.1}$$

Upon the melt solidification, the individual molten tracks and the previously solidified layer beneath become fused together. Following the selective exposure of the powder bed to the laser beam, the build plate is lowered. Subsequently, a fresh powder layer is deposited, and the process of melting the newly added powder layer is repeated. These three steps are reiterated until the completion of the part. Once finished, unmelted metal powder can be sieved and reutilized in subsequent L-PBF processes [11].

2.3.1 Laser sources

Laser sources commonly utilized in L-PBF predominantly involve single-mode fiber lasers that emit radiation in the continuous wave mode. Generally, these laser sources have a power level up to 1 kW and emit radiation with a wavelength falling within the range of 1060 nm to 1080 nm in the near-infrared spectrum (red laser) [15]. Varying the laser wavelength, it is possible modify the absorptivity of the powder bed, leading to a subsequent adjustment in the quantity of energy transmitted for the purpose of melting [4,16]. In recent years, machinery has been upgraded with green laser sources operating at a wavelength approximately of 515 nm. This advancement aims to enhance absorption for materials such as copper, its alloys and gold, which traditionally exhibit low absorbance levels when exposed to red lasers [17,18].

2.3.2 Scanning strategies

The scanning strategy includes the geometric arrangement of laser paths within the Laser Powder Bed Fusion (L-PBF) process. Figure 7 offers an illustration showcasing different scanning strategies employed in L-PBF [19].

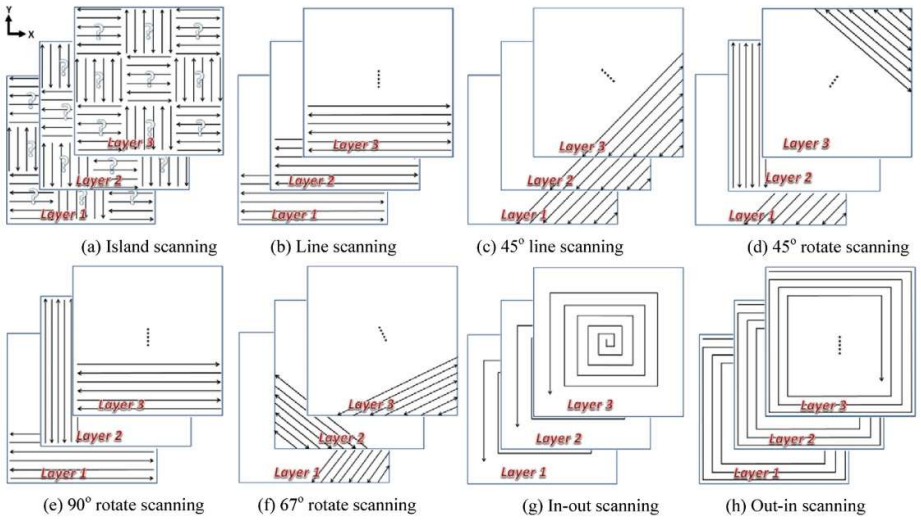

Figure 7. Example of scanning strategies in L-PBF technique [19].

Figure 7a illustrates the "island strategy." This method involves partitioning the cross-section of the component into uniform regions of discrete dimensions. Within each of these designated "islands," the laser beam is directed to selectively melt the powder bed, shaping it according to the desired form. The laser track direction is altered with respect to the previous layer. Other scanning strategies use a continuous scanning line, wherein the laser tracks maintain a fixed direction between each powder layer (Figure 7b-c), change direction at a specified angle (Figure 7d-f) or follow an in-out or out-in spiral pattern (Figure 7g-h). The scanning strategy with a rotation of 67° (Figure 7f) is one of the most used in L-PBF process. Different scanning strategies give rise to distinct thermal gradients and temperature distributions [5], thereby exerting an influence on material densification, microstructure, and residual stresses within the material [20–22]. Precise overlap between successive laser tracks facilitates the remelting of consolidated material, diminishing internal porosity, enhancing inter-layer adhesion, elevating material temperature, and consequently reducing thermal residual stresses. Notably, rotated scanning strategies outperform unidirectional ones in reducing porosity and residual stresses within final components due to superior overlap between consecutive layer laser tracks[5,23,24].

2.3.3 Support structures and preheated build plate

The constructed part is affixed to a build plate, often connected by support structures. These support structures take the form of lattice-like frameworks,

serving to dissipate heat and secure the part within the powder bed. They are particularly crucial for maintaining the stability of horizontally oriented and overhanging surfaces of the part. This arrangement effectively prevents deformation of the part. These support structures must be removed in the later stages of finishing the part. In addition to support structures, pre-heating of the build plate can be employed to mitigate part distortion by reducing thermal gradients. This practice leads to diminished residual stresses that can arise during the L-PBF process [25].

2.3.4 Protective atmosphere

The L-PBF process is conducted within a sealed process chamber, where an inert gas atmosphere is continually maintained to keep residual oxygen content below 0.1% [26]. Nitrogen or argon is introduced into the chamber to prevent undesired interactions between the metal powder and its surroundings while safeguarding the molten material. Additionally, by directing an inert gas flow around the work area, byproducts of the process like fumes and spatter are eliminated [27].

2.4 Electron Beam Powder Bed Fusion (EB-PBF)

Electron Beam Powder Bed Fusion (EB-PBF) is a technique that unfolds in a manner analogous to the L-PBF process and its scheme and process cycle are depicted in Figure 8.

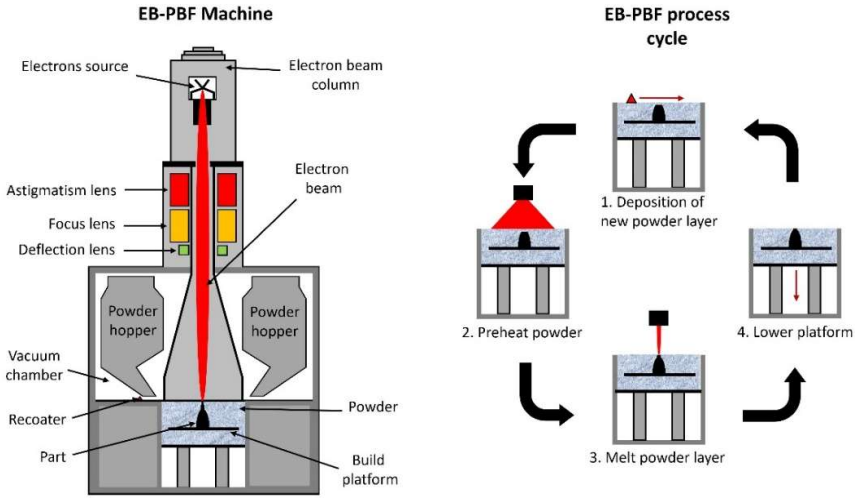

Figure 8. Schematics of an EB-PBF machine and its process cycle [28].

In EB-PBF, metal powder, normally ranging in size from 45 to 106 µm, is fed from a hopper and evenly distributed across a build plate using a recoater blade [29,30]. Ordinarily, the layer thickness (l_t) of the powder ranges from 50 µm to 200 µm. The build plate typically measures 200 x 200 mm^2 in the x-y direction or 350 mm in diameter [11]. EB-PBF employs an electron beam as the energy source to melt the powder, following the required pattern. This electron beam, originates within an electron beam column, undergoes acceleration with a voltage of 60 kV, is focused by electromagnetic lenses, and is directed through a magnetic scan coil to precise positions on the build plate's x-y plane [31]. The electron beam's power (P), focus, and scanning speed (v) are chiefly determined by the selected beam current, focus offset, and speed function, respectively. Initially, metal powder is spread in thin layers using a recoater blade. Subsequently, the powder bed undergoes pre-heating through a defocused beam that systematically scans the surface of the powder bed multiple times. To ensure the full fusion of the metal powder, the beam current and scan speed are typically reduced, compared to the parameters used during the preheating step, employing a specific scanning strategy in the subsequent melting scan. Following the selected scanning strategy, molten tracks are deliberately overlapped, maintaining a specific distance known as the "line offset" (l_o = *line offset*). As in the L-PBF technology, the volume energy density (equation (0.2)) is meticulously controlled to attain the intended melting effect and achieve a greater relative density.

$$VED = P/(v * l_o * l_t) \qquad \left[\frac{J}{mm^3}\right] \tag{0.2}$$

Once the melting phase is completed, the build plate is lowered, and a new layer of metal powder is introduced. This cycle, involving powder spreading, scanning the uppermost layer, and lowering the build plate, is reiterated until the part fabrication is accomplished. Once finished, as aforementioned for L-PBF process, unmelted metal powder can be sieved and reutilized [11].

2.4.1 Electron beam sources

Electrons can be generated through direct heating (resistive heating) or indirect heating (laser heating) of the cathode. This cathode has a with a V-shaped tip, and it is made of either tungsten or LaB_6. In comparison to tungsten filament, the LaB_6 cathode exhibits a notably higher current density per unit surface area due to its considerably lower work function and operating temperature. The electron beam

produced using LaB_6 is known for its enhanced stability. While the diameter of a 60 kV beam generated with a tungsten filament can significantly increase with beam power, the spot size of the electron beam emitted from LaB_6 experiences only a slight increase with beam power. Furthermore, single-crystalline LaB_6 is associated with a higher price and longer lifespan compared to a tungsten filament [31].

2.4.2 Protective atmosphere

The operational environment for the EB-PBF process is a vacuum with a pressure below 10^{-2} Pa [32]. However, during the melting process, helium is introduced into the work area to elevate the pressure inside the system to around 1 Pa. This serves to prevent electrical charging of the powder particles, enhance heat conduction, and improve the cooling of the molten material [30].

2.5 Defects in L-PBF and EB-PBF technologies

All additive manufacturing processes, including L-PBF and EB-PBF processes, offer many advantages in their use, but at the same time, they also present challenges. The results in terms of relative density and the success in producing a part depend on the optimization of process parameters. If not properly optimized, the produced parts will not be completely dense and will exhibit defects. Table 1 lists the main defects that can occur during the production of parts using L-PBF and EB-PBF, which will be discussed in the following paragraphs.

Table 1. Defects of AM process and corresponding technology.

Defects	AM Technology
Balling	L-PBF
Porosity	L-PBF, EB-PBF
Keyhole	L-PBF, EB-PBF
High Surface Roughness	L-PBF, EB-PBF
Loss of alloying elements	L-PBF, EB-PBF
Oxide inclusion	L-PBF, EB-PBF

2.5.1 Balling

The balling phenomenon (Figure 9) arises from two primary factors: splashing of molten metal and the molten metal inadequate ability to wet a surface. Balling behavior is manifests when liquid molten metal has limited contact with a substrate or base material. According to the principle of minimizing surface energy, the liquid metal forms small spherical droplets due to its surface tension. The presence of the balling region negatively impacts surface finish, diminishing its quality. Additionally, it leads to numerous pores within the processed component and has the potential to harm the recoater, consequently affecting the even distribution of the subsequent layer [33,34].

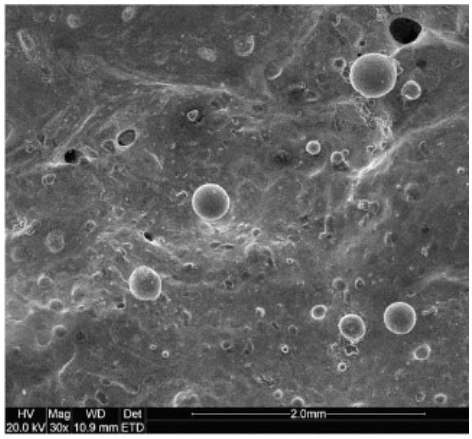

Figure 9. SEM micrograph of an example of balling defect [34].

2.5.2 Porosity

In the L-PBF and EB-PBF processes, pores can be categorized into three types: lack of fusion, gas pores, and shrinkage pores [33,35–37]. Lack of fusion defects (Figure 10) arise from insufficient laser energy density and incomplete overlap of adjacent molten pools. This deficiency results in inadequate heat penetration, leaving the top layer of already melted and solidified material unmelted, leading to poor bonding with subsequent layers [33,38]. Gas pores form when trapped gases within the powders are released, potentially disrupting the scanning path in a hazardous manner. As the process continues and cavities develop, the forces exerted by the fluid balance with vapor pressure, causing liquid phases to collapse and form pores. Gas pores typically exhibit a spherical shape due to the influence of surface tension, causing gas bubbles to adopt this form [33,39,40]. On the other hand,

shrinkage pores predominantly emerge during the solidification phase when an insufficient amount of molten metal is generated [41].

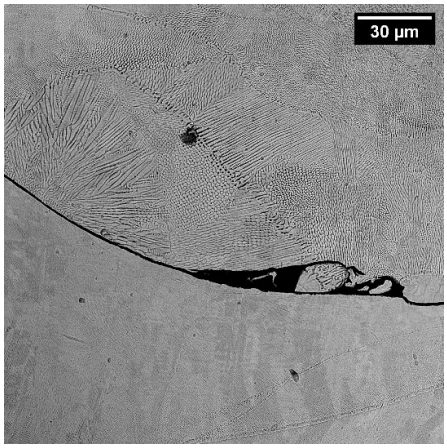

Figure 10. SEM BSE micrograph of an example of lack of fusion defect [internal repository].

2.5.3 Keyhole

Keyholing behavior is a defect that occurs in L-PBF process, when extremely high laser energy density is applied. This phenomenon is associated with the evaporation of elements within the molten material, resulting in the generation of gas within the meltpool. Some of this gas may become trapped by the solidification front of the meltpool, ultimately leading to significant porosity in the finished part [42–44].

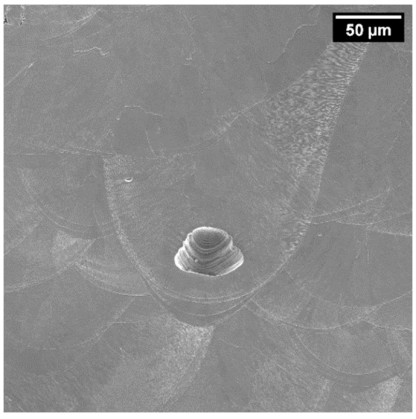

Figure 11. SEM SE micrograph of an example of keyhole defect [internal repository].

2.5.4 Surface roughness

Surface roughness is influenced by various factors. One such factor is oxidation, which occurs due to the presence of atmospheric gases and the adhesion of partially melted powders to the surface of the part [45]. Another factor is the continuous presence of unused powders that either linger in the process area or persist within the powder bed itself. These unused powders can attach to the surface increasing the roughness. The average size of the roughness resulting from particles adhered to the surface is nearly of the same order of magnitude as the diameter of the powder particles. For these reasons, the surface finish of L-PBF samples (Figure 12a) is better than that of EB-PBF samples (Figure 12b), primarily because of the particle size range used in both processes, which are 20-63 micrometers and 50-106 micrometers, respectively. Another factor that affects the surface roughness of parts in PBF technologies is the "staircase" effect, which is associated with the number of layers. As the layer thickness increases, the surface roughness also increases [33,46].

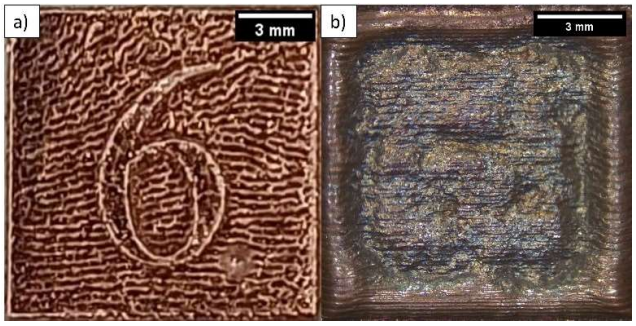

Figure 12. Different surface roughness in a) L-PBF and b) EB-PBF samples [internal repository].

2.5.5 Loss of alloying elements

During the PBF processes, the high temperatures involved in the process lead to the evaporation from the meltpool of highly volatile metals, such as Al, Mg, Zn, and similar elements. When the laser interacts with these metals, their elevated vapor pressure and low boiling points result in their vaporization [47]. The temperature within the meltpool significantly overcome the boiling points of these elements. This vaporization process not only modifies the composition of the produced part but also impacts its mechanical properties [33,48].

2.5.6 Oxide inclusion

The oxide inclusion is one of the certain defects that adversely affects the properties of the manufactured part. If the oxide inclusion generates a oxide layer, this oxide layer can affects bonding and contribute to the balling phenomenon. The presence of an oxide layer in the pre-solidified layer hampers the distribution of the new layer and impedes interlayer bonding. Consequently, this leads to inadequate densification [33].

Chapter 3

Copper and copper alloys

Copper and copper alloys constitute a significant category within the group of commercial metals, securing their place as the third most produced and consumed metals after steel and aluminum. Their widespread utilization can be attributed to a lot of remarkable properties, including exceptional electrical and thermal conductivity, remarkable resistance to corrosion, ease of malleability, satisfactory strength, and commendable fatigue resistance. Moreover, their inherent nonmagnetic nature adds to their allure. The versatility of these materials is further demonstrated by their seamless compatibility with soldering and brazing processes, along with the potential for welding through diverse techniques like gas, arc, and resistance methods. In applications where aesthetics matter, readily available standard alloys boast specific colors, making them ideal for decorative components. The manipulability of copper alloys extends even to their surface characteristics, as they can be polished, buffed, and manipulated to achieve nearly any conceivable texture and level of luster. Beyond this, their adaptability shines through processes like plating, organic substance coating, and chemical coloring, which collectively broaden the spectrum of attainable finishes and appearances.

Copper readily forms alloys with several key elements including aluminum, nickel, silicon, tin, and zinc, which are frequently employed to tailor its properties. Additionally, trace amounts of various other elements and metals can be integrated to enhance specific material traits, ranging from heightened resistance to corrosion to improved machinability. The spectrum of copper and its alloy derivatives is

categorized into nine primary groups, each distinguished by distinct compositional features and utilization profiles [49]. These pivotal groupings comprehend:

- Pure copper and coppers, which contain a minimum of 99.3% Cu
- High-copper alloys, incorporating alloying elements up to 5%
- Copper-zinc alloys (brasses), composed of up to 40% Zn
- Copper-tin alloys (phosphor bronzes), containing up to 10% Sn and 0.2% P
- Copper-aluminum alloys (aluminum bronzes), including up to 10% Al
- Copper-silicon alloys (silicon bronzes), containing up to 3% Si
- Copper-nickel alloys, containing up to 30% Ni
- Copper-zinc-nickel alloys (nickel silvers), which contain up to 27% Zn and 18% Ni
- Special alloys, strategically infused with alloying elements to enhance specific properties or characteristics, such as improved machinability

The following paragraphs of this chapter will provide an overview of the materials used in this research.

3.1 Pure copper

Pure copper stands as an exemplary model of extraordinary electrical conductivity, showcasing an impressive magnitude of 58 MS/m [50]. This places copper in a prominent echelon among materials renowned for their aptitude in facilitating electrical conduction, a ranking surpassed only by silver. The evaluative benchmark for electrical conductivity derives its foundation from copper's standard, established at 100%. This calibration subsequently facilitates the articulation of alternative materials electrical conductivities as relative percentages of the International Annealed Copper Standard (IACS). Notably, beyond its electrical prowess, pure copper also demonstrates a notable proficiency in heat conduction, with a thermal conductivity value of 401 W/m*K [51]. These and other characteristics of copper are summarized in Table 2.

Table 2. Physical properties of pure copper at 20 °C.

Properties	Pure copper	Unit
Density	8952 [49]	[Kg/m^3]
Electrical conductivity	58 [50]	[*MS/m*]
Thermal conductivity	401 [51]	[*W/m*K*]
Hardness	35-65 [52]	[*HV*]
Yield strength	≤120 [52]	[MPa]
Tensile strength	≥200 [52]	[MPa]
Elongation at break	≥35 [52]	[%]

3.1.1 Pure copper grades

Within the realm of commercially pure copper, several grades exist, primarily distinguished by their emphasis on achieving heightened electrical conductivity. The paramount variants include tough pitch copper, deoxidized copper, and oxygen-free electronic copper. Their respective compositions and physical properties are detailed in Table 3. The differentiation of commercially pure copper grades is closely intertwined with the refining methods employed. Tough pitch copper exhibits a copper content exceeding 99.00 wt% and an oxygen content of approximately 0.04 wt%. Its attributes render it a versatile choice for applications such as electrical wire and cable, as well as roofing and architectural trim. Deoxidized copper boasts a copper content of 99.90 wt% and a scant oxygen content of 0.01 wt%. Additionally, it contains trace amounts of phosphorous, typically ranging from 0.004 wt% to 0.012 wt%. This inclusion arises from the utilization of phosphorous during production, aimed at diminishing oxygen content, but regrettably, it leads to a reduction in electrical conductivity. Deoxidized copper primary application lies in serving as the standard material for household water

tubing. Oxygen-free electronic copper emerges as the purest form, featuring a copper content surpassing 99.99 wt% and an oxygen content lower than 0.001. Its unparalleled purity designates it for applications necessitating supreme electrical conductivity, exemplified by its conductivity level of no less than 100% IACS [49].

Table 3. Oxygen content and properties of three commercially pure coppers [49].

	Copper content (*wt%*)	**Oxygen content (*wt%*)**	**Others (*wt%*)**	**Electrical conductivity at 20 °C (*MS/m*)**
Though pitch copper	≥99.00 (Cu + Ag)	0.04–0.05	-	58.6
Deoxidized copper	99.90	0.01	0.004-0.012 P	49.3
Oxygen-free electronic copper	≥99.99	≤0.001	-	58.6

3.1.2 Effect of impurities on conductivity

Disruptions, in the regular arrangement of the copper lattice, result in the scattering of electrons, leading to a reduction in electrical conductivity. Solute elements introduced into the copper lattice, due to their distinct atomic sizes, create localized regions of elastic strain, consequently contributing to a reduction in conductivity. This stands as the predominant impact of impurities. Nonetheless, if the secondary element forms a separate phase with the copper, the presence of this secondary phase generally leads to a reduction in conductivity, primarily due to the reduced volume of copper available for current conduction. This effect, however, is not as significant as when the secondary element exists in solid solution within the copper lattice. Figure 13 illustrates the impact of alloying elements on electrical resistivity. Notably, even minute quantities of impurities can result in a substantial decrease the electrical conductivity. Of these influential elements, phosphorus stands out prominently [49].

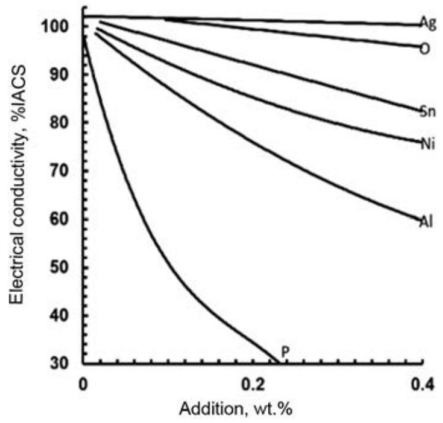

Figure 13. Effect of alloying element on electrical conductivity of pure copper [15].

3.2 Copper-nickel alloys

Copper and nickel occupy neighboring positions in the periodic table of elements and display complete miscibility both in their liquid and solid forms as shown in the phase diagram in Figure 14.

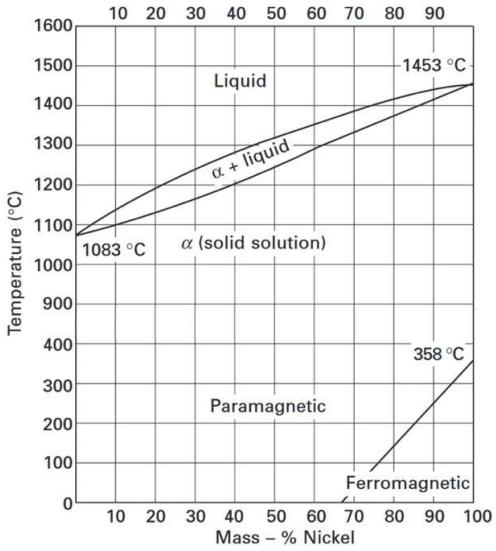

Figure 14. CuNi Phase diagram [53].

Copper-nickel alloys commonly exhibit compositions with up to 30 wt% nickel and take the form of solid-solution alloys. The incorporation of elements such as

iron, chromium, niobium, silicon, and manganese serve to enhance their properties. The effects of these elements are succinctly described as follows:

- the addition of manganese during melting serves for deoxidation, enhancing castability and elevating tensile strength, especially the softening temperature;
- when dissolved in the matrix, iron heightens the corrosion resistance of CuNi alloys. It stimulates the formation of a consistent, firmly adhering corrosion-protective layer, thereby boosting corrosion resistance, particularly in swiftly flowing seawater. Iron contributes to modest improvements in mechanical properties, albeit slightly diminishing cold workability;
- tin amplifies tensile strength, high-temperature corrosion resistance, and wear resistance of CuNi alloys. CuNi alloys containing 2% Sn exhibit excellent stress relaxation properties, making them valuable for spring applications. In cast alloys, tin improves castability and acts as a deoxidizing agent;
- in the copper-nickel system, the solubility of silicon rises with increasing nickel content. Within the solubility limit, greater silicon content enhances mechanical strength and ductility;
- niobium boosts tensile strength and proof strength while decreasing elongation. It also positively influences the weldability of cast alloys. In wrought alloys intended for hot working;
- lead content is kept below 0.02%.

Undesirable elements in copper-nickel alloys include arsenic, sulfur, antimony, and tellurium because they are known to induce embrittlement in the alloy [53].

Copper-nickel alloys showcase exceptional attributes, notably including remarkable corrosion resistance in seawater, thermal stability, and an almost unparalleled immunity to Stress Corrosion Cracking in environments that can be detrimental to other copper alloys. Alloys with lower nickel content, falling within the range of 2 to 4 wt%, are particularly suited for applications in strip form for electrical and electronic products. In these applications, a combination of strength, thermal stability, and favorable bend formability is crucial. On the other hand, alloys containing around 10 wt% nickel exhibit exceptional resistance to biofouling. Furthermore, as nickel content increases, various properties generally improve. The optimal corrosion resistance is observed in copper-nickel alloys with a composition of approximately 30% nickel.

Copper-nickel alloys find extensive use in maritime applications, serving on ships, offshore platforms, and coastal power plants. They have garnered recognition as the primary materials for evaporative desalination plants[49].

3.2.1 Cu-Ni-Si alloys

Copper-nickel-silicon alloys contain a nickel content that spans from 2 to 3 wt.% and a silicon content below 1%. These alloys belong to the category of copper-base alloys known for their capacity for precipitation hardening. The heat treatment employed to achieve this precipitation hardening traditionally involves a solution heat treatment within the range of 760 to 955 °C, followed by an aging heat treatment within the range of 260 to 565 °C [49]. The mechanism responsible for strengthening involves the formation of δ-Ni_2Si precipitates. These alloys exhibit superior mechanical properties compared to pure copper. Notably, they can attain a tensile strength of up to 590 MPa, as reported by Monzen et al., albeit with a trade-off in electrical conductivity, which decreases to around 47% IACS [54]. Cu-Ni-Si alloys are applied as spring contacts and lead frames, serving as alternatives to alloys containing beryllium, a material associated with health risks.

Chapter 4

Additive Manufacturing of Copper and Copper Alloys

In the last years, AM has showcased its potential to reduce the traditional cost associated with copper component production. It achieves this goal by eliminating the need of complex manufacturing tooling, the assembly of numerous parts, and high temperature joining operations.

Several recent studies have extensively explored the difficulties inherent in the additive manufacturing of copper and its alloys, particularly, in the context of L-PBF approaches. One prominent challenge arises from copper high thermal conductivity, which rapidly dissipates heat from the melting area. This phenomenon leads to the formation of local and global thermal gradients, residual stress build-up, and distortion in the final product. These issues are compounded by the significant differences in thermophysical properties between the consolidated material and the surrounding powder bed. Furthermore, the high reflectivity of copper at the common red laser wavelength (around 1060 nm), widely used in many commercial L-PBF systems, often needs the utilization of high beam power. This, in turn, results in increased recoil pressure, vaporization, spatter, and other undesirable defects in the printed components. It is worth noting that for L-PBF and many other AM processes, one must also acknowledge that copper alloys desirable properties are highly sensitive to contamination, especially by oxygen. Controlling this contamination can be challenging due to the exceptionally large surface area of

typical AM powder feedstock, adding another layer of complexity to the manufacturing process [15].

To address these issues, particularly the challenge of high reflectivity, various approaches can be explored.

One approach involves a technological solution, which entails utilizing an alternative energy source to enhance energy absorption. In the context of laser technology, the use of lasers with wavelengths different from the near-infrared laser can be considered to improve absorption. Green (515 nm) or blue (450 nm) lasers can be employed for this purpose, potentially increasing energy absorption from 27% up to 77% [55] (Figure 15).

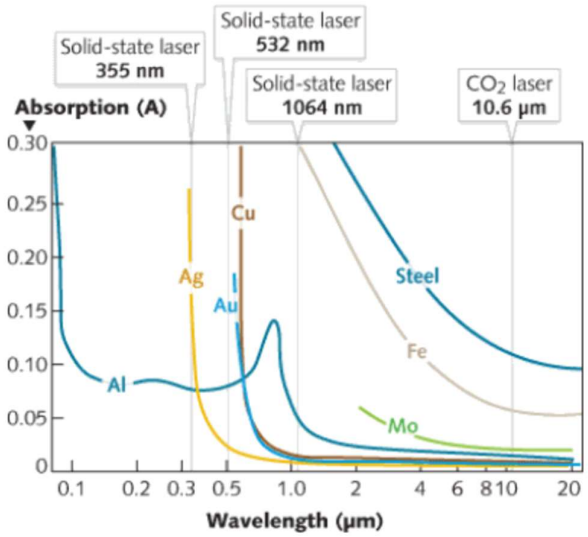

Figure 15. The absorption of material versus wavelength [56].

By completely altering the energy source, the option of employing EB-PBF technology becomes viable. As mentioned earlier, EB-PBF utilizes an electron beam as its energy source. Due to the distinct absorption and reflection mechanisms of electrons in contrast to photons, the EB-PBF process remains unaffected by the optical reflectivity of materials, and a significant portion of the energy is deposited within the materials [57]. Additionally, it's worth noting that the entire process takes place under vacuum conditions, which effectively mitigates the risk of material oxidation [58].

The second approach under consideration involves material modification. Primarily used to enhance the absorption of pure copper, this method could involve the powder surface treatments (coating) or the incorporation of particles with higher absorptivity into the pure copper batch [59–61]. Additionally, this approach may involve the addition of a small quantity of alloying elements to the copper matrix through the development of specific alloys [62].

Table 4 lists the primary copper alloys presented in literature along with the corresponding AM processes employed.

Table 4. Copper alloys used for AM [15].

Composition (*wt%*)	**AM process**	**References**
Cu-(0.4–1.2)Cr	L-PBF	[63–65]
Cu-(0.5–1.2)Cr-(0.03–0.3)Zr	L-PBF	[66–68]
Cu-(0.5–0.7)Cr-(0.02–0.05)Zr-(0.02–0.05)Ti	L-PBF	[69]
Cu-0.5Cr	L-PBF	[70,71]
Cu-(1.3–2.5)Cr	L-PBF	[72]
Cu-(20–25)Cr	L-PBF, EB-PBF	[73,74]
Cu-7.2Ni-1.8Si-1Cr	L-PBF	[75,76]
Cu-2.4Ni-0.04Cr-0.7Si	L-PBF	[77–82]
Cu-15Ni-8Sn	L-PBF	[83]
Cu-4.1Zr-1.1B	L-PBF	[84]
Cu-4Sn		[85,86]
Cu-(10–15)Sn	L-PBF	[87–90]
Cu-10Zn	L-PBF	[91]
Cu-15Zn-2.8Si	L-PBF	[92]
Cu-6.5Cr-5.8Nb (GRCop-84)	L-PBF, EB-PBF, DED	[93–102]
Cu-3.3Cr-2.9Nb (GRCop-42)	L-PBF	[103–105]
Cu-11.85Al-3.2Ni-3Mn	L-PBF	[106–109]

In this chapter, the main results obtained to date on pure copper and CuNiSi alloy processed by both L-PBF and EB-PBF are reported.

4.1 Pure copper

4.1.1 L-PBF Red laser (1060nm)

Pure copper exhibits high reflectivity in the near-infrared radiation spectrum, resulting in low energy absorption and a back reflection issue. This low absorption necessitates the use of high-power laser systems to achieve the required energy for powder melting and to obtain a full dense part. The back reflection can potentially damage the laser mirror, as documented by Jadhav et al., with an example illustrated in Figure 16 [110].

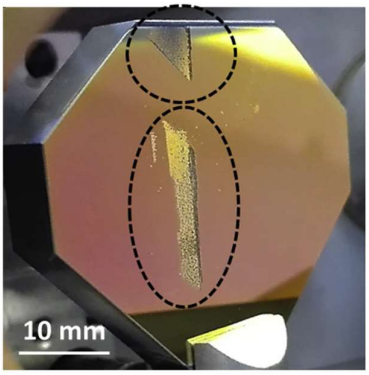

Figure 16. Damaged laser mirror after laser back reflection issue[110].

Numerous studies have focused on manufacturing fully dense copper samples utilizing laser power up to 1 kW [110–121].

Lykov et al. [119] achieved a notably low relative density of 88.1% employing a commercial L-PFB machine with a maximum laser power of 200W and a laser beam diameter of 35 µm. They adjusted the scanning speed within the 100 to 150 mm/s range, maintained a layer thickness of 50 µm, and employed a hatching distance of 120 µm. Their optimization of process parameters led to a tensile strength of 149 MPa. Huang et al. [120], using a L-PBF machine equipped with a laser with a maximum power of 300W, a scanning speed of 600 mm/s, a layer thickness of 30 µm and a hatching distance of 80 µm, obtained samples with a relative density of 98,8%. Yan et Al. [115] obtained a relative density of 99.1% using a laser power of 300 W, a scanning speed of 600 mm/s, a layer thickness of

30 µm, and a hatching distance of 80 µm. Jadhav et al. [110] conducted an exhaustive evaluation of various process parameters, including laser power, hatching distance, and scan speed, with ranges spanning 600 to 800 W, 70 to 90 µm, and 200 to 600 mm/s, respectively. They employed a layer thickness of 30 µm and ultimately achieved their best result using 800 W, 90 µm, and 400 mm/s, yielding a relative density of 98%, electrical conductivity of 88% IACS, and a remarkable thermal conductivity of up to 336 W/mK. Ikeshoji et al. [114] obtained samples with rough texture and ball-shaped asperities without sever oxidation and a relative density of 96,6%. Their methodology involved a laser power of 800W, a scanning speed of 300 mm/s, a layer thickness of 50 µm, and a hatching distance varying between 0.025 and 0.12 mm. Colopi et al. [116] undertook an investigation into the evolution of relative density by varying laser power, layer thickness, and scan speed, within the ranges of 200 to 1000 W, 50 to 100 µm, and 1000 to 4000 mm/s, respectively. They achieved their most favorable outcome, a relative density of 98.7%, using parameters of 600 W, 50 µm, and 1000 mm/s.

Further experimental findings have demonstrated that laser powers below 400 W are often inadequate for achieving complete densification [119]. Moreover, Stoll et al. achieved the most promising outcome, attaining a relative density of 99.82% (Figure 17) and an electrical conductivity of 56.88 MS/m (98%IACS) by employing a laser power of 400 W, a scan speed of 600 mm/s and a layer thickness of 30 µm [121].

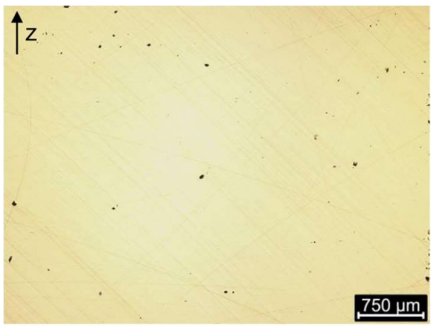

Figure 17. Cross-section of pure copper sample produced by red L-PBF technology with a relative density of 99.82% [121].

A summary of the mechanical and physical properties of the pure copper processed by red L-PBF found in literature are reported in Table 5.

Table 5. Mechanical and physical properties of pure copper processed by red L-PBF (n.d. non detected).

Study	**Process parameters (P, v, h_d, l_t)**	**Relative density (*%*)**	**Electrical conductivity (*%IACS*)**	**Tensile Strength (*MPa*)**	**Thermal Conductivity (*W/m*K*)**
Lykov et al. [119]	200 W – 100 mm/s – 120 µm – 50 µm	88.1	n.d.	149	n.d.
Ikeshoji et al. [114]	800 W – 300 mm/s – 100 µm – 50 µm	96.6	n.d.	n.d.	n.d.
Jadhav et al. [113]	500 W – 400 mm/s – 90 µm – 30 µm	>97.5	89	270	n.d.
Jadhav et al. [110]	800 W – 400 mm/s – 90 µm – 30 µm	98	88	n.d.	336
Colopi et al. [116]	600 W – 1000 mm/s – 70 µm – 50 µm	98.7	n.d.	n.d.	n.d.
Huang et al. [120]	300 W – 600 mm/s – 80 µm – 30 µm	98.8	41	242	n.d.
Yan et al. [115]	300 W – 600 mm/s – 80 µm – 30 µm	99.1	n.d.	187	n.d.
Jadhav et al. [112]	500 W – 800 mm/s – 90 µm – 30 µm	99.3	94	211	392
Stoll et al. [121]	400 W – 600 mm/s – / µm – 30 µm	99.82	98	n.d.	n.d.

4.1.1.1 Material modification

Jadhav et al. processed a powder blend comprised pure copper powder mixed with 0.1 wt.% of carbon nanoparticles [60]. The goal of this attempt was to enhance absorption without compromising electrical and thermal properties. This approach increased the absorption from 29 to 67% (Figure 18) and allowed to obtain a relative density of 98% using a laser power of 725 W and an energy density within the range of 200-500 J/mm^3. This was a good result compared to the minimum energy density of 700 J/mm^3 required to obtain dense samples from pure copper powders processed with the same machine [110]. Anyway, the mechanical properties and electrical conductivity were compromised due to the segregation of carbon nanoparticles and the presence of various impurities along the grain boundaries (Table 6).

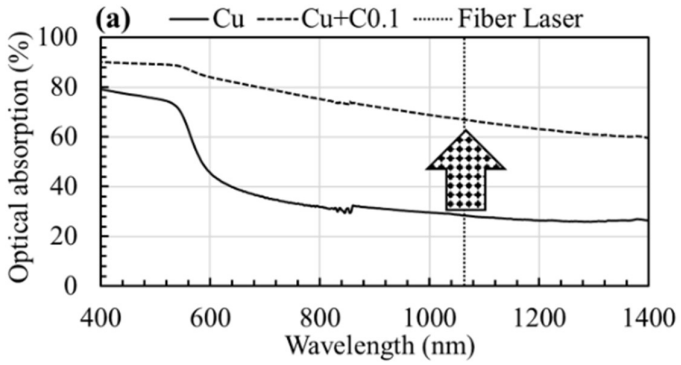

Figure 18. Optical absorption for both pure copper and 0.1 wt.% carbon-mixed-copper powder [60].

Table 6. Comparison between L-PBF pure copper samples and pure copper +0.1% C.

Alloy	**Relative density (%)**	**Electrical conductivity (*%IACS*)**	**Tensile Strength (*MPa*)**	**ε (%)**
Pure copper + 0.1% C [60]	98	39	125 ± 11	3 ± 1
Pure copper [110]	98	100	179-262	35

4.1.2 L-PBF Green laser (515nm)

Pure copper exhibits an absorptivity of approximately 77% at a wavelength of 515 nm, in contrast to 27% at a wavelength of 1060 nm (Figure 26) [55]. Increasing absorption at shorter wavelengths substantially enhances energy coupling, a critical factor in the fusion of materials with high heat conduction properties such as pure and low-alloy copper. Few studies have been conducted on this topic, but they are very promising [55,122–124]. Gruber et al., using a TruPrint 1000 green edition equipped with a green laser with maximum power of 500 W, a line energy of 0.808 J/mm, a hatching distance of 120 µm and a layer thickness of 30 µm, achieved bulk samples with a relative density of 99.8%, featuring a dense core and a porous surface, as shown in Figure 19. They also measured an electrical conductivity of 58.12 MS/m and a horizontal tensile strength of 224 MPa. [55].

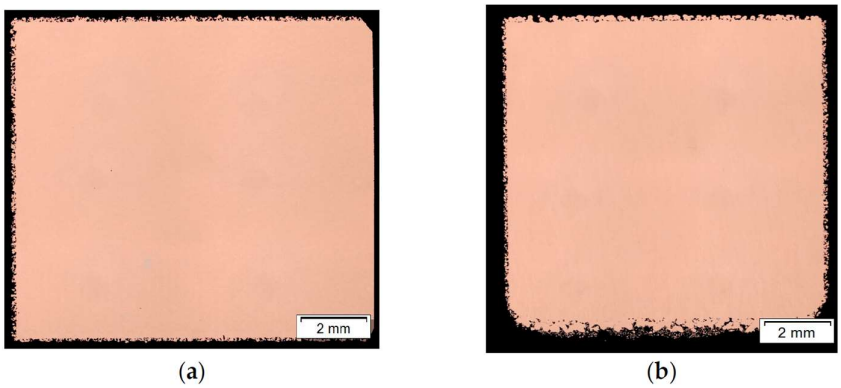

Figure 19. Cross-section of a pure copper sample produced by green L-PBF technology in the a) x-y plane and b) x-z plane [55].

Furthermore, Wagenblast et al. obtained dense samples with a relative density of 99.8%, electrical conductivity at 100% IACS, and a horizontal tensile strength of 241 MPa [123]. The paper do not define the optimized process parameters nor the printer used. Finally, De Terries et al., using a green laser L-PBF machine with maximum laser power of 500 W, attained a relative density of 99.75%, electrical conductivity at 100% IACS, a thermal conductivity of 406 W/m*K, and a horizontal tensile strength of 214 MPa. Also in this case, the optimized parameters are not published. These results are summarized in Table 7 and they prove that the use of the green laser source resulted in a stable process to build high-quality copper samples.

Table 7. Mechanical and physical properties of pure copper processed by green L-PBF (n.d. non detected).

Study	Relative density (*%*)	Electrical conductivity (*%IACS*)	Tensile Strength (*MPa*)	Thermal Conductivity (*W/m*K*)
Gruber et al. [55]	99.8	100	224	n.d.
Wagenblast et al. [123]	99.8	100	241	n.d.
De Terris et al. [124]	99.7	100	214	406

4.1.3 EB-PBF

The EB-PBF technology remains unaffected by the optical reflectivity of materials due to the distinct absorption and reflection mechanisms of electrons compared to photons as much as 95% of the total supplied energy is transferred to the copper with no risk of back reflections [79]. Consequently, a substantial portion of the energy in EB-PBF is deposited within the materials, rendering it highly promising for the processing of pure copper, as substantiated by numerous studies [50,58,125–132]. In the initial experiments involving EB-PBF of copper conducted by Frigola et al. [131] the achieved electrical conductivity stood at approximately 97% IACS. This figure notably falls short of the 101% IACS requirement for oxygen-free electrical (OFE) copper. Subsequently, Raab et al. [125] reported a maximum electrical conductivity of 96.24% IACS. In both instances, the reported material densities were relatively high, with the gap in conductivity largely attributed to the presence of interstitial contaminants within the powder feedstock. Nevertheless, Guschlbauer et al. [127] and Ledford et al. [129] later achieved electrical conductivities exceeding 101% IACS. Notably, Raab et al. and Frigola et al. also found thermal conductivity values of 400.1 W/mK and 390 W/mK, respectively.

Figure 20 displays the processing space for pure copper, as characterized by volumetric energy density, while considering an oxygen content typical of electrolytic tough pitch (ETP) copper [130].

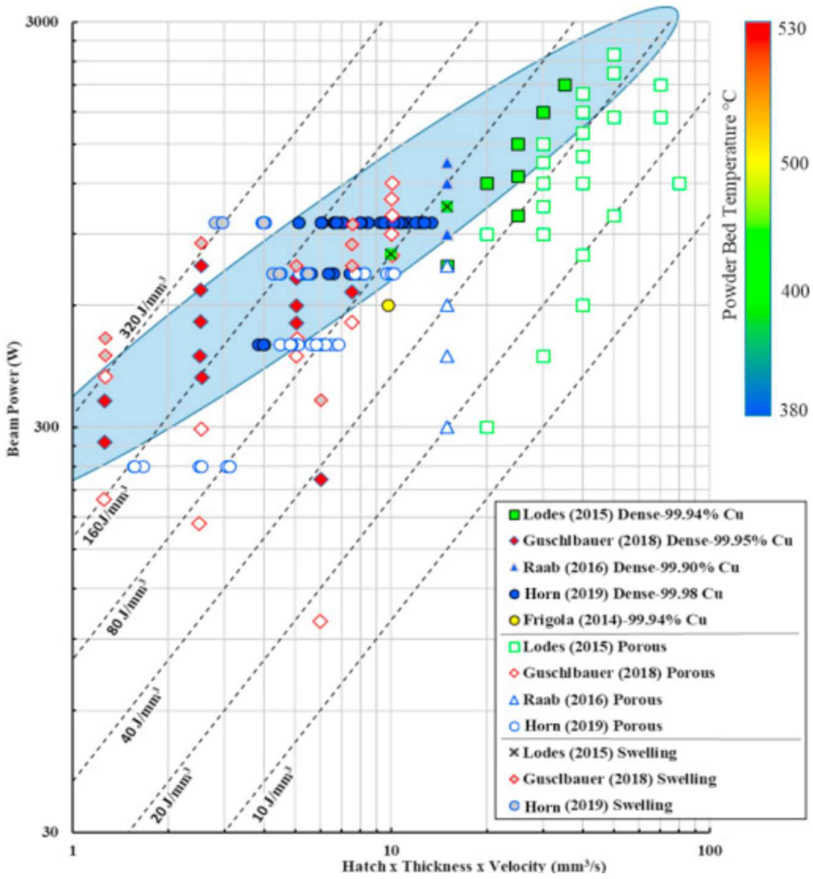

Figure 20. Processing space for copper using EB PBF. Relative densities above 99.5% are considered dense. Note for each reported instance, the ambient build/surface temperatures are different [130].

Upon a comprehensive examination of various combinations of beam power and speed, the achievable processing envelope for pure copper becomes evident corresponding at the blue area in Figure 20. However, it is notable that this space exhibits some deviations from the lines of constant volumetric energy density. This divergence is unsurprising, given the potential influence of various external or unreported factors on melting behavior. These factors may include spot size, powder size distribution, oxide thickness, powder bed packing, and more [130].

The EB-PBF process is thus capable of directly producing copper components with the highest relative density, tensile strength, and superior electrical and thermal conductivities. Moreover, the process reliability has been demonstrated in

fabricating intricate structures such as open cellular structures and vacuum electronic devices.

Despite the advantages of EB-PBF and these outstanding achievements, one of the primary challenges when processing copper with EB-PBF lies in dealing with the elevated temperatures, compounded by copper high thermal conductivity. In fact, both the temperature of the powder bed and the molten part rise rapidly and can easily lead to evaporation phenomena if not well controlled [62]. In any case, Guschlbauer et al. obtained the highest values in terms of relative density, electrical conductivity, tensile strength, and thermal conductivity, listed in Table 8, using an electron beam power of 850 W and a scanning speed of 1500 mm/s.

Table 8. Mechanical and physical properties of pure copper processed by EB-PBF.

AM process	**Relative density (*%*)**	**Electrical conductivity (*%IACS*)**	**Tensile Strength (*MPa*)**	**Thermal Conductivity (*W/m*K*)**
EB-PBF [78]	99.95	100	177	411.89

4.2 CuNiSi alloys

CuNiSi alloys are the predominant copper-nickel alloys processed through additive manufacturing, specifically employing the red L-PBF technology. These alloys boast a unique quality, exhibiting significantly enhanced absorptivity at 1060 nm (red laser) in contrast to pure copper. This property enhances the potential to achieve high densities, even though there have been relatively few studies conducted on these alloys [78,80–82]. Tiberto et al. [80] conducted an investigation into porosity as a function of different process parameters using three CuNiSi powders (CuNiSiCr, CuNi1.5Si, and CuNi3Si) processed with a Concept Laser Mlab machine, with maximum laser power of 100 W. They achieved the highest relative density result of 94% for CuNi3Si by employing a laser power of 95 W, a scanning speed of 200 mm/s, a hatching distance of 36 µm, and a layer thickness of 15 µm. Furthermore, their observations revealed that a reduction in the Ni content also led to a decrease in relative density. Ventura et al. [82] produced samples of C70250 alloy (CuNi3.3Si0.9) with a relative density of 98% using an EOSINT M280 equipped with a 200 W Yb-fiber laser and an energy density of 107 J/mm³. Zhou et al. [81] obtained fully dense Cu2.4Ni0.7Si samples using an SLM250 facility machine with a 500W laser. They utilized a laser power of 360 W, a

scanning speed of 550 mm/s, a layer thickness of 30 µm, and a hatching distance of 80 µm to achieve a relative density of 99.5%. Finally, Zhang et al. [78] studied the relative densities of K220 alloy (CuNi2.4Si0.7) L-PBF parts under different laser energy densities. They employed an SLM250HL machine with a maximum laser power of 400 W, producing samples with varying scanning speeds and hatching distances while keeping the laser power at 375 W and the layer thickness at 30 µm. Their results are presented in Figure 21.

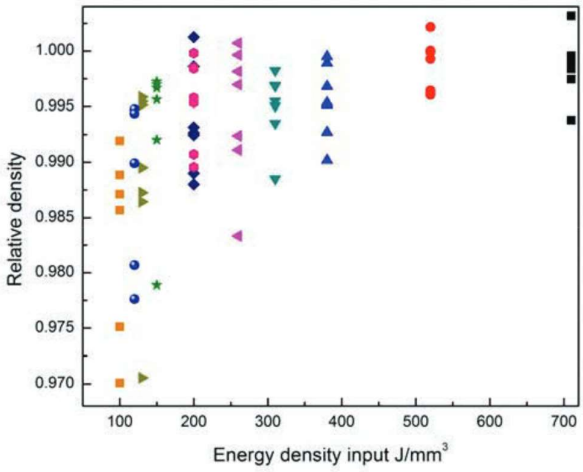

Figure 21. Relative density of L-PBF K220 samples against VED [78].

They observed that the rise in relative density is linked to the escalation in VED. For VED values exceeding 200 J/mm³, the relative densities of the components were consistently observed to exceed 98.8%. However, at higher VED levels, the L-PBF process was impeded due to severe balling. The best result of relative density of 99.9% was reached using a laser power of 375 W, a scanning speed of 550 mm/s, a hatching distance of 90 µm and a layer thickness of 30 µm.

As previously discussed in this thesis, CuNiSi alloys are categorized as precipitation-hardening alloys. Therefore, it is crucial to optimize the post-heat treatment process to achieve the best mechanical and physical properties. After traditional processes, parts undergo a solutioning heat treatment within the range of 760 to 955 °C, followed by quenching and subsequent aging within the range of 260 to 565 °C, a process that can span from one to several hours. However, the rapid cooling rate achieved through L-PBF eliminates the need for the solutioning

step, allowing for optimal properties to be attained by directly aging the material at the optimized temperature of 450 °C (Figure 22) as reported by Ventura et al. [82].

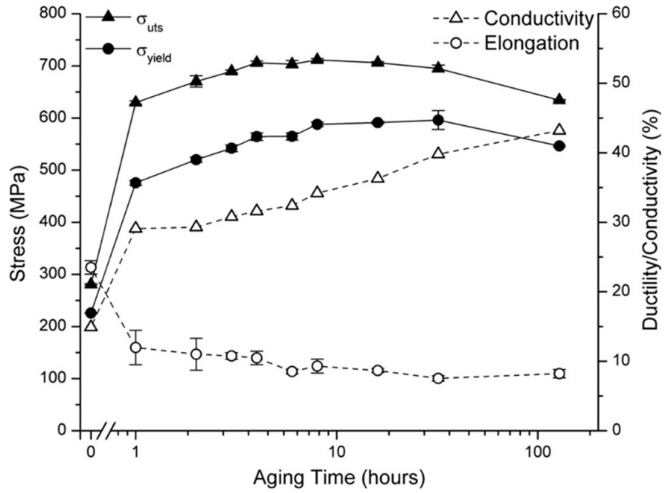

Figure 22. Physical property evolution of L-PBF C70250 alloy (CuNi3.3Si0.9) treated by Direct aging at 450°C [82].

They found that the optimal aging duration to achieve the highest ultimate tensile strength is 8 hours. It's important to note that during this period, the electrical conductivity remains relatively low, at approximately 32% IACS. After an extended aging duration of about 40 hours, there is a degradation in ultimate tensile strength. The mechanical properties decrease due to the coarsening of the precipitates and the loss of coherency as the particles grow. However, electrical conductivity continues to increase and reaches its peak in the overaged condition, typically after around 128 hours, at approximately 44% IACS [82]. Furthermore, their findings indicate that these alloys contain 2 to 3% precipitates by volume, resulting in strengths of approximately 700 MPa, along with electrical conductivities ranging from 35 to 45% IACS [82]. These data can be compared with the study by Semboshi et al. [133] on the evolution of the electrical conductivity of the Cu-4.3 at.% Ni-2.2 at.% Si alloy processed by cold rolling with varying aging times (Figure 23). In this case, the electrical conductivity value after quenching is about 15% IACS, comparable to the value found by Ventura et al., and it increases to 55% IACS after 500 hours at 450 °C.

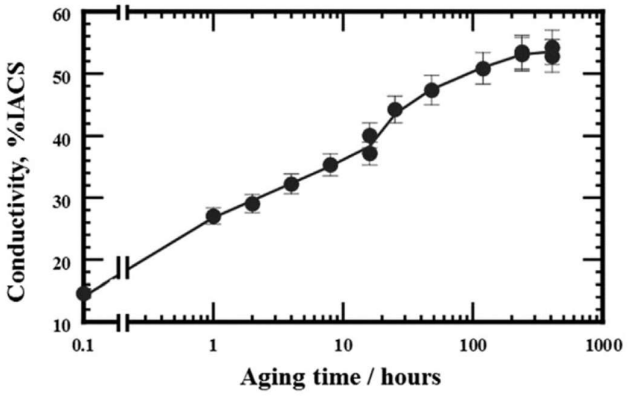

Figure 23. Variations in electrical conductivity as a function of aging time for Cu-4.3 at.% Ni-2.2 at.% Si alloy specimens aged at 450°C (723 K) [133].

Chapter 5

Materials and methods

5.1 Powders

For this work, a pure copper and a CuNi2SiCr powders were utilized. The characteristics of these powders are presented in this paragraph.

5.1.1 Powder flowing behavior

5.1.1.1 Hall flowmeter funnel test

The Hall Flowmeter funnel test is the preferred method for determining the flowability of metal powders and powder mixtures. This test method is based on the flow of a specified mass of powder through a funnel (Hall) and measuring the time it takes for the powder to completely flow through the funnel. Tests were carried out following the standard ASTM B213-17 [134].

5.1.1.2 Apparent density

Under controlled conditions, a defined volume of powder is allowed to flow into a container with a fixed volume. The mass of powder per unit volume is then calculated and reported as the apparent density. Tests were carried out following the standard ASTM B212-17 [135].

5.1.1.3 Tap density

The tap density, or packed density, of metal powders and compounds, is the density of a powder that has been tapped, to settle contents, in a container under

specified conditions. Tests were carried out following the standard ASTM B527-15 [136].

5.1.1.4 Skeletal density

The skeletal density is the ratio of mass of discrete pieces of solid material to the sum of the volumes of the solid material in the pieces and closed pores within the pieces. Tests were carried out following the standard ASTM B923-23 [137].

5.1.2 Pure copper

A gas atomized pure copper powder provided by Ronald Britton Ltd. was used in this study. The chemical composition of the pure copper is reported in

Table 9.

Table 9. Pure copper powder chemical composition provided by Ronald Britton Ltd.

Element	**Cu**	**O**	**P**
Wt.%	>99.00	<0.15	<0.50

The SEM micrographs, as illustrated in Figure 24, disclose the existence of particles with both spherical and elongated shapes, alongside the presence of certain satellites. In Figure 24c is represented the cross-section of the powders showing a good circularity and the presence of few internal porosities.

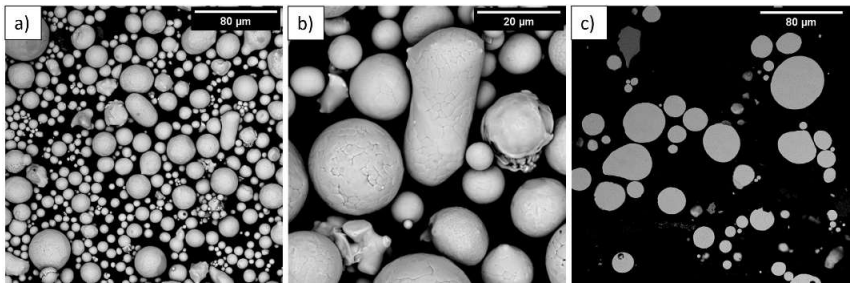

Figure 24. SEM images of pure copper powder on top a) 1000 X, b) 4000X and c) cross-section 4000X

The particle size distribution (PSD) of this powder is reported in Figure 25. Specifically, the d10, d50, and d90 values for this powder are 15.6 µm, 31.0 µm, and 51.9 µm, respectively.

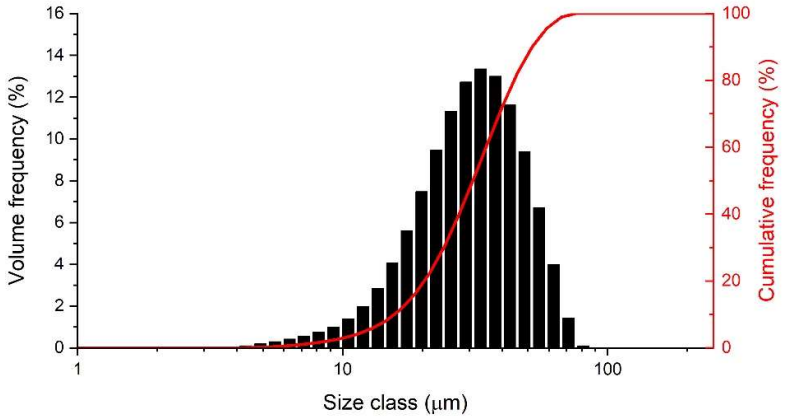

Figure 25. Particle size distribution of the pure copper powder.

The flowability, the apparent density, the tap density and the skeletal density are reported in Table 10.

Table 10. Flowability, apparent, tap and skeletal densities of pure copper powder.

Flowability	12,2 ± 0,2 s/50g
Apparent density	5,55 ± 0,01 g/cm^3
Tap density	5,88 ± 0,01 g/cm^3
Skeletal density	8,903 ± 0,001 g/cm^3

The apparent and tap density values were used to calculate the Compressibility Index and the Hausner ratio that were reported in Table 11. The obtained values are within the threshold of excellent flow character.

Table 11. Compressibility Index and Hausner Ratio of pure copper powder.

Index	Value	Flowability
CI	3,74	Excellent
HR	1,03	Excellent

The absorbance of pure copper powder at different wavelengths is reported in Figure 26. The powder showed an absorbance of 27% at 1060 nm (red laser) and 78% at 515 nm (green laser).

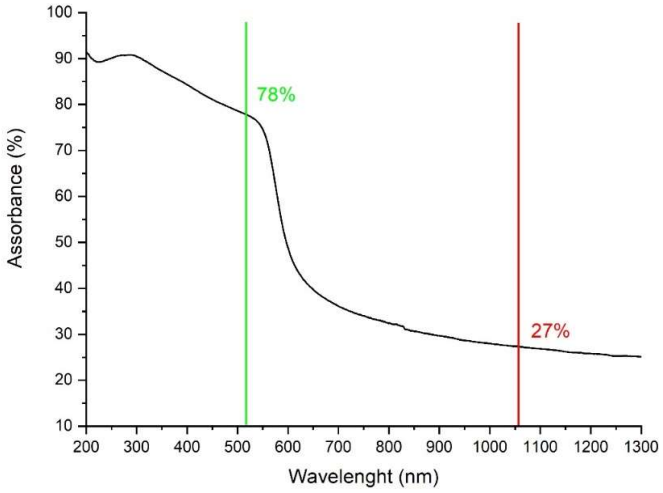

Figure 26. The absorption versus wavelength of Ronald Britton pure copper powder.

5.1.3 CuNi2SiCr

A CuNi2SiCr powder produced by gas atomization by Praxair, Inc. was used for this work. The chemical composition of the CuNi2SiCr is reported in Table 12.

Table 12. CuNi2SiCr powder chemical composition.

Element	Cu	Ni	Si	Cr	Fe	O	P
Wt.%	Balance	2.38	0.49	0.47	0.09	0.021	<0.005

The SEM images of the powder, as depicted in Figure 27, underline the presence of predominantly spherical and elongated particles, along with some clusters and satellite structures. In Figure 27c is represented the cross-section of the powders showing a good circularity with some irregular shape and the presence of few internal porosities.

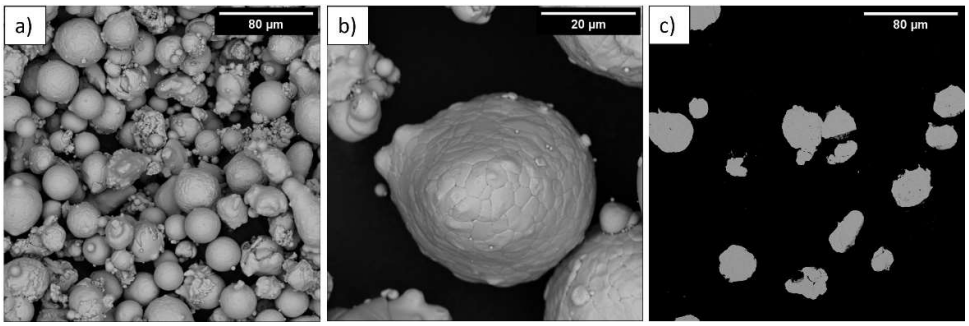

Figure 27. SEM images of CuNi2SiCr alloy particles on top a) 1000 X, b) 4000X and c) cross-section 4000X

The PSD of the powder is reported in Figure 28. Specifically, the d10, d50, and d90 values are 18.2 µm, 29.8 µm, and 47.5 µm, respectively.

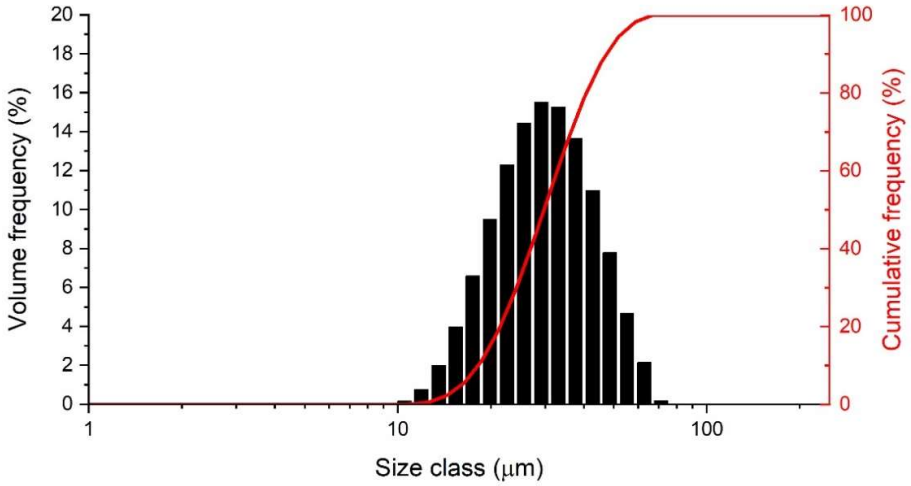

Figure 28. Particle size distribution of the CuNi2SiCr powder.

The flowability, the apparent density, the tap density and the skeletal density are reported in Table 13.

Table 13. Flowability, apparent, tap and skeletal densities of CuNi2SiCr powder.

Flowability	14,0 ± 0,2 s/50g
Apparent density	4,72 ± 0,05 g/cm^3
Tap density	5,36 ± 0,08 g/cm^3
Skeletal density	8,846 ± 0,001 g/cm^3

The apparent and tap density values were used to calculate the Compressibility Index and the Hausner ratio that were reported in Table 14. The obtained values are within the threshold of excellent flow character.

Table 14. Compressibility Index and Hausner Ratio of CuNi2SiCr powder.

Index	Value	Flowability
CI	8,94	Excellent
HR	1,10	Excellent

The absorbance of CuNi2SiCr powder at different wavelengths is reported in Figure 29. The powder showed an absorbance of 49% at 1060 nm (red laser) and 87% at 515 nm (green laser).

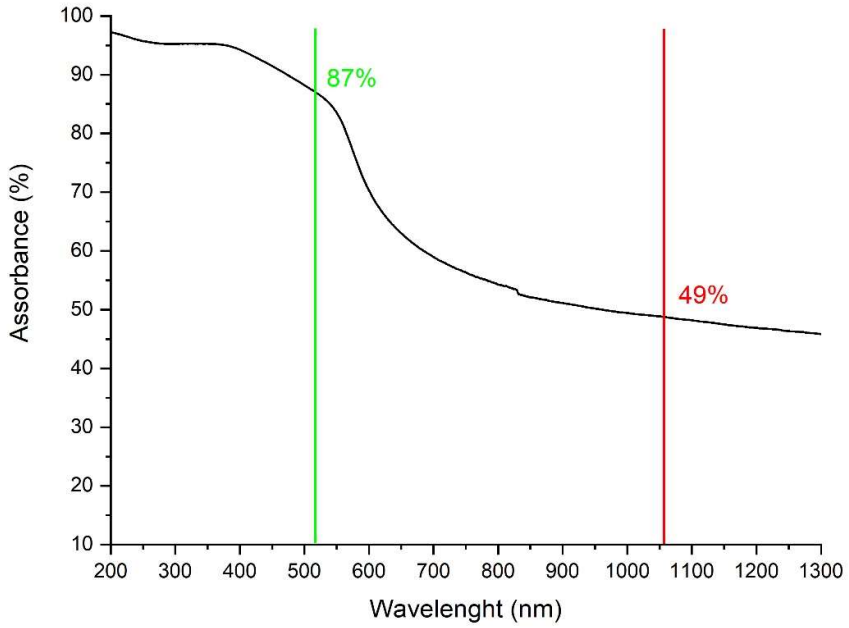

Figure 29. The absorption versus wavelength of Praxair CuNi2SiCr powder.

5.2 L-PBF systems

For this thesis three L-PBF machines were used: a low-power red laser machine, a medium-power red laser machine and a green laser machine. In this paragraph, an overview of these machines is provided.

5.2.1 Low-power red laser system

A Concept Laser Mlab R machine (Figure 30) produced by GE additive was used to produce samples with a low-power red laser (up to 100 W). The main characteristics of the machine are listed in Table 15.

Figure 30. Concept Laser Mlab R machine by GE additive [138].

Table 15. Technical data of a Concept Laser Mlab R machine.

Build envelope	90x90x80 mm
Layer thickness	15 – 30 µm
Production speed	1 – 5 cm^3/h
Laser system	Fibre laser 100 W
Laser Wavelength	1070 nm
Max. scanning speed	7 m/s
Focus diameter	Approx. 50 µm
Power consumption	Max. 1.5 kW
Inert gas consumption	0.6 – 0.8 l/min

5.2.2 Medium-power red laser system

A Print Sharp 250 machine (Figure 31) produced by Prima Industrie S.p.A. was used to produce samples with a medium-power red laser (up to 500 W). The main characteristics of the machine are listed in Table 16.

Figure 31. Print Sharp 250 by Prima Industrie [139].

Table 16. Technical data of a Print Sharp 250 machine.

Build envelope	258x258x330 mm
Layer thickness	20 – 100 µm
Production speed	12 – 30 cm^3/h
Laser system	Fibre laser IR single mode 500 W
Laser Wavelength	1070 nm
Focus diameter	100 µm

5.2.3 Low-power green laser system

A Print Green 150 machine (Figure 32) produced by Prima Industrie S.p.A. was used to produce samples with a green laser. The main characteristics of the machine are listed in Table 17.

Figure 32. Print Green 150 by Prima Industrie [140].

Table 17. Technical data of a Print Green 150 machine.

Build envelope	Ø = 150 mm; h = 330 mm
Layer thickness	20 – 120 µm
Laser system	Green fibre laser 200 W
Laser Wavelength	515 nm
Focus diameter	35-100 µm
Pre-heated platform	Up to 300 °C

5.3 EB-PBF system

To print EB-PBF samples, a Freemelt ONE machine (Figure 33) produced by Freemelt was used. The main characteristics of the machine are listed in Table 18. This machine has an open system architecture and has been specifically designed

for materials research and development. Consequently, it operates without any limitations on process parameters and setup configurations.

Figure 33. Freemelt ONE machine by Freemelt [141].

Table 18. Technical data of the Freemelt ONE machine

Build envelope	Ø = 100 mm; h = 100 mm
Beam power	Max 6 kW
Beam acceleration voltage	60 kV
Base pressure in vacuum chamber	10^{-6} hPa (mbar)
Base pressure in electron gun	10^{-7} hPa (mbar)
Cathode heater	CO_2 Laser

5.4 Printing parameter optimization

The process parameters were studied and optimized to achieve a relative density value as close as possible to 100%. The evaluated parameters were the parameters used to calculate the VED: the power of the laser or electron beam (P), scanning speed (v), layer thickness (lt), and hatching distance or line offset (hd/lo).

5.4.1 Pure copper samples

Pure copper was processed by the EB-PBF system. In this section the followed experimental procedure is reported.

5.4.1.1 Samples production

Samples of pure copper were manufactured using a Freemelt ONE machine. Two batches of cubes (Figure 34), each with a size of 12 mm, were printed using a snake-like scanning strategy with rotation 0-90° to optimize process parameters.

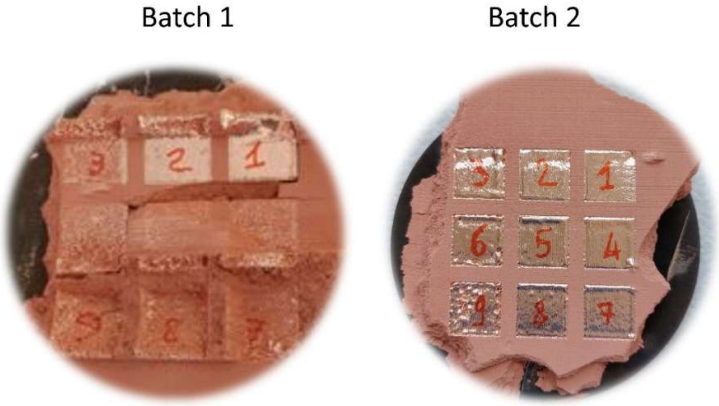

Figure 34. Batch 1 and 2 of pure copper cubes produced by EB-PBF Freemelt ONE machine.

The optimization of process parameters was carried out based on the study by Raab et al. [125], maintaining a constant electron beam power of 720 W (beam current 12mA), a layer thickness of 0.05 mm, a line offset of 0.2 mm. Just the scanning speed was varied during the experimentation. The list of the parameters used is reported in Table 19 and Table 20.

Table 19. Freemelt ONE pure copper Batch 1 process parameters (P = 720 W; Line offset = 0.2 mm; Layer thickness = 0.05 mm).

Batch	Sample	Scanning Speed (mm/s)	VED (J/mm^3)
1	1	720	100
	2	960	75
	3	1200	60
	4	1440	50
	5	1680	43
	6	1920	38
	7	2160	33
	8	2400	30
	9	2640	27

Table 20.Freemelt ONE pure copper Batch 2 process parameters (P = 720 W; Line offset = 0.2 mm; Layer thickness = 0.05 mm).

Batch	Sample	Scanning Speed (mm/s)	VED (J/mm^3)
2	1	300	240
	2	400	180
	3	500	144
	4	600	120
	5	700	103
	6	800	90
	7	900	80
	8	1000	72
	9	1100	65

5.4.2 CuNi2SiCr samples

CuNi2SiCr alloy was processed by L-BPF, utilizing a low-power red laser, a medium-power red laser and a low-power green laser. In this section the followed experimental procedure is reported.

5.4.2.1 Low-power red laser system

Low-power red laser samples of CuNi2SiCr alloy were produced using a Concept Laser Mlab R machine. Two batches of cubes (Figure 35), each with a size of 10 mm, were printed using a 67° rotational scanning strategy to optimize process parameters.

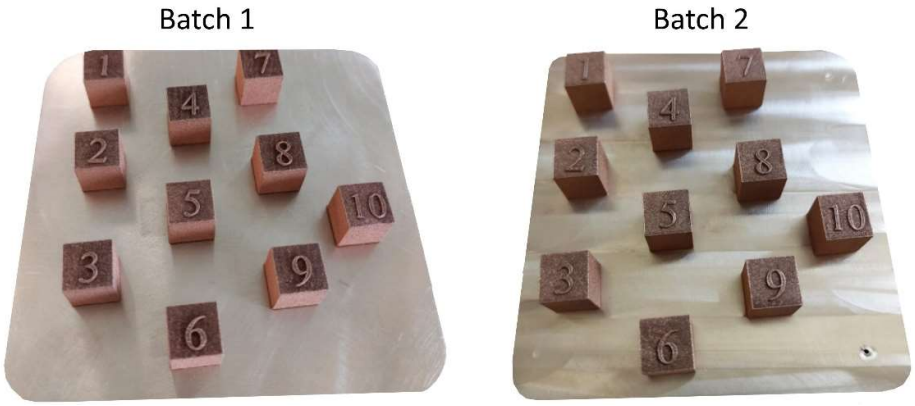

Figure 35. Batch 1 and 2 of CuNi2SiCr cubes produced by low-power red laser machine.

The optimization of process parameters was conducted with a constant laser power of 95 W while varying the hatching distance, layer thickness, and scanning speed. The list of the parameters used is reported in Table 21 and Table 22.

Table 21. Concept CuNi2SiCr Batch 1 process parameters (P = 95 W).

Batch	Sample	Scanning Speed (mm/s)	Hatch distance (mm)	Layer thickness (mm)	VED (J/mm^3)
1	1	200	0.10	0.015	317
	2	180	0.10	0.015	352
	3	160	0.10	0.015	396
	4	140	0.10	0.015	452
	5	120	0.10	0.015	528
	6	250	0.08	0.015	317
	7	225	0.08	0.015	352
	8	200	0.08	0.015	396
	9	175	0.08	0.015	452
	10	150	0.08	0.015	528

Table 22. Concept CuNi2SiCr Batch 2 process parameters (P = 95 W).

Batch	Sample	Scanning Speed (mm/s)	Hatch distance (mm)	Layer thickness (mm)	VED (J/mm^3)
2	1	200	0.10	0.010	475
	2	180	0.10	0.010	528
	3	160	0.10	0.010	594
	4	140	0.10	0.010	679
	5	120	0.10	0.010	792
	6	250	0.08	0.010	475
	7	225	0.08	0.010	528
	8	200	0.08	0.010	594
	9	175	0.08	0.010	679
	10	150	0.08	0.010	792

A third batch was produced using optimized process parameters obtained from batches 1 and 2. In this batch, samples for testing electrical conductivity (EC) and parallelepipeds shown in the Figure 36 were printed. The EC samples had dimensions of 6 x 10 x 2 mm^3, while the parallelepipeds had a height of 10 mm and cross-sectional dimensions that increased from 10 x 10 mm^2 to 20 x 20 mm^2.

Figure 36. Printed samples of the batch 3

5.4.2.2 Medium-power red laser system

Samples of CuNi2SiCr alloy were manufactured using a Print Sharp 250 machine equipped with a medium-power red laser. Two batches of samples (Figure 37) were printed to optimize process parameters and to undergo heat treatments. The first batch consisted of cubes each with a size of 12 mm, employing a 0-90° scanning strategy. The second batch was comprised of semi-cubes, sharing the same dimensions and the scanning strategy as the first batch, with a height of 6 mm.

Figure 37. Batch 1 and 2 of CuNi2SiCr samples produced by medium-power red laser machine.

The optimization of process parameters was carried out based on the study by Zhou et al. [81], maintaining a constant laser power of 360 W and a layer thickness of 0.03 mm. The hatching distance and scanning speed were varied during the experimentation. The list of the parameters used is reported in Table 23 and Table 24.

Table 23. Printsharp CuNi2SiCr Batch 1 process parameters (P = 360 W; Layer thickness = 0.03 mm).

Batch	Set	Sample	Scanning Speed (mm/s)	Hatch distance (mm)	VED (J/mm^3)
1	1	1	686	0.10	175
		2	600	0.10	200
		3	533	0.10	225
		4	480	0.10	250
		5	436	0.10	275
		6	400	0.10	300
		7	369	0.10	325
		8	343	0.10	350
		9	320	0.10	375
		10	300	0.10	400
	2	11	857	0.08	175
		12	750	0.08	200
		13	667	0.08	225
		14	600	0.08	250
		15	545	0.08	275
		16	500	0.08	300
		17	462	0.08	325
		18	429	0.08	350
		19	400	0.08	375
		20	375	0.08	400

Table 24. Printsharp CuNi2SiCr Batch 2 process parameters (P = 360 W; Layer thickness = 0.03 mm).

Batch	Sample	Scanning Speed (mm/s)	Hatch distance (mm)	VED (J/mm^3)
2	1	380	0.10	316
	2	370	0.10	324
	3	360	0.10	333
	4	350	0.10	343
	5	340	0.10	353
	6	330	0.10	364
	7	320	0.10	375
	8	310	0.10	387

Other 2 batches (3 and 4) were produced using optimized process parameters obtained from batches 1 and 2 (Figure 38). In these batches, 20 samples (10 for each batch) were printed for testing electrical conductivity and mechanical properties, after heat treatments. The sizes of the flat dog bone tensile samples follow the ASTM E8M standard.

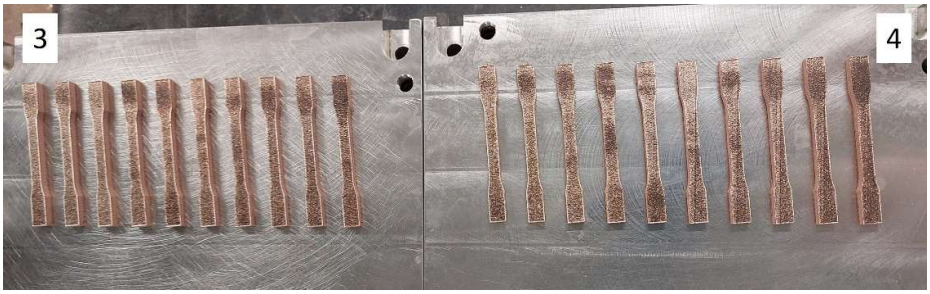

Figure 38. Printsharp CuNi2SiCr Batches 3 and 4 containing tensile samples.

5.4.2.3 Low-power green laser system

Samples of CuNi2SiCr alloy were manufactured using a Print Green 150 machine equipped with a low-power green laser. Two batches of samples (Figure 39), each with a size of 13 mm, were printed using a 0-90° (batch 1) and rotation of 67° (batch 2) scanning strategies to optimize process parameters.

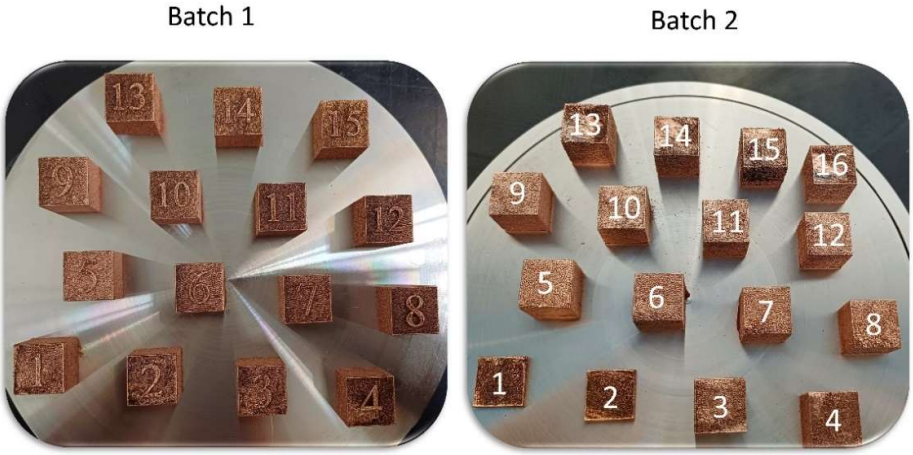

Figure 39. Batch 1 and 2 of CuNi2SiCr samples produced by low-power green laser machine.

The optimization of process parameters was carried out based on the study on pure copper by Gruber et al. [55]. It was assessed with a constant layer thickness of 0.03 mm while varying the laser power, the hatching distance and scanning speed. The list of the parameters used is reported in Table 25 and Table 26.

Table 25. Printgreen CuNi2SiCr Batch 1 process parameters (Layer thickness = 0.03 mm).

Batch	Set	Sample	Power (W)	Scanning Speed (mm/s)	Hatch distance (mm)	VED (J/mm^3)
1	1	1	180	200	0.08	375
		2	180	231	0.08	325
		3	180	273	0.08	275
		4	180	333	0.08	225
		5	180	429	0.08	175
	2	6	160	178	0.08	375
		7	160	205	0.08	325
		8	160	242	0.08	275
		9	160	296	0.08	225
		10	160	381	0.08	175
	3	11	140	156	0.08	375
		12	140	179	0.08	325
		13	140	212	0.08	275
		14	140	259	0.08	225
		15	140	333	0.08	175

Table 26. Printgreen CuNi2SiCr Batch 2 process parameters (Layer thickness = 0.03 mm).

Batch	Set	Sample	Power (W)	Scanning Speed (mm/s)	Hatch distance (mm)	VED (J/mm^3)
2	1	1	160	178	0.08	375
		2	160	205	0.08	325
		3	160	242	0.08	275
		4	160	296	0.08	225
	2	5	160	178	0.04	749
		6	160	205	0.04	650
		7	160	242	0.04	551
		8	160	296	0.04	450
	3	9	160	356	0.04	375
		10	160	410	0.04	325
		11	160	485	0.04	275
		12	160	593	0.04	225
	4	13	160	89	0.08	750
		14	160	103	0.08	650
		15	160	121	0.08	550
		16	160	148	0.08	450

In Figure 40 is reported a scheme with all samples produced with the VED range explored in this thesis.

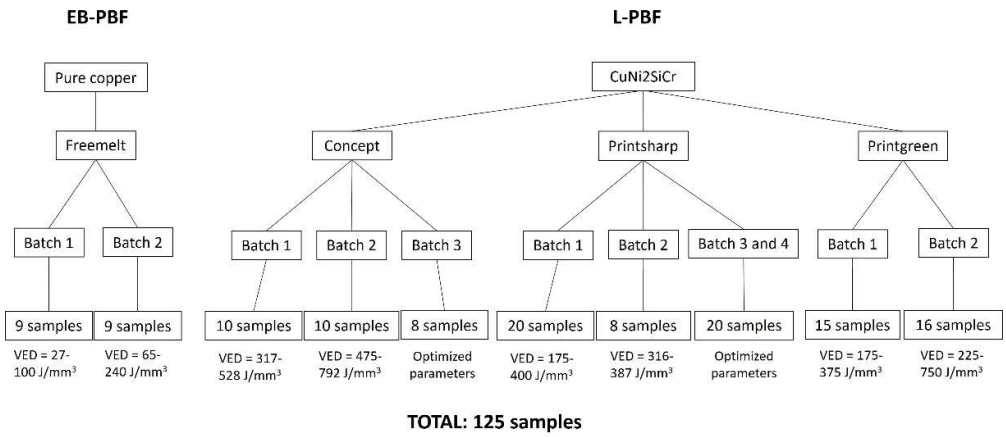

Figure 40. Scheme with all samples produced with the VED range explored in this thesis.

5.5 Heat treatment optimization

The heat treatment optimization was carried out starting from the patented heat treatment (US4191601 [142]) used with the CuNi2SiCr alloy processed by cold working and the optimized heat treatment by Ventura et al. [82] for the C70250 alloy (CuNi3.3Si0.9) produced by L-PBF. The patented heat treatment consists of a solubilization in the range of 870 °C and 980 °C for 1-3 hours followed by water quenching and a double aging heat treatment. The aging process is conducted at 540 °C for 3 hours to allow the precipitation of metal silicides (Ni_2Si, Cr_3Si, Cr_5Si_2), and at 450 °C for 3 hours to facilitate the precipitation of chromium excess from the copper matrix, as reported in the patent [142]. Instead, the heat treatment optimized by Ventura et al., as reported in the introduction section, consists of a direct aging at 450 °C for 8 hours.

The study was conducted on CuNi2SiCr samples manufactured using the Printsharp machine (medium-power red laser system). Two heat treatments were examined (Figure 41): direct aging (DA) at 540°C for a duration ranging from 1 to 6 hours, and a short T6 (S-T6) heat treatment involving solutioning at 930°C followed by water quenching and artificial aging at 540°C for a duration ranging from 1 to 6 hours.

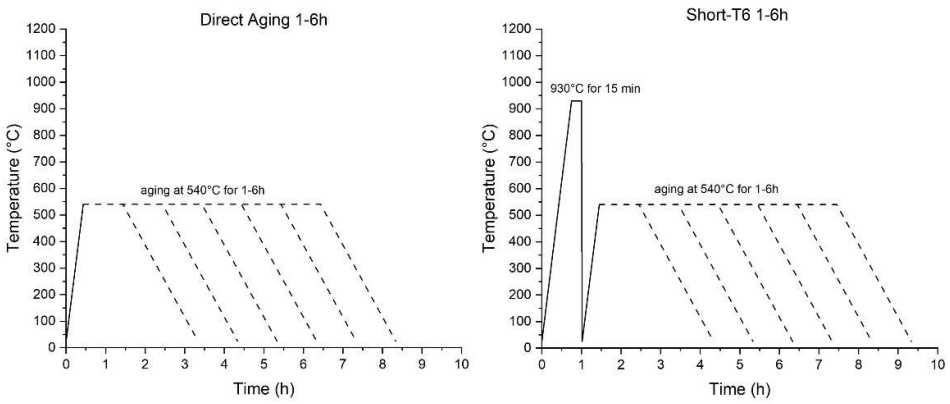

Figure 41. Schematic representation of the heat treatments under investigation.

The solutioning time was chosen based on the dimensions of the dendrite arms (1 μm) observed during the microstructure analysis, and in accordance with a previous study on the heat treatment optimization of a component manufactured via L-PBF [143]. The solutioning temperature (930 °C) and the aging temperature (540 °C) were chosen based on the patented heat treatment, omitting the second aging step.

The samples underwent characterization, including hardness tests to assess their mechanical properties, DSC (Differential Scanning Calorimetry), and XRD (X-Ray Diffraction) analyses to evaluate the evolution of phases and precipitates during the heat treatment. Additionally, their cross-sections were polished for the examination of microstructure and composition.

5.6 Densification with Hot Isostatic Pressing (HIP)

The samples produced using the low-power red laser machine underwent hot isostatic pressing (HIP). Hot isostatic pressing involves subjecting a material to elevated temperature and high isostatic pressure to induce plastic flow, with the purpose of consolidation and densification. The aim of this study was the densification of the samples and the evaluation of the possibility of simultaneously performing the first step of the optimized heat treatment (solutioning). The process was carried out in argon using a pressure of 150 MPa and a temperature of 930°C for two durations: 15 and 60 minutes. The temperature of 930°C and the duration of 15 minutes were selected from the optimized solutioning heat treatment. The duration of 60 minutes was chosen to evaluate a longer exposure to the process. The

pressure of 150 MPa was selected based on the study of Suvorova et al. on the HIPping of CuCrZr alloy [144].

After the heat treatment, the samples underwent characterization, including hardness tests to assess the evolution of the mechanical properties. Additionally, their cross-sections were polished for the examination of microstructure and composition.

5.7 Cu and CuNiSi Sample Characterisation

5.7.1 Microstructural characterization

The specimens were sectioned along the XZ and XY planes (Figure 42), meticulously polished to a smoothness of 0.03 μm, and subjected to etching (following the standard E407-07 [145]) for microstructure observation.

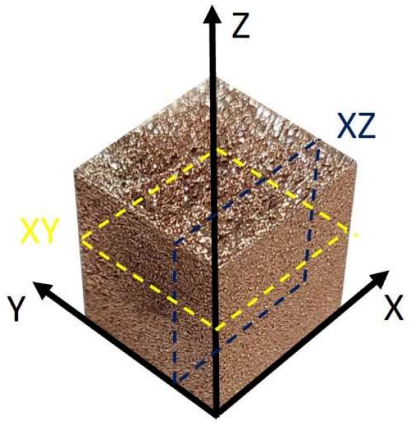

Figure 42. Schematic representation of the cutting planes on the sample.

For the microstructural analyses, three microscopes were used:

- Stereo Microscope (SM) Leica Leica EZ4 W
- Optical Microscope (OM) Leica DMI 5000 M
- Scanning Electron Microscope (SEM) Phenom Pro XL, Thermo Fisher

5.7.2 Electron Backscattered diffraction (EBSD)

Electron Backscattered Diffraction (EBSD) analysis was used to examine the orientation and grain size. Prior to testing, the XZ samples cross-sections were polished to a smoothness of 0.03 μm. EBSD measurements were conducting using a Focus Ion Beam Scanning Electron Microscope (FIB-SEM) S9000G by Tescan equipped with an Oxford EBSD detector.

5.7.3 Relative density

The relative density was calculated using two different methods: pycnometer and image analysis.

5.7.3.1 Pycnometer

The density of both powders and bulk samples was assessed using an Ultrapyc 5000 pycnometer manufactured by Anton Paar. The instrument operates by filling the sample chamber with helium gas at controlled pressure and a temperature of 20 °C. Prior to testing, the sample was accurately weighed. It was then introduced into the pycnometer, resulting in a change in pressure. This pressure change was measured and used to calculate the volume of the sample, allowing for the determination of the skeletal density. The measurements were conducted using a small cell known for its high precision, boasting an accuracy of 0.03% and a repeatability of 0.01%. The testing procedures adhered to the standards outlined in ASTM B923 and ISO 12154[92], [93].

The equation (0.1) was used for evaluating the sample relative density where δ_{bulk} is the skeletal density of the bulk sample and δ_{powder} is the powder skeletal density.

$$Relative\ density = \frac{\delta_{bulk}}{\delta_{powder}} \tag{0.1}$$

5.7.3.2 Image Analysis

The second approach employed to determine the sample relative density involved image analysis. After acquiring images of the specimens with the Leica DMI 5000 M optical microscope, the images were processed using Fiji (ImageJ),

an image processing freeware software [146]. This process included enhancing the image contrast to improve the distinction between pores, dark areas, and the alloy, light areas (Figure 43). The software enables the selection of a color range, and in this instance, the darker range was chosen to calculate the percentage of surface area occupied by our selection in comparison to the total surface area.

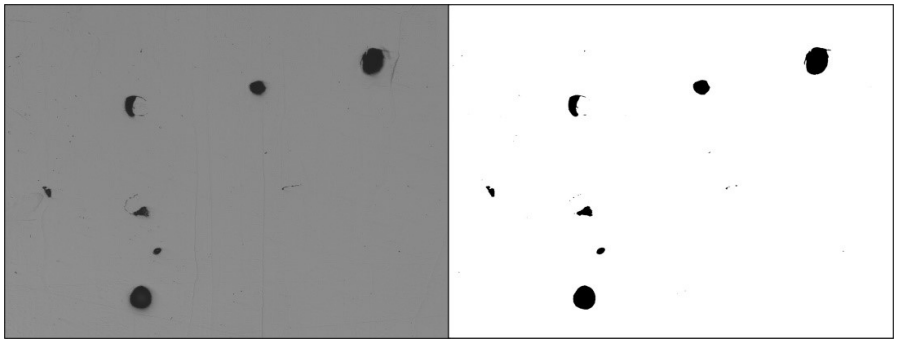

Figure 43. Image captured by optical microscope without graphic processing (left) and with graphic processing (right).

5.7.4 X-rays diffraction (XRD)

X-ray diffraction (XRD) analysis was employed to examine the phase composition of the fabricated specimens. Prior to testing, the samples were prepared by polishing with various SiC grinder papers up to 1200 grit. X-ray measurements were conducted using an Empyrean by Malvern Panalytical diffractometer, utilizing CuKα radiation (λ=0.1504 nm) and covering a 2θ range spanning from 30 to 100°.

5.7.5 Differential Scanning Calorimetry (DSC)

Differential Scanning Calorimetry (DSC) analysis was utilized to investigate the precipitation phenomenon that occurred during the post-process heat-treatment. Before testing, the samples were cut into small pieces weighing approximately 180 mg. Analyses were carried out using a DSC 404 F3 Pegasus Netzsch instrument in an argon atmosphere, employing a heating ramp of 10 °C/min from 25 to 980 °C.

5.7.6 Mechanical tests

5.7.6.1 Hardness

Micro-Vickers hardness was determined using a micro-Vickers indenter with a 100 g load applied for 15 seconds. A minimum of 10 measurements were conducted on the XZ cross-section for each sample following the ASTM E92-17 standard [147].

5.7.6.2 Tensile tests

Flat tensile specimens were manufactured and examined both in their as-built state and after undergoing a heat-treatment process. These specimens were constructed in alignment with the XY plane, parallel to the building platform. Subsequently, all samples were subjected to testing using a Zwick Z050 tensile machine, following the ASTM E8M standard, with a strain rate of $8x10^{-3}$ s^{-1}[148].

5.7.7 Electrical analysis

Flat specimens measuring 6x2x60 mm^3 were produced, oriented parallel to the XY plane in alignment with the building platform. A four-points probe test was then conducted on these samples to assess their electrical conductivity. A schematic representation of the test is shown in Figure 44.

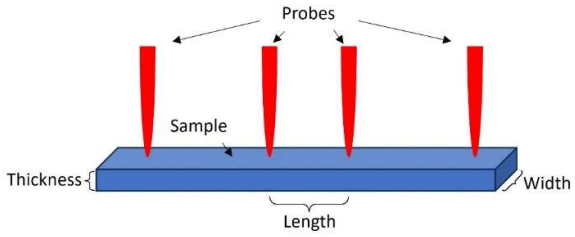

Figure 44. Schematic representation of a four-points probe test.

A known current is applied through the two outer probes, passing through the material being tested. Meanwhile, the voltage drops across the material is precisely measured using the two inner probes. The electrical resistance of the material is then calculated using Ohm's law ((0.2)) where R is the material's electrical resistance, V is the measured voltage and I the known current:

$$R = \frac{V}{i}$$

(0.2)

Then, using the equation (0.3) (where w, t, L and $\boldsymbol{\rho}$ are the width, the thickness, the length and resistivity of the sample, respectively), the resistivity of the sample is calculated.

$$\rho = \frac{R * w * t}{L}$$

(0.3)

Finally, it is worth noting that the inverse of resistivity is electrical conductivity.

Chapter 6

Pure copper

6.1 Electron beam powder bed system

To produce the samples of batch 1, the following parameters were used: P = 720 W, line offset = 0.2 mm, layer thickness = 0.05 mm, and scanning speed in the range of 720-2640 mm/s. Instead for the batch 2 were used: P = 720 W, line offset = 0.2 mm, layer thickness = 0.05 mm, and scanning speed in the range of 300-1100 mm/s.

6.1.1 Process parameters optimization

Relative densities of the produced samples were assessed using a gas-pycnometer.

The relative density analysis for batch 1 yielded unreliable results due to the presence of opened porosities in the samples resulting from unoptimized parameters and the fundamental principle of the pycnometer analysis, which measures only closed porosities. Only samples 7, 8, and 9 exhibited reliable relative densities, measured around 97.5%. These results indicate a need to transition towards higher VED due to the observed increase in the relative densities of the cubes in agreement with the work of Raab et al. [125] .

In Figure 45, the relative densities of 9 samples from batch 2 are reported, correlated with the VED.

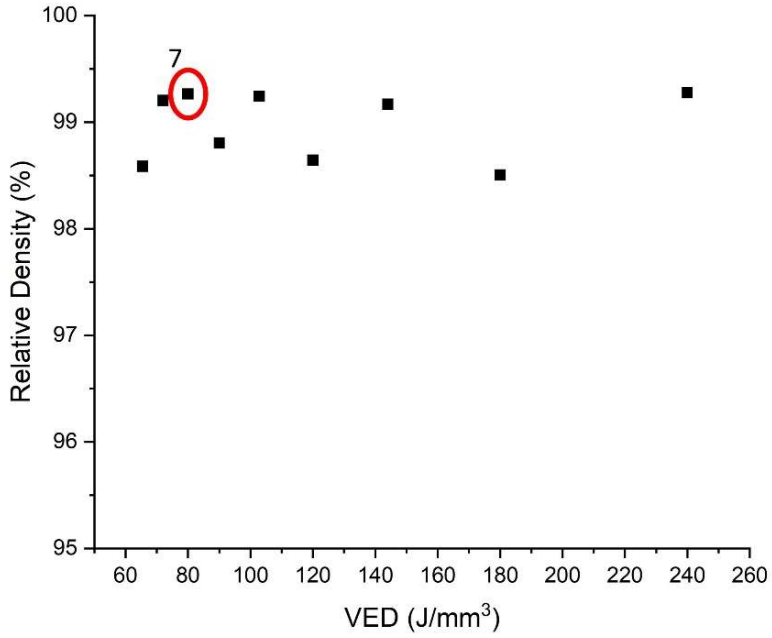

Figure 45. Relative density vs volume energy density of Freemelt ONE pure copper batch 2.

These results reveal that all the samples exhibited a relative density exceeding 98.5%. Among them, five surpassed 99%, with the highest value recorded at 99.3% for sample 7, accompanied by a VED value of 80 J/mm³. These findings contrast slightly with the results obtained in Job 1 for the same VED values. This discrepancy could be attributed to the issues encountered during the production of the first batch. To validate the relative densities measured by pycnometer, image analyses were conducted only on the samples 7. As evident in Figure 46 representing Sample 7 cross-section, the relative density obtained through software analysis aligns well with the pycnometer value and the obtained samples can be considered fully dense.

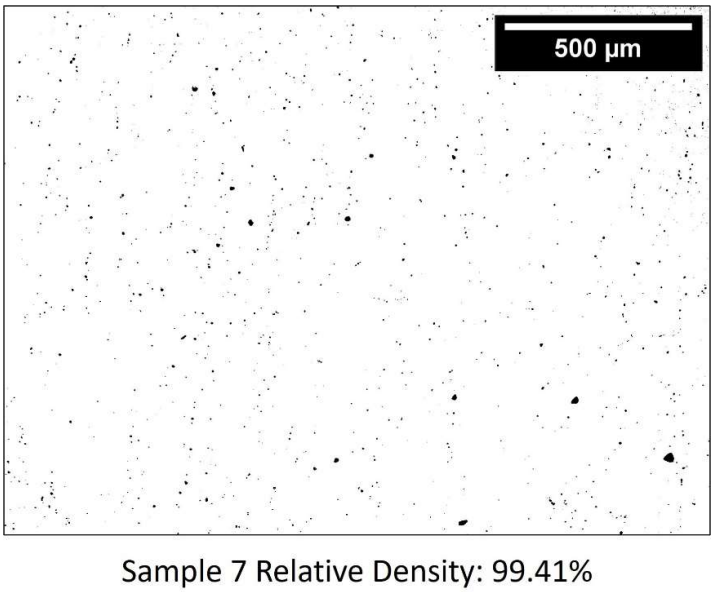

Figure 46. Processed images by ImageJ software of sample 7 of the batch 2 (50X).

The process parameters of the sample 7 of the batch 2 (*P = 720 W (BC = 12mA); v = 900 mm/s; h_d = 200 µm; l_t = 50 µm*) were selected as optimized process parameters.

6.1.2 Optimized sample microstructure

The sample microstructure was examined employing a stereo microscope (SM), an optical microscope (OM), a scanning electron microscope (SEM), and a range of etchants to uncover specific characteristics like melt pools and grains.

The initial examination utilized the optical microscope (OM) with the 30th etchant specified in ASTM E407 Standard (25% NH_4OH + 25% H_2O + 50% H_2O_2) via electro-etching. Figure 47 displays the microstructure of sample 7 from batch 2. The etching revealed the typical EB-PBF microstructure, featuring melt pools with dimensions of 285 ± 30 µm. Furthermore, distinctions between each layer were observable. These disparities stem from the scanning direction of the electron beam, employing a 0-90 scanning strategy. Consequently, alternate layers portray perpendicular cross-sections of the melt pools and parallel ones. Additionally, columnar grains can be observed growing along the build direction, perpendicular to the scanning direction.

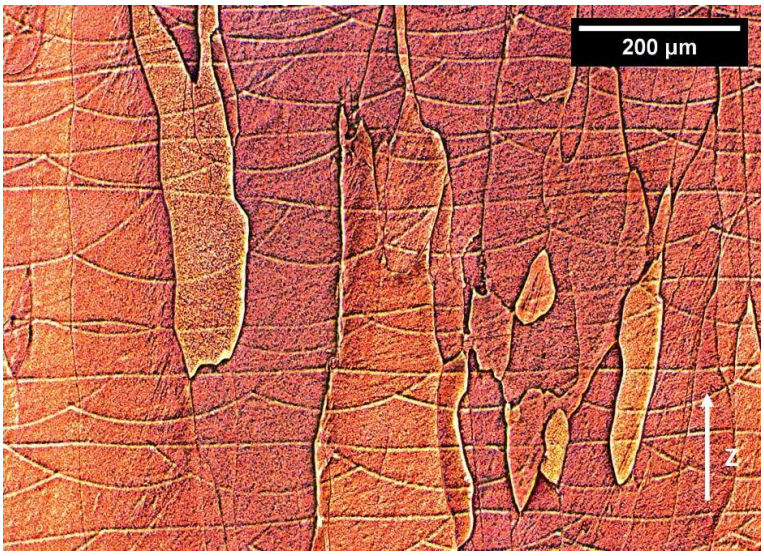

Figure 47. Microstructure of the sample 7 of the batch 2 etched (OM 100X).

A subsequent analysis was conducted using the stereo microscope to investigate grain growth. This microscope was chosen for its suitability to the dimensions of grains produced by EB-PBF technology. In this case, a solution of nitric acid (composed of 50% HNO_3 and 50% H_2O) was utilized to accentuate the grains, and the resulting microstructure is depicted in Figure 48.

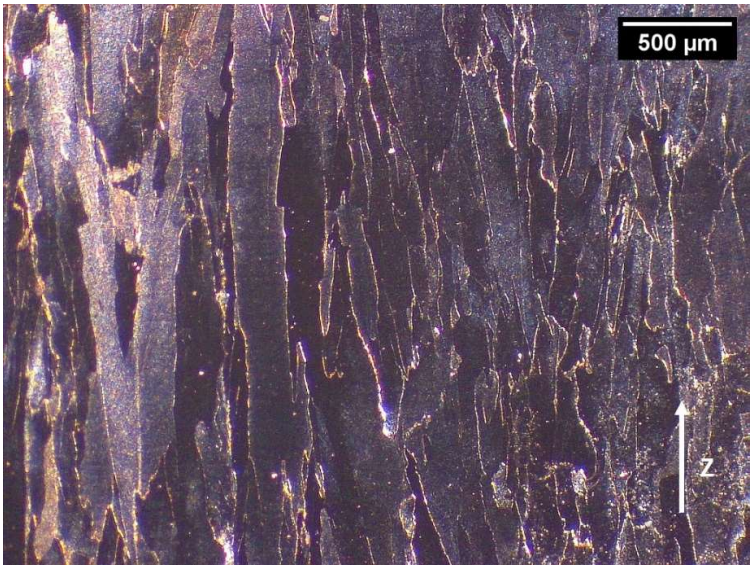

Figure 48. Microstructure of the sample 7 of the batch 2 after etching (SM 16X).

These images illustrate the epitaxial columnar growth of grains, a distinctive feature of additive manufacturing processes. As seen previously in Figure 47, the columnar grains align parallel to the building direction (z), with lengths of millimeters and widths reaching up to 250 µm.

The same etching used for the observation with the optical microscope was used for the scanning electron microscope analysis (electro-etching using 25% NH_4OH + 25% H_2O + 50% H_2O_2 solution) and the results are shown in Figure 49a and b.

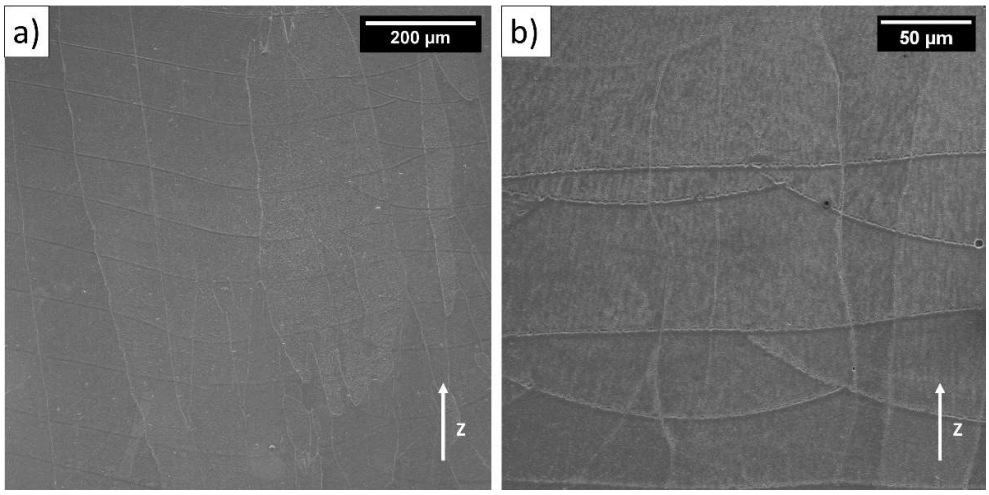

Figure 49. SED SEM images of sample 7 of the batch 2 after etching at different magnifications a) 300X and b) 1000X).

These images once more reveal the microstructure of the sample, specifically illustrating grain boundaries that span across multiple melt pools along the construction axis. This occurrence stems from the heat flow direction perpendicular to the scanning direction, leading to grain crystallization oriented accordingly.

6.1.2.1 Defects

Upon inspecting the images utilized to assess the relative density (Figure 46), it becomes clear that the printed samples were completely dense. The only defects observed were gas porosities, which were always located close to the meltpool borders and an example of them is shown in Figure 50.

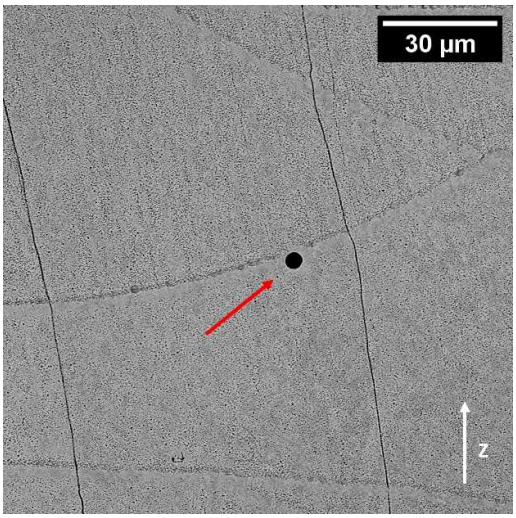

Figure 50. BSE SEM image at 2000X of a gas porosity in the pure copper sample processed with Freemelt ONE machine.

6.1.3 Optimized sample phase and compositional analysis

The analysis of phase content and element distribution was conducted through XRD and EDS SEM analyses.

In Figure 51 are reported the results of XRD analysis performed on Z cross-sections of the samples.

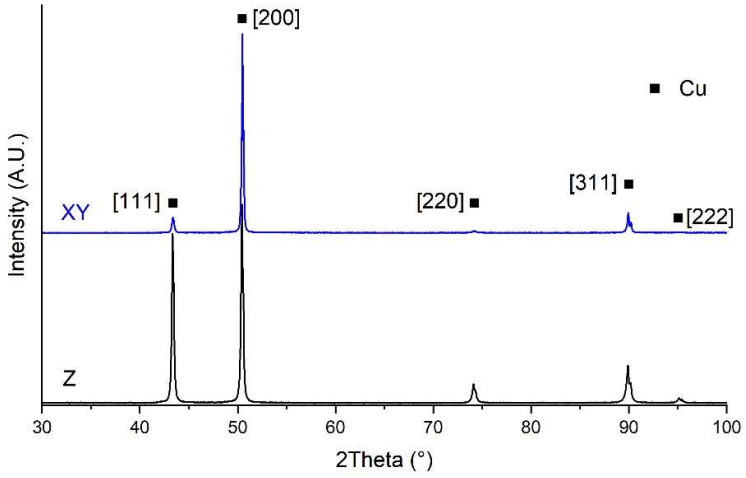

Figure 51. XRD patterns along XY and Z planes of a pure copper sample.

This analysis indicates the presence of the FCC phase and a disparity in peak intensity between the XY and Z cross-sections, with the highest peak at 51° ([200]) for both. The disparity is mainly observed at the peak at 44°, where the intensity is much higher in the Z cross-section than in the XY cross-section. These intensity differences are attributed to the highly anisotropic microstructure, featuring unidirectional columnar grains perpendicular to the scanning direction. The unidirectional columnar grains grew parallel to the build direction due to the combination of parameters, such as line offset and scanning speed, which affect the melt pool geometry and consequently influence the thermal gradient direction. In this case, the thermal gradient is perpendicular to the scanning direction, leading to epitaxial growth parallel to the build direction. In a pure FCC metal like copper, the preferential growth direction is along one of the <001> directions. Therefore, in this case, the growth is parallel to the build direction, which explains why in the XRD pattern of the XY cross-section, the highest peak corresponds to the (200) plane. Such characteristics are typical of materials produced through additive manufacturing methods and can be modified changing the process parameters.

To evaluate the contained elements within the sample, EDS analysis on the Z plane is reported in Figure 52.

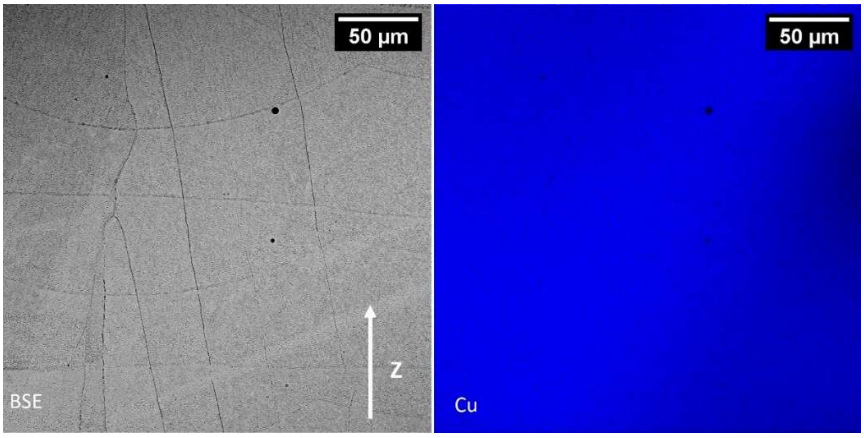

Figure 52. EDS SEM map of a pure copper sample produced by Freemelt ONE machine.

The EDS SEM map indicates the exclusive presence of copper, without any detectable oxide, which is a common occurrence during copper processing.

6.1.4 Optimized sample hardness

A preliminary study of the mechanical properties of these samples were conducted measuring the hardness in the as-built condition. The Vickers microhardness test resulted in a value of 54 ± 9 HV. This value is comparable with the hardness value obtained in the study of Guschlbauer et al. [127] and with the hardness value of the casted annealed pure copper [149].

6.1.5 Discussion

Based on the obtained results, it is clear that the optimal relative density was attained with a VED of around 80 J/mm^3, resulting in a fully dense sample at 99.3%. Despite increasing the VED to higher values, such as 240 J/mm^3, there was no significant alteration in the high relative density observed. These findings align entirely with those reported by Raab et al. [125].

The microstructure of the samples exhibited typical columnar grains parallel to the build direction, characteristic of additive manufacturing technologies, along with the presence of melt pools. The melt pool geometry, influenced by the process parameters, generated a thermal gradient perpendicular to the scanning direction and parallel to the building direction. This resulted in epitaxial growth along the building direction, leading to the observed elongated and vertical grains. For this reason, the grain length extended up to millimeters, crossing many layers. The EB-PBF process, during the pre-heating, melting, and post-heating phases, maintains the material at elevated temperatures throughout, facilitating grain growth. This thermal history also influenced the hardness value; in fact, the resulting hardness of 54 ± 9 HV is comparable with the hardness value of cast annealed pure copper. Furthermore, within the specimens, a few defects such as gas porosities were observed, confirming the high density and the optimization of the process parameters. Finally, the phase and composition analysis revealed the presence of an FCC phase within the samples, indicating exclusively, as expected, the presence of copper.

Chapter 7

CuNi2SiCr alloy

7.1 Low-power red laser system

To produce the samples of batch 1, the following parameters were used: P = 95 W, hatch distance = 0.08-0.10 mm, layer thickness = 0.015 mm, and scanning speed in the range of 120-250 mm/s. For the batch 2 were used: P = 95 W, hatch distance = 0.08-0.10 mm, layer thickness = 0.010 mm, and scanning speed in the range of 120-250 mm/s. The third batch was printed using the optimized process parameters.

7.1.1 Process parameters optimization

The relative densities of the produced samples were determined using a gas-pycnometer. The plotted graph in Figure 53 shows the relative densities of the 20 samples of batches 1 and 2, as functions of the VED.

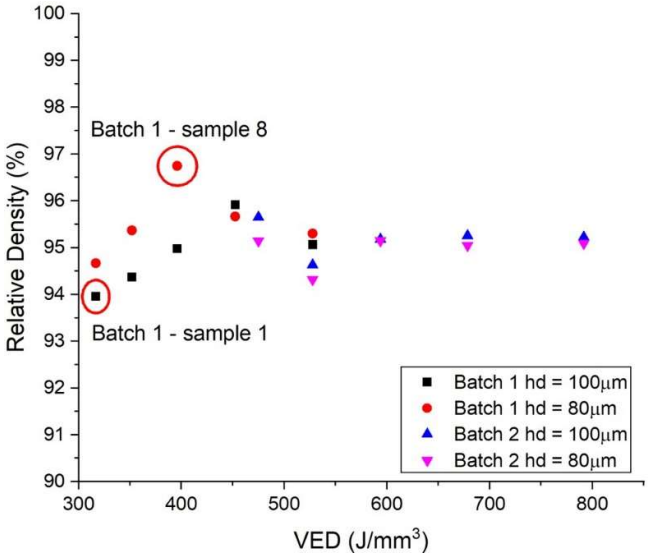

Figure 53. Relative density vs volume energy density of Concept batches 1 and 2.

Starting at 93.96% for sample 1 in batch 1 at 317 J/mm³, it peaks at 96.75% for sample 8 at 400 J/mm³ in the same batch. Subsequent increases in VED result in a gradual decline in relative density, stabilizing around 95% despite the escalating energy density. When varying the hatching distance at VED values lower than 400 J/mm³, there was a reduction in relative density observed as the distance moved from 80 to 100 µm. However, for higher VED values, the resulting relative density values were comparable. The effect of changing the layer thickness can be observed between batch 1 (0.015 mm) and batch 2 (0.010 mm). The layer thickness was adjusted to assess higher VED values, constrained by the very low scanning speed already utilized. However, its effect did not increase the relative density of the samples; instead, it significantly increased the processing time.

To validate the relative densities measured by pycnometer, image analyses were conducted. As evident in Figure 54 representing sample 1 (a) and 8 (b) of batch 1, the relative density obtained through software analysis aligns with the findings.

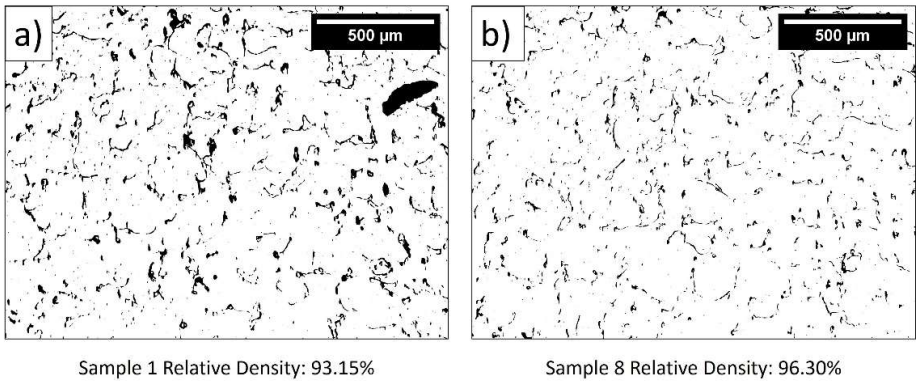

Figure 54. Processed images by ImageJ software of a) sample 1 and b) sample 8 of the batch 1 (50X).

The process parameters of the sample 8 (*P = 95 W; v = 200 mm/s; h_d = 80 µm; l_t = 15 µm*) were used as optimized process parameters for building the third batch.

The third batch was utilized to produce EC samples and parallelepipeds for studying the electrical conductivity and the influence of the size (area) of the part on its relative density, respectively. Figure 55 shows the variation of relative density as a function of the sample area.

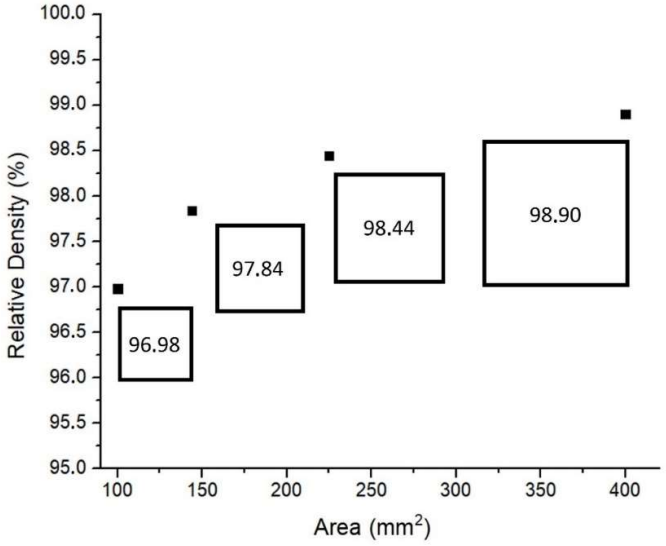

Figure 55. Relative density VS Area of the batch 3.

From the graph, it is evident that with an increase in the sample area (size) from 100 to 400 mm², there is a corresponding rise in relative density, climbing from 96.98 to 98.90%. One plausible hypothesis suggests that as the dimensions of a sample increase, the duration of heat exposure to its internal areas during the manufacturing process also increases. This could prove advantageous for highly conductive materials such as copper, potentially leading to elevated temperatures in the interior regions and contributing to a reduction in porosity.

7.1.2 Optimized sample microstructure

The study of the microstructure involved the use of an optical microscope (OM), a scanning electron microscope (SEM), and various etchants to reveal distinct features such as melt pools and grains.

The initial investigation was carried out at low magnification using the optical microscope (OM) with the 30th etchant specified in the ASTM E407 Standard (25% NH_4OH + 25% H_2O + 50% H_2O_2) through electro-etching. Figure 56 displays the microstructure of sample 8 from batch 1. The etching revealed the typical L-PBF microstructure characterized by melt pools, with dimensions ranging from 75 µm to 100 µm.

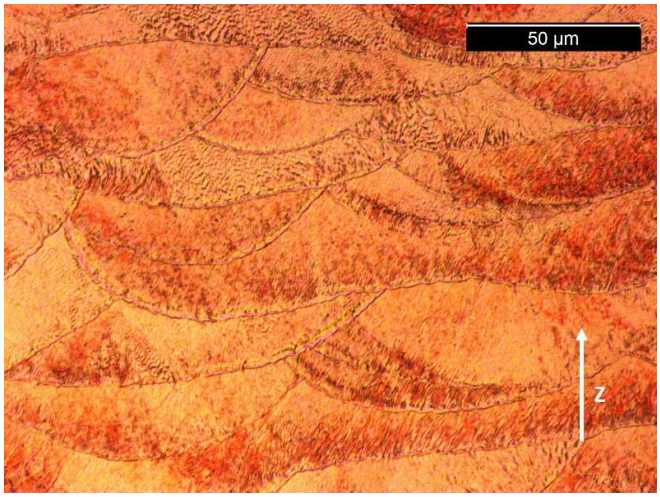

Figure 56. Microstructure of the sample 8 of the batch 1 (OM 500X).

A second investigation was conducted with the same instrument to study grain growth. For this purpose, a nitric acid solution (50% HNO_3 + 50% H_2O) was used, and the resulting microstructure is presented in Figure 57.

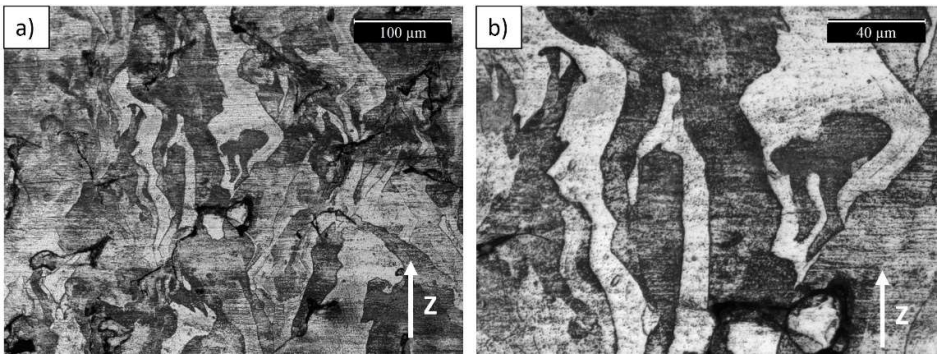

Figure 57. Columnar grain structure of the sample 8 of the batch 1 along the building direction (Z) at a) OM 200X and b) OM 500X.

These micrographs represent the epitaxial columnar growth of grains, a characteristic feature of an AM process. The columnar grains align parallel to the building direction (z) with a slight zig-zag pattern, and their dimensions can reach hundreds of microns, with sizes as large as 60 µm.

A third investigation was effectuated at higher magnification using a SEM and the 40th Etchant in ASTM E407 Standard (5 grams of $FeCl_3$ + 16 mL HCl + 60 ml C_2H_5OH). This etching allows to observe melt pools and grains as showed in Figure 58.

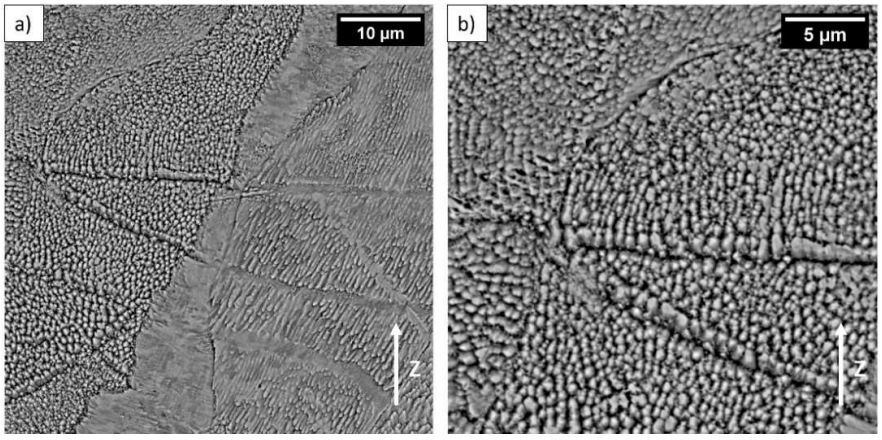

Figure 58. BSE SEM images after etching at different magnifications a) 5000X and b) 10000X).

These images clearly enable the observation of cellular dendrites oriented in different directions with dimensions of about 1 µm. Additionally, one can observe grain boundaries traversing various melt pools along the building direction. The observed phenomenon arises from the perpendicular heat flow direction to the scanning direction, resulting in the crystallization of grains along that specific orientation. A very similar microstructure was also observed by Zhang et al. with the K220 alloy [78].

7.1.2.1 Defects

Since the images (Figure 54) used for the evaluation of the porosities, including that of the optimized sample, clearly showed that the printed samples were full of defects, this section reports some pictures of them. The main defects consist in un-melted powder, cracks and lack of fusions as showed in Figure 59. These defects were uniformly distributed throughout the samples. They stem from insufficient laser power, hindering proper and thorough fusion of the powder, thus resulting in the creation of porous samples.

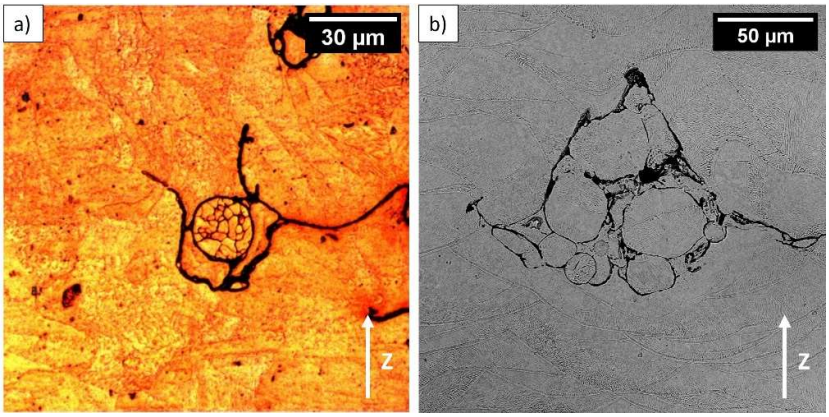

Figure 59. un-melted powder, cracks and lack of fusion a) OM 500X and b) BSE SEM 1250X.

7.1.3 Phase and compositional analysis

The analysis of phase content and element distribution was conducted through XRD and EDS SEM analyses.

In Figure 60 are reported the results of XRD analysis performed on XY and Z cross-sections of the samples.

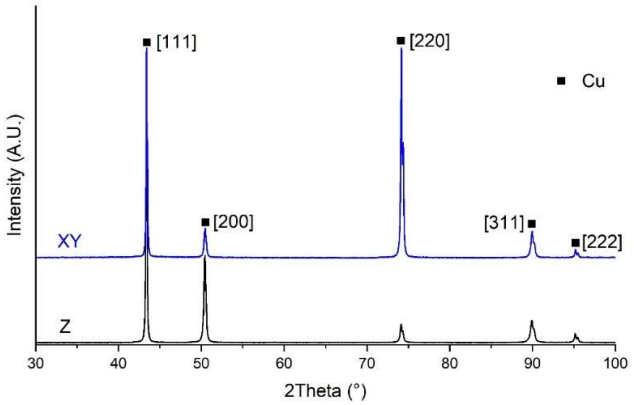

Figure 60. XRD patterns along XY and Z planes of a CuNi2SiCr sample produced by Concept machine.

This analysis reveals the presence of the FCC phase and a disparity in peak intensity between the XY and Z cross-sections, with the highest peak at 74° ([220] lattice plane) and 43° ([111] lattice plane), respectively. This variation in intensities is attributed to the anisotropic microstructure characterized by unidirectional columnar grains perpendicular to the scanning direction, typical of samples produced by L-PBF. The XRD pattern of the XY cross-section is quite different compared to the XY of pure copper processed by EB-PBF. The highest peak depends on the orientation and growth of the grains during the building process. In this case, the process parameters influenced the melt pool geometry, resulting in a thermal gradient direction at a 45° angle to the build direction. The grains grew along this direction, leading to the <110> orientation being parallel to the build direction and, therefore, the highest peak corresponding to the [220] lattice plane.

The exclusive detection of the FCC phase could be attributed to various factors. Firstly, nickel is the second-most abundant element in the alloy (2.4 wt%) and exhibits complete miscibility with copper, remaining in solid solution with it. Secondly, the remaining nickel content, which did not participate in the solid solution, falls below the detection limit (2%) of the XRD instrument.

To evaluate the element distribution in the sample, EDS analysis on the Z plane is reported in Figure 61.

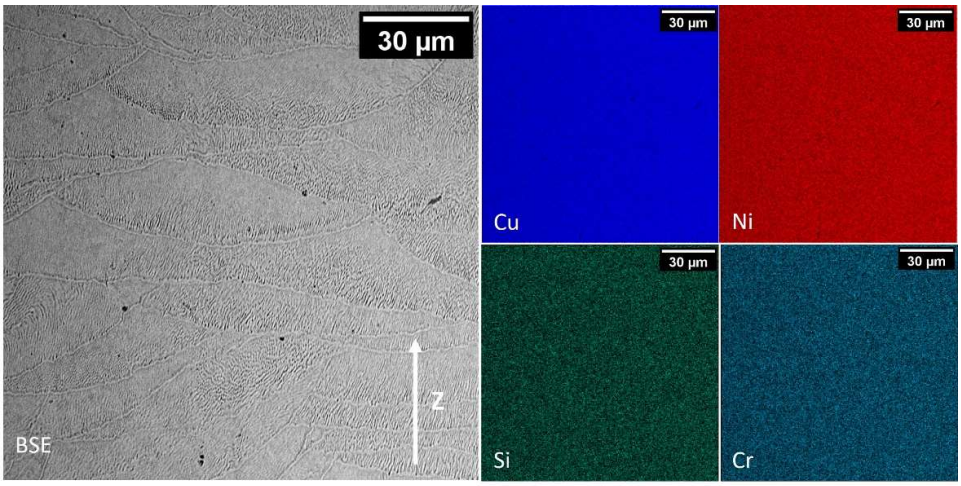

Figure 61. EDS SEM map of a CuNi2SiCr sample produced by Concept machine.

The EDS SEM map shows a uniform distribution of Cu, Ni, Si and Cr throughout the entire sample, with no variation in their contents along the melt pool boundaries. This homogeneity confirms the solid solution of Cu, Ni, Si and Cr.

7.1.4 Hardness and electrical conductivity

A preliminary study of the mechanical properties and the electrical conductivity of this alloy was conducted measuring the hardness and the electrical conductivity of the as-built printed samples.

The Vickers microhardness test resulted in a value of 93 ± 11 HV while the 4 points test yielded an electrical conductivity value of 5.62 MS/m, corresponding to 9.8% IACS. This electrical conductivity value is lower than that obtained by Ventura et al. [86] (14% IACS) and this is due to the high content of porosities, which interrupt the copper matrix reducing the electrical conductivity.

7.1.5 Discussion

From the obtained results, it is evident that the best outcome in terms of relative density was achieved using a VED of approximately 400 J/mm^3, corresponding to a value of 97.52 ± 0.73 %. The density value also depends on the geometry and size of the part, leading to an increase as the dimensions grow. By doubling the side of the test specimen (cube) from 10 mm to 20 mm, a density value of 98.9% was

reached. This phenomenon can be explained by the prolonged exposure to heat, resulting in improved densification.

Nevertheless, the microstructure exhibits typical columnar grains parallel to the build direction with a slight zig-zag pattern, characteristic of additive manufacturing technologies, along with the presence of melt pools. Furthermore, within the specimens, numerous defects such as lack of fusion, unfused particles, and cracks can be observed. These defects are attributed to the laser power being too low, preventing proper and complete fusion of the powder, leading to the formation of porous samples. These porosities have a negative impact on both mechanical and electrical properties. The obtained electrical conductivity value is 9.8% IACS, which is lower than the 14% IACS reported by Ventura et al. [86].

The phase analysis unveiled a FCC phase within the samples, whereas the composition analysis indicated the presence of Ni, Si, and Cr that thus create a solid solution with the Cu. This occurrence is attributed to the low concentration of elements in the alloy and the exceptionally rapid cooling rate during the building process, resulting in a supersaturated solid solution.

7.2 Medium-power red laser system

To produce the samples of batch 1, the following parameters were used: P = 360 W, hatch distance = 0.08-0.10 mm, layer thickness = 0.030 mm, and scanning speed in the range of 300-857 mm/s. For the batch 2 were used: P = 360 W, hatch distance = 0.10 mm, layer thickness = 0.030 mm, and scanning speed in the range of 310-380 mm/s. The batches 3 and 4 were printed using the optimized process parameters.

7.2.1 Process parameters optimization

Relative densities of the produced samples were assessed using a gas-pycnometer, following the methodology previously employed for low-power red laser samples. In Figure 62, the relative densities of 20 samples from batches 1 are reported, correlated with the VED.

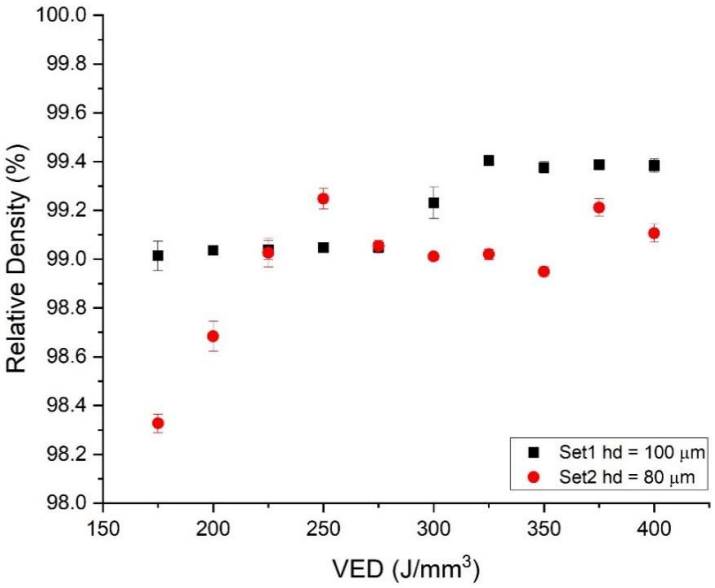

Figure 62. Relative density vs volume energy density of Printsharp batch 1.

The graph shows two distinct trends as a function of hd (sets 1 and 2). Set 1, featuring a hatching distance of 100 µm, demonstrated a certain stability, starting from a relative density value of 99% and maintaining it consistently for VED values between 175 and 275 J/mm³. Upon increasing the VED beyond 325 J/mm³, a relative density value of 99.4% was attained and remained constant despite the increase in energy density. On the other hand, set 2, featuring a hatching distance of 80 µm, exhibited a certain instability. Starting from a relative density value of 98.3%, it gradually increased, peaking at 250 J/mm³ with a relative density of 99.3%. Subsequently, it slightly decreased to 99% and remained close to this value for any increase in the VED value.

Based on these results, the second batch was printed following the set 1, within the VED range of 315-390 J/mm³ (the highest values of relative density of the set 1 with hd of 100 µm), to narrow down the energy density range and achieve the highest relative density. In Figure 63 the relative densities results of the batch 2 are reported.

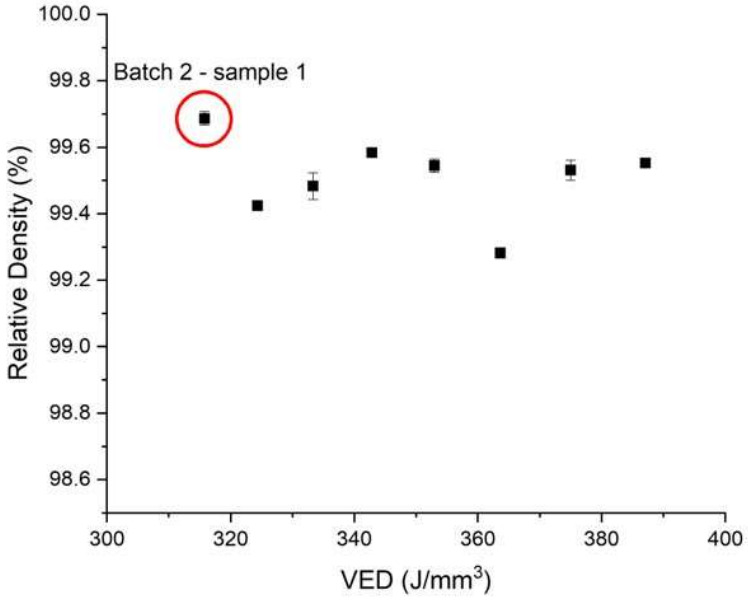

Figure 63. Relative density vs volume energy density of Printsharp batch 2.

This batch revealed that most of the samples exhibited a relative density exceeding 99.4%, reaching the highest value of 99.7% (sample 1) with a VED value of 316 J/mm³. To validate the relative densities measured by pycnometer, image analyses were conducted only on the sample 1. As evident in Figure 64 representing sample 1 cross-section, the relative density obtained through software analysis well aligns with the pycnometer value.

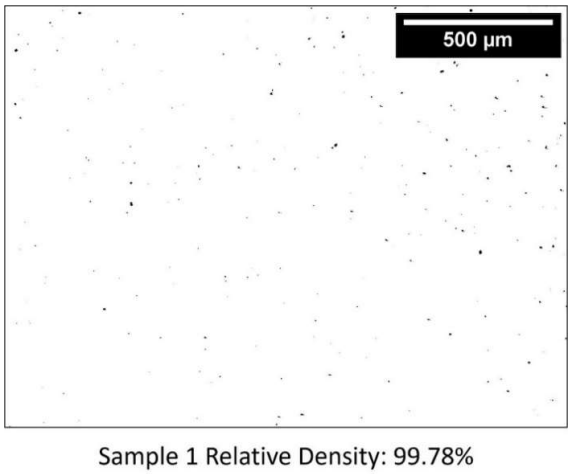

Figure 64. Processed images by ImageJ software of sample 1 of the batch 2 (50X).

The process parameters of the sample 1 of the batch 2 (*P = 360 W; v = 380 mm/s; h_d = 100 µm; l_t = 30 µm*) were selected as optimized process parameters.

7.2.2 Optimized sample microstructure

The preliminary examination was conducted at a lower level of magnification utilizing an OM and the 30th etchant outlined in the ASTM E407 Standard (25% NH_4OH + 25% H_2O + 50% H_2O_2) through the process of electro-etching. Figure 65 shows the microstructure of sample 1 from batch 2. The etching unveiled the standard microstructure of L-PBF, as already observed with samples produced with low-power, featuring melt pools with dimensions ranging from 150 to 190 µm in this instance. The size of these melt pools is larger than those found in the samples produced using the Concept machine. This variance can be attributed to the different size of the laser spot.

Figure 65. Microstructure of the sample 1 of the batch 2 produced by Printsharp machine (OM 100X).

A subsequent examination was carried out using the same instrument to explore grain growth. In this case, a solution of nitric acid (comprising 50% HNO_3 and 50% H_2O) was employed, and the resulting microstructure is depicted in Figure 66.

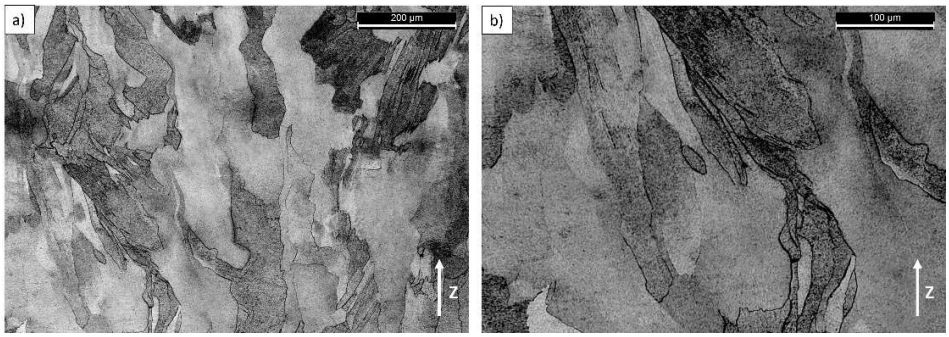

Figure 66. Columnar grain structure of the sample 1 of the batch 2 along the building direction (z) at a) OM 100X and b) OM 200X.

These pictures illustrate the epitaxial columnar growth of grains, as previously observed in the low-power samples that is a distinctive trait of an additive manufacturing process. The columnar grains align parallel to the building direction (z) with a slight zig-zag pattern, with dimensions extending up to hundreds of microns and reaching sizes as large as 170 µm. A subsequent investigation, conducted at higher magnification using a scanning electron microscope (SEM) and the 40th etchant in accordance with ASTM E407 Standard (5 grams of $FeCl_3$ + 16 mL HCl + 60 ml C_2H_5OH), revealed melt pools and grains simultaneously, as demonstrated in Figure 67.

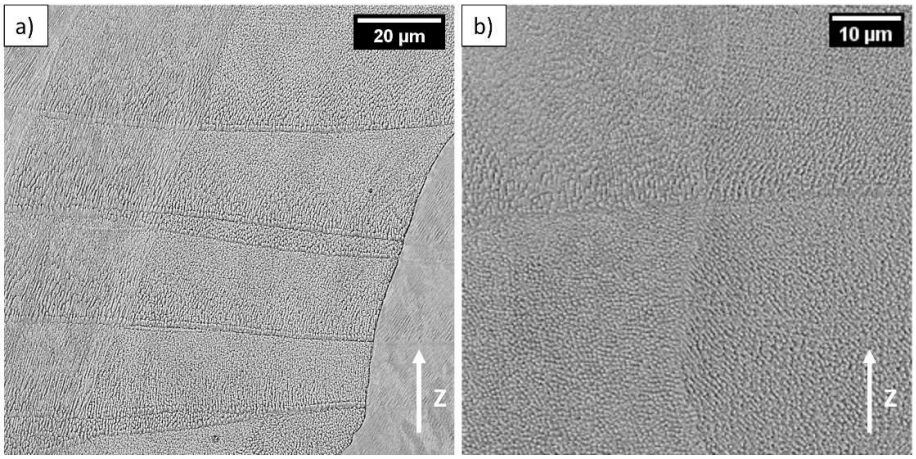

Figure 67. BSE SEM images after etching at different magnifications a) 2500X and b) 4000X.

These images display a clear view of cellular dendrites oriented in various directions, each measuring approximately 1 µm. Additionally, the images show grain boundaries traversing multiple melt pools along the construction axis. This

phenomenon arises from the perpendicular heat flow direction to the scanning direction, resulting in grain crystallization along that specific orientation. Significantly, this microstructure exhibits a notable similarity to observations in samples produced utilizing a low-power red laser and those made by Zhang et al. on the K220 alloy [78].

7.2.2.1 Defects

Upon examining the images used for evaluating the relative density (Figure 52), it is evident that the printed samples were fully dense. The few defects observed include gas porosities and sporadic lack of fusion, as shown in Figure 68.

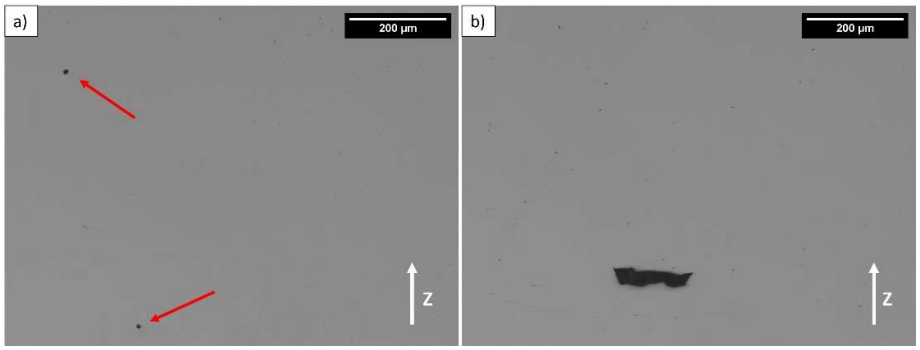

Figure 68. OM 100X images of a) gas porosities and b) lack of fusion.

This result stands in contrast to the outcomes obtained with the low-power red laser machine, highlighting the sufficient energy used with the medium-power laser to completely melt the powder and achieve almost fully dense samples.

7.2.3 Phase and compositional analysis

The analysis of phase content and element distribution was conducted through XRD and EDS SEM analyses.

In Figure 69 are reported the results of XRD analysis performed on XY and Z cross-sections of a sample.

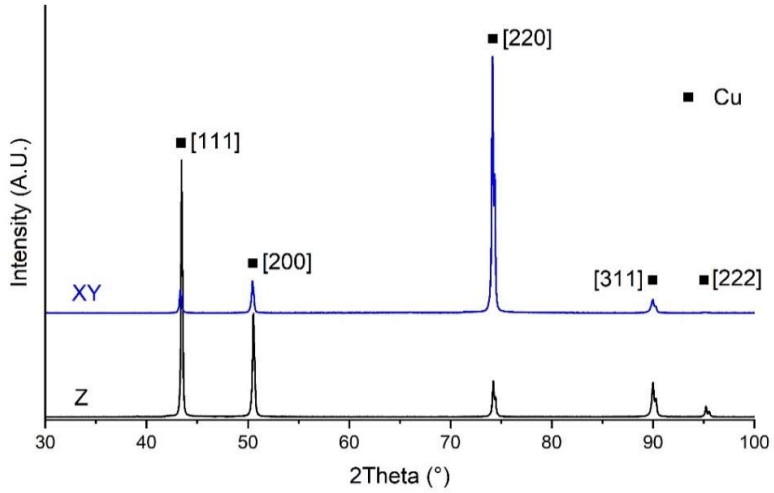

Figure 69. XRD patterns along XY and Z planes of a CuNi2SiCr sample produced by Printsharp machine.

As observed previously with the low-power red laser, this analysis shows the presence of the FCC phase alongside a significant disparity in peak intensity between the XY and Z cross-sections. Notably, the peak intensity reaches its maximum at 74° ([220] lattice plane) in the XY section, and at 43° ([111] lattice plane) in the Z section. Such intensity variations are attributed to the highly anisotropic microstructure characterized by unidirectional columnar grains perpendicular to the scanning direction, a characteristic often observed in samples fabricated via L-PBF. As observed in the XRD pattern of the AB sample produced by the Concept machine, the highest peak at 74° (corresponding to the [220] lattice plane) indicates an orientation of the grains with the <110> direction parallel to the build direction. This suggests a melt pool geometry that results in a thermal gradient direction at a 45° angle to the build direction. The difference in intensity of the [220] plane peak relative to the [111] plane peak between the Concept (lower) and Printsharp (higher) machines can be attributed to a higher texture in the Printsharp samples, due to the use of higher laser power compared to the Concept samples.

The exclusive identification of the FCC phase could be ascribed to several factors. Firstly, nickel is the second-most abundant element in the alloy (2.4 wt%) and exhibits complete miscibility with copper, remaining in solid solution with it. Secondly, the remaining nickel content, which did not participate in the solid solution, falls below the detection limit (2%) of the XRD instrument.

In order to assess the elemental distribution within the sample, EDS analysis on the Z plane is presented in Figure 70.

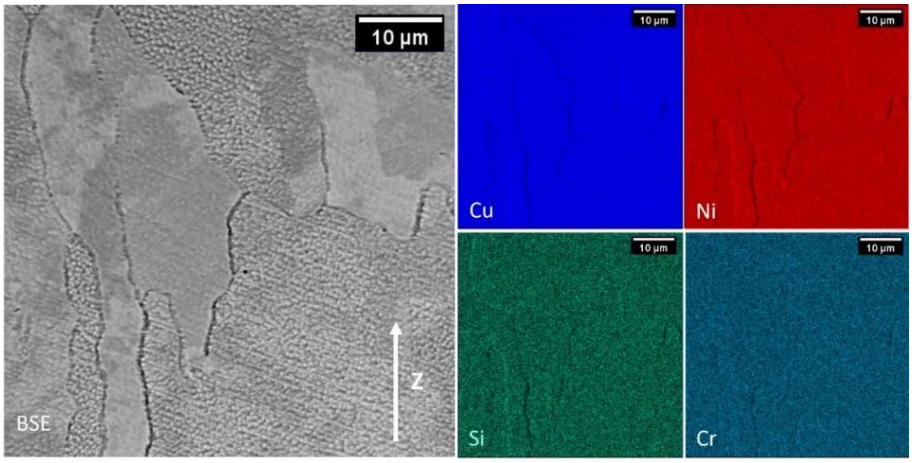

Figure 70.EDS SEM map of a CuNi2SiCr sample in the AB condition produced by Printsharp machine.

The EDS SEM map demonstrates a consistent dispersion of Cu, Ni, Si, and Cr across the entirety of the sample, without any discernible fluctuation in their concentrations along the boundaries of the melt pool. This uniformity validates the solid solution of Cu, Ni, Si, and Cr.

7.2.4 Hardness

A preliminary study of the mechanical properties of these samples were conducted measuring the hardness in the as-built condition. The Vickers microhardness test resulted in a value of 104 ± 3 HV.

7.2.5 Discussion

Based on the obtained results, it is possible to assess that the optimal relative density was achieved at a VED of approximately 316 J/mm^3, resulting in a fully dense sample at 99.7%. However, even with higher VED values of up to 390 J/mm^3, the relative density remained above 99.2%. The different results respect to the low-power samples can be attributed to variations in laser power. Below a certain threshold, the laser fails to fully melt the powder. However, with the application of a 360 W laser power, despite a lower VED (316 J/mm^3) than that used in the low-power red laser samples (400 J/mm^3), the powder achieved full melting. The

resulting high relative density correlates with a low incidence of defects, primarily comprising gas porosities and sporadic lack of fusion.

The microstructure of the samples revealed typical columnar grains aligned parallel to the build direction with a slight zig-zag pattern, a characteristic commonly observed in additive manufacturing technologies. These grains were accompanied by the presence of melt pools, consistent with observations made in the low-power samples. Notably, the size of the melt pools in the current samples was nearly double that of the low-power samples and the grain width. This discrepancy can be attributed to the differing laser spot sizes of the machines, which measure 100 μm and 50 μm, respectively. Furthermore, the length of the grains extended to several hundreds of microns, mirroring observations from the low-power samples.

Phase analysis and composition analysis further substantiated the findings from the low-power samples, confirming the presence of a FCC phase within the samples. Additionally, Ni, Si, and Cr were identified to be in solid solution with the Cu matrix.

Finally, the hardness value of 104 ± 3 HV is slightly higher than that of the low-power samples (93 ± 11 HV), although it remains comparable.

7.3 Low-power green laser system

To produce the samples of batch 1, the following parameters were used: P = 140-160-180 W, hatch distance = 0.08 mm, layer thickness = 0.030 mm, and scanning speed in the range of 156-429 mm/s. For the batch 2 were used: P = 160 W, hatch distance = 0.04-0.08 mm, layer thickness = 0.030 mm, and scanning speed in the range of 89-593 mm/s.

7.3.1 Process parameters optimization

The relative densities of the printed samples were evaluated using a gas-pycnometer, employing the same methodology as previously utilized for samples from low-power and medium red lasers. Figure 71 presents the relative densities of 15 samples from batch 1, depicted alongside their correlated VED values.

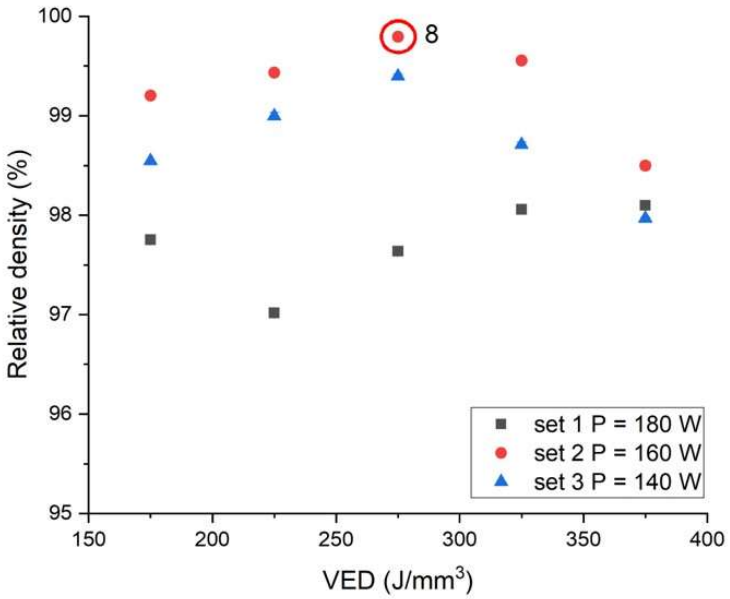

Figure 71. Relative density vs volume energy density of Printgreen batch 1.

The graph shows 3 distinct trends as a function of the laser power (sets 1, 2 and 3). Set 1, with a laser power of 180 W, exhibited relative density values below 98%. It began with a relative density of 97.7% at a VED of 175 J/mm³, decreased to 97.0% at 225 J/mm³, and then increased to 98.0% for higher VED values. Set 2, featuring a laser power of 160 W, demonstrated the most favorable parameter combination. Starting at a relative density of 99.2%, it steadily rose, reaching a peak of 99.7% at 275 J/mm³, before slightly declining to 98.5%. As for set 3, with a laser power of 140 W, it displayed a behavior comparable to set 2, although with lower relative density values. Commencing at 98.5%, it progressively increased, peaking at 99.4% at 275 J/mm³, then slightly diminishing to 98.1%.

Based on these findings, the second batch was printed following the parameters of set 2, employing a laser power of 160W, while modifying the scanning strategy (rotation of 67°) and assessing two sets of hatching distance and scanning speed. Notably, samples 1 and 2 were not fully completed, as apparent from Figure 39. This was attributed to the curling of the initial layers, resulting in their premature termination. Nonetheless, the remaining portion of the batch was successfully completed, and the relative density results are presented in Figure 72.

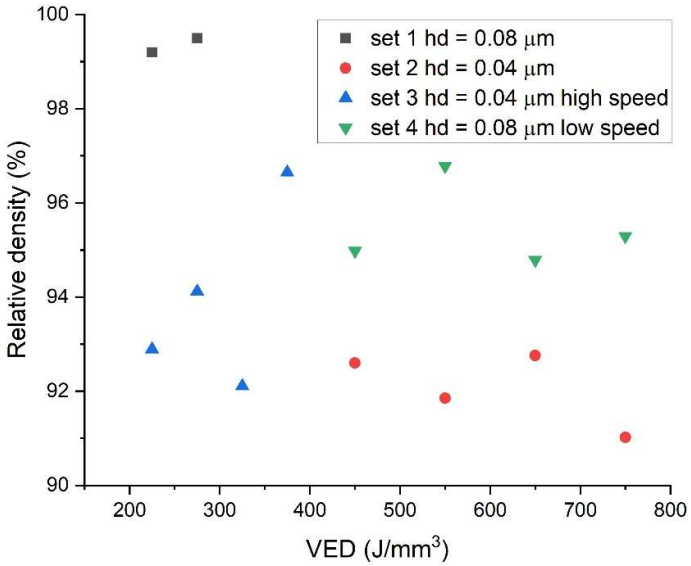

Figure 72. Relative density vs volume energy density of Printgreen batch 2.

This batch indicated that altering the hatching distance from 0.08 to 0.04 mm and adjusting the scanning speed to maintain a VED value between 225 and 750 J/mm³ resulted in a reduction in relative density. When examining the VED range of 225 and 375 J/mm³ with sets 1 and 3, set 1 (manufactured using parameters identical to batch 1 set 2 but with a scanning strategy changed from 0-90° to a rotation of 67°) achieved results comparable to set 2 of batch 1, thus yielding the highest relative density within this batch with a value of 99.5%. On the contrary, set 3 yielded considerably lower values, with the highest relative density recorded at 96.9%. Concerning the second VED range of 450 to 750 J/mm³ with sets 2 and 4, both sets achieved low relative density values ranging from 91% to 97%.

To validate the relative densities obtained from the pycnometer measurements, image analyses were exclusively performed on sample 8. As evident in Figure 73 representing sample 8 cross-section, the relative density obtained through software analysis aligns well with the pycnometer value.

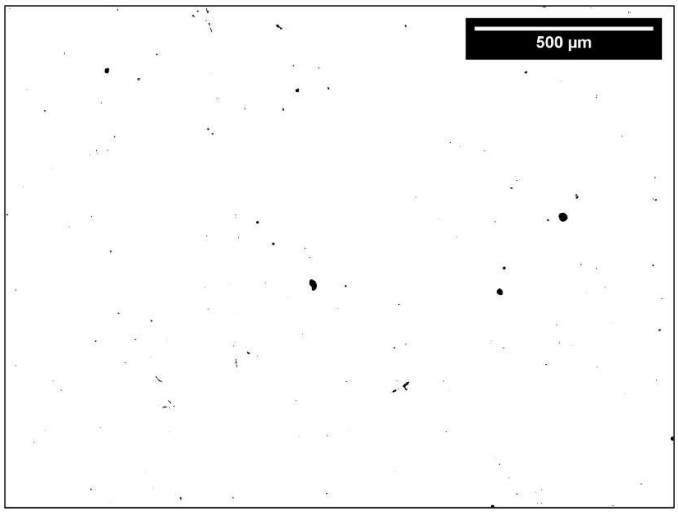

Figure 73. Processed images by ImageJ software of sample 8 of the batch 1 (50X).

The process parameters of the sample 8 of the batch 1 (*P = 160 W; v = 242 mm/s; hd = 80 µm; lt = 30 µm*) were selected as optimized process parameters.

7.3.2 Optimized sample microstructure

The examination of the microstructure involved the use of tools such as an optical microscope (OM), a scanning electron microscope (SEM), and different etchants. These methods were employed to reveal distinct features such as melt pools and grains, following a methodology akin to that used for samples produced with low-power red lasers.

The preliminary examination was conducted at a lower level of magnification utilizing an OM and the 30th etchant outlined in the ASTM E407 Standard (25% NH_4OH + 25% H_2O + 50% H_2O_2) through the process of electro-etching. Figure 74 shows the microstructure of sample 8 from batch 1. The etching unveiled the standard microstructure of L-PBF, as already observed with samples produced with low-power, featuring melt pools with dimensions ranging from 150 µm to 180 µm in this instance. The size of these melt pools is larger than those observed in the samples produced using the Concept machine and comparable to those found in the Printsharp one. This variance can be attributed to the different size of the laser spot.

Figure 74. Microstructure of the sample 8 of the batch 2 produced by Printgreen machine (OM 200X).

A follow-up analysis was conducted utilizing the same instrument to investigate grain growth. In this case, a solution of nitric acid (composed of 50% HNO3 and 50% H2O) was utilized, mirroring the approach used for the red laser samples. The resulting microstructure is illustrated below in Figure 75.

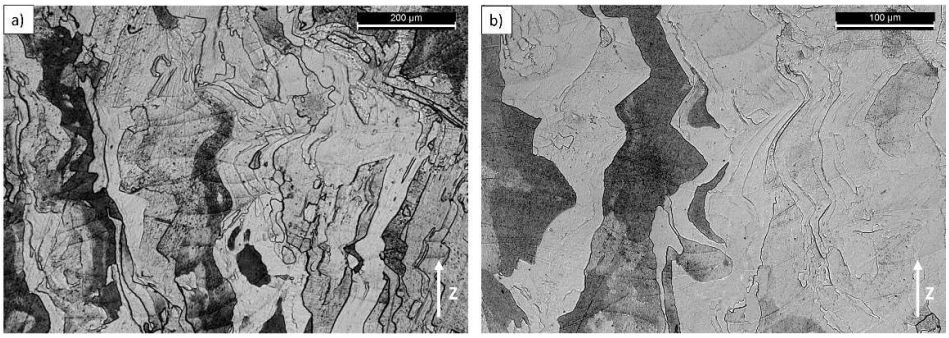

Figure 75. Columnar grain structure of the sample 8 of the batch 2 along the building direction (z) at a) OM 100X and b) OM 200X.

These images show the epitaxial columnar growth of grains, a characteristic previously noted in the red laser samples and indicative of an additive manufacturing process. The columnar grains align parallel to the building direction

(z) with a slight zig-zag pattern, with dimensions ranging up to hundreds of microns and reaching sizes as large as 100 μm.

The same condition used for the observation with the optical microscope was used for the subsequent scanning electron microscope analysis conducted at higher magnification (electro-etching using 25% NH4OH + 25% H2O + 50% H2O2 solution) and the results are shown in Figure 76a and b.

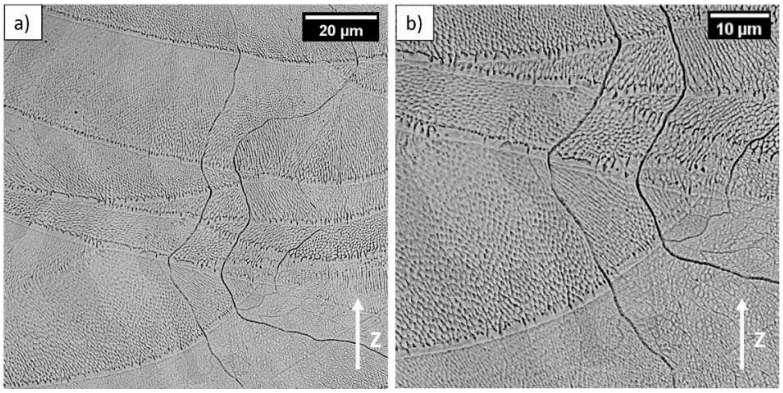

Figure 76. BSE SEM images after etching at different magnifications a) 2500X and b) 4000X.

These images display a clear view of cellular dendrites oriented in various directions, each measuring approximately 1 μm. Additionally, the images show grain boundaries traversing multiple melt pools along the construction axis. This phenomenon arises from the perpendicular heat flow direction to the scanning direction, resulting in grain crystallization along that specific orientation. Significantly, this microstructure exhibits a notable similarity to observations in samples produced utilizing a low-power and a medium-power red laser.

7.3.2.1 Defects

From the image used to evaluate the relative density (Figure 73), it is possible to state that the printed samples exhibited full density. The only defects observed were gas porosities, predominantly situated within grains, with an example represented in Figure 77.

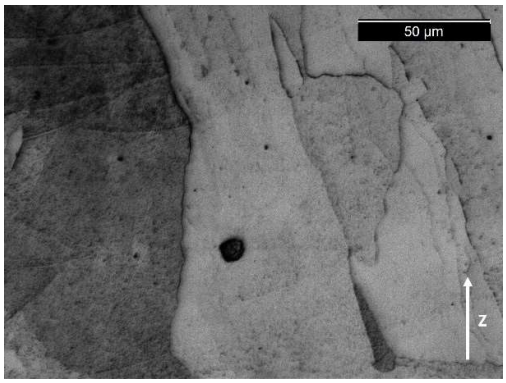

Figure 77. OM 500X image of a gas porosity.

7.3.3 Phase and compositional analysis

The analysis of phase content and element distribution was conducted through XRD and EDS SEM analyses.

In Figure 78 are reported the results of XRD analysis performed on XY and Z cross-sections of a sample.

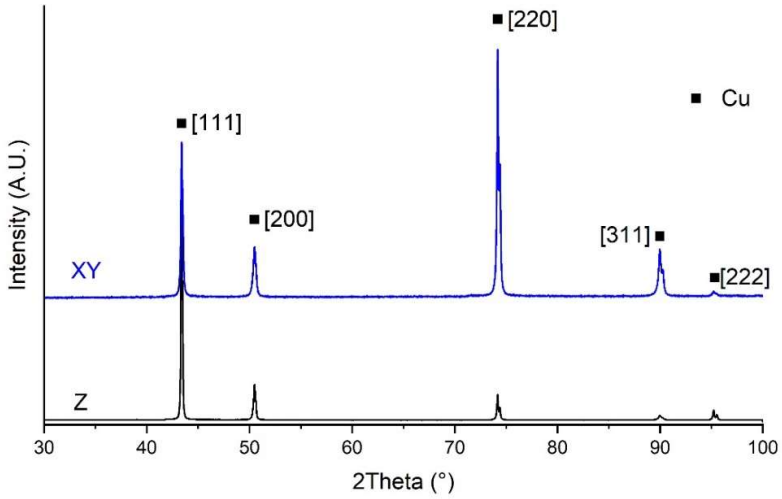

Figure 78, XRD patterns along XY and Z planes of a CuNi2SiCr sample produced by Printgreen machine.

As previously observed with low-power and medium-power red lasers, this analysis reveals the presence of the copper phase alongside a significant difference

in peak intensity between the XY and Z cross-sections. Notably, the peak intensity reaches its maximum at 74° ([220] lattice plane) in the XY section and at 43° ([111] lattice plane) in the Z section. These intensity variations stem from the anisotropic microstructure characterized by unidirectional columnar grains perpendicular to the scanning direction, a trait frequently observed in samples produced via L-PBF, as noted numerous times in this thesis. In the XRD pattern of the AB sample produced by the Printsharp machine, the highest peak at 74° (corresponding to the [220] lattice plane) indicates that the grains are oriented with the <110> direction parallel to the build direction. This implies a melt pool geometry that causes the thermal gradient direction to be at a 45° angle to the build direction.

The exclusive identification of the copper phase can be attributed to several factors. Firstly, nickel, the alloy's second-most abundant element (2.4 wt%), exhibits complete miscibility with copper, remaining in solid solution with it. Secondly, the remaining nickel content, which did not participate in the solid solution, falls below the detection limit (2%) of the XRD instrument.

In order to assess the elemental distribution within the sample, EDS analysis on the Z plane is presented in Figure 79.

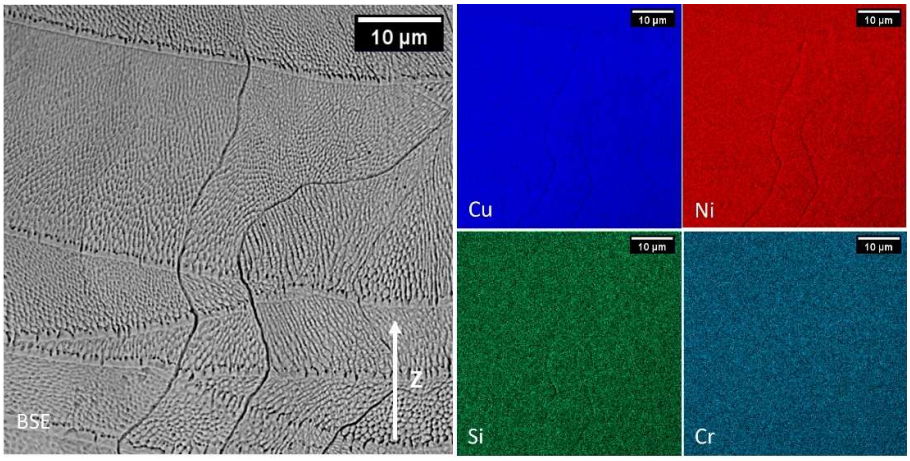

Figure 79. EDS SEM map of a CuNi2SiCr sample in the AB condition produced by Printgreen machine.

The EDS SEM map illustrates a uniform distribution of Cu, Ni, Si, and Cr throughout the entire sample, with no noticeable variation in their concentrations along the melt pool boundaries. This consistent dispersion confirms the solid solution of Cu, Ni, Si, and Cr.

7.3.4 Hardness

A preliminary study of the mechanical properties of these samples were conducted measuring the hardness in the as-built condition. The Vickers microhardness test resulted in a value of 100 ± 4 HV.

7.3.5 Discussion

Based on the obtained results, it is possible to state that the optimal relative density was achieved at a VED of approximately at 275 J/mm³, resulting in a fully dense sample at 99.7%. Increasing the VED to higher value led to a decrease of the relative density reaching values below 99%. The range of VED required to achieve fully dense samples seems to be nearly within the optimal range identified for the medium-power red laser machine but slightly lower. This variance can be attributed to the greater material absorption at the green laser compared to the red laser, owing to the distinct laser wavelengths. The high relative density corresponds to a minimal occurrence of defects, consisting of gas porosities.

The microstructure of the samples is composed by columnar grains aligned parallel to the build direction with a slight zig-zag pattern, a characteristic also observed in the red laser samples, and it is common in additive manufacturing parts. These grains were accompanied by the presence of melt pools, consistent with observations made in the medium and low power samples. Notably, the size of the melt pools in the current samples was comparable to those observed in the medium-power red laser samples, while the grain width was almost twice that of the low-power ones. Moreover, the length of the grains extended to several hundreds of microns, mirroring observations from the red laser samples.

Phase and composition analysis further supported the observations made in the red laser samples, confirming the only presence of a FCC phase within the specimens. Furthermore, Ni, Si, and Cr were found to be in solid solution with the Cu matrix.

Finally, the hardness value of 100 ± 4 HV was observed, slightly surpassing that of the low-power samples (93 ± 11 HV) and falling slightly behind the hardness observed in the medium-power samples (104 ± 3 HV), though it remains within a comparable range.

7.4 Heat treatment optimization

The optimization of the heat treatment was conducted using samples from batch 2, which were produced using the Printsharp machine (medium-power red laser samples).

7.4.1 Hardness

The hardness comparison of the heat-treated samples is shown in Figure 80 as a function of time of the aging.

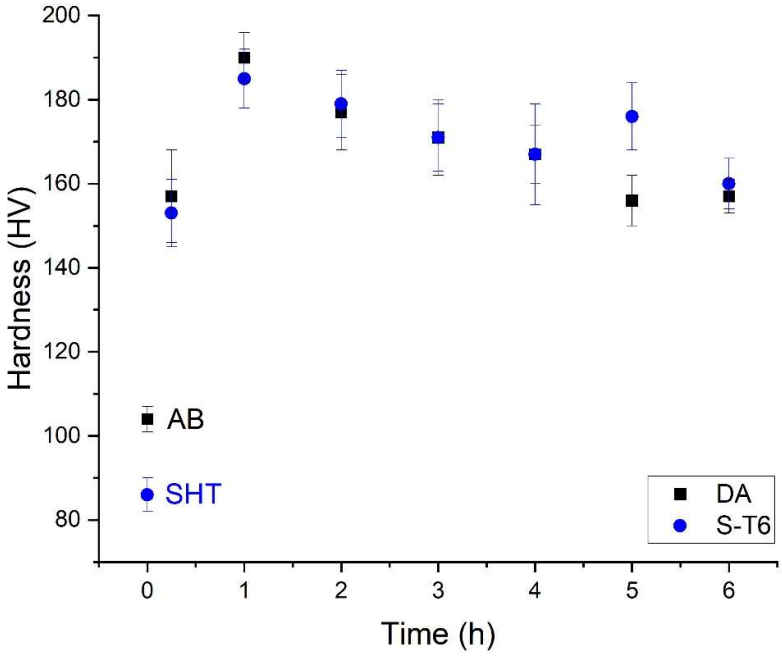

Figure 80. Hardness trends during DA and S-T6 aging at 540 °C.

The hardness of the AB sample was measured at 104 ± 3 HV, consistent with findings by Ventura et al. [82]. Following the direct aging heat treatment at 540°C, the hardness increased, peaking at 190 ± 6 HV after 1 hour (DA1) before gradually declining over 6 hours. In comparison, the SHT sample exhibited the lowest hardness among all samples tested, registering at 86 ± 4 HV. However, its hardness increased during aging treatment, mirroring the behavior observed in the DA samples. After 1 hour of aging treatment, the SHT sample achieved its highest

hardness value of 185 ± 7 HV (S-T6-1), comparable to that of the S-T6 samples, and then gradually declined over 6 hours.

These results were used to decide which samples to analyze more thoroughly. For the XRD, DSC, microstructural, and compositional analyses, the starting point samples, AB and SHT, were selected, along with the samples exhibiting the highest hardness values, DA1 and S-T6-1 respectively. Additionally, the samples subjected to the longest heat treatment durations, DA6 and S-T6-6, were included. For the AB sample, in this section, only XRD and DSC analyses are reported, as the other characterizations have already been presented in sections 6.2.2 and 6.2.3.

7.4.2 Phases evolution

The XRD patterns of the previously selected conditions are shown in Figure 81.

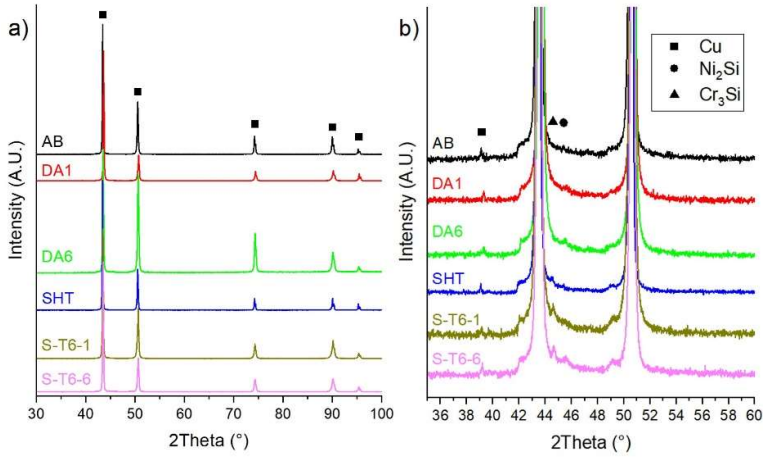

Figure 81. XRD patterns along Z direction of AB, DA1, DA6, SHT, S-T6-1 and S-T6-6 samples in the 2theta range of a) 30-110° and of b) 35-60°.

Starting from Figure 81a, it is possible to gain an overview of the entire XRD patterns of the studied conditions. As observed in previous sections of this thesis concerning this alloy processing, the XRD pattern exhibited solely the FCC phase, with its primary peak at 43° ([111] lattice plane) along the Z section. Zooming into a 2θ range between 35° and 60°, as showed in Figure 81b, reveals some new small peaks emerging across different conditions.

Examining the aging evolution in both DA and S-T6 conditions, a minor peak appeared around 45.5°, and it increased with longer durations of direct aging. This peak can be attributed to the Ni_2Si phase, which exhibits its peak with maximum intensity at 45.5°, but it cannot be completely confirmed because of the only presence of one small peak of its pattern. However, it is widely recognized that the precipitation of this phase occurs during the aging of this alloy [150,151].

Focusing on the evolution of the S-T6 heat treatment, it is evident the appearance of a small new peak at 44.4° starting from the SHT condition compared to the AB, DA1 and DA6 ones. This peak could be identified with the main peak of the Cr_3Si phase, but it cannot be completely confirmed due to the only presence of one small peak of its pattern. Nevertheless, this peak suggests the presence of Cr precipitates after the solutioning heat treatment followed by quenching, which are not present in the AB condition. A similar behavior was observed by Salvan et al. and [152] while working with the CuCrZr alloy processed by L-PBF. They observed that in the as built condition, the Cr remained in solid solution within the copper matrix. However, after the solutioning and quenching, part of the Cr precipitated in the form of micro-precipitates, while the remaining stayed in solid solution. During the subsequent aging treatment, the remaining Cr precipitated in the form of nano-precipitates. The increase in intensity of the Cr_3Si peak as the aging time increases seems to confirm this behavior.

The DSC patterns of the previously selected conditions are shown in Figure 82.

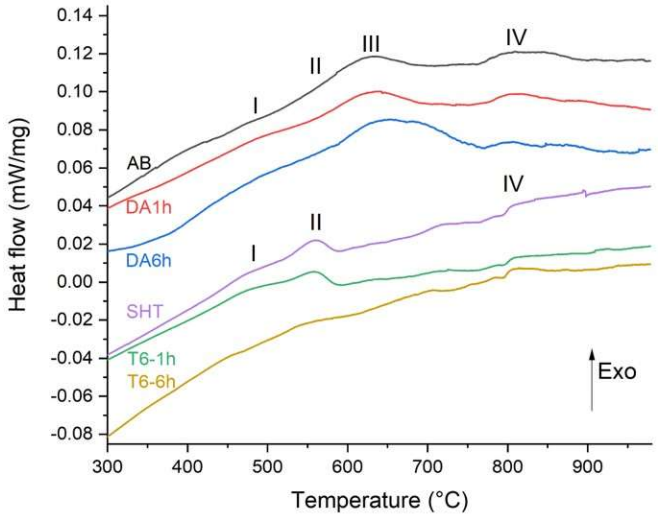

Figure 82. DSC analysis of AB, DA1, DA6, SHT, S-T6-1 and S-T6-6 samples.

The DSC comparison shows the presence of four exothermic peaks at 450°C (I), 550°C (II), 630°C (III) and 800°C (IV) in the AB, DA1 and DA6 conditions, and only three peaks (I, II, IV) in the SHT, S-T6-1 and S-T6-6 ones.

The first peak (I), observed in both heat treatments, at 450°C, is attributed to two phenomena: recrystallization and Cr clusters precipitation. The recrystallization temperature for pure copper is typically in the range of 379–433°C [153], while for copper alloys such as Cu-Zr and Cu-Cr-Zr-Mg, it occurs around 450°C [154]. Considering this data, it is reasonable to infer that this temperature, which also corresponds to half the melting temperature in Kelvin (1353 K) of this alloy, represents its recrystallization temperature, thus identifying this peak as the recrystallization peak. Additionally, this temperature aligns with the precipitation of Cr clusters, as reported by Bourezg et al. [155] in their study on CuCrZr alloy. Moreover, it corresponds to the temperature specified in the heat treatment patent for the CuNi2SiCr alloy, facilitating the precipitation of Cr [142].

The second peak (II), observed in both heat treatments, at 550 °C, is attributed to the Ni_2Si precipitation. This peak is clearer visible in the S-T6 heat treatment evolution than the DA one due to the overlapping with peak III in the latter. Furthermore, this peak gradually reduces its intensity as the aging time increases in both conditions. This reduction can be attributed to the gradual precipitation of Ni_2Si precipitates during the aging heat treatment, as previously observed in the XRD pattern with the appearance of the Ni_2Si phase peak in the aged samples.

The third peak (III), observed exclusively in the DA heat treatments, at 630 °C, is attributed to the Cr_3Si precipitation. The absence of this peak in the S-T6 heat treatments is explained by the Cr_3Si precipitation during the solutioning heat treatment, as confirmed by the XRD analysis. The presence of Cr enriched phases after solutioning was also observed by Meng et al. [150].

Finally, the fourth peak (IV), observed in both heat treatments, starting from 800 up to 980 °C, is attributed to precipitation dissolution. This temperature range for the copper alloys solutioning heat treatment is well known and reported in many books such as ASM Speciality Book for copper and copper alloys [49].

On the base of previously reported results, we can suppose that these heat treatments led the precipitation of the Ni_2Si phase, which is the main reason for the strengthening of this alloy. The detection of the Ni_2Si phase in the XRD pattern (Figure 81b) after 6 hours of aging heat treatment, and the complete reduction of

the exothermal peak at 550°C (Figure 82) attributed to the precipitation of this phase in the DSC pattern, can be assumed as confirmation of its complete precipitation. The complete precipitation of Ni_2Si after 6 hours of aging heat treatment led to a reduction in hardness (Figure 80) compared to the peak-aged conditions (after 1 hour of aging) due to the reduction of the solid solution and the growth of the precipitates [150].

7.4.3 Microstructure and compositional analysis

The following characterizations were performed employing tools such as the optical microscope (OM) and the scanning electron microscope (SEM). For the analysis, samples were etched using the ASTM E407 Standard (25% NH4OH + 25% H2O + 50% H2O2) through the process of electro-etching.

7.4.3.1 Direct aged 1 hour (DA1) sample

In Figure 83 is reported the microstructure obtained with the optical microscope of the DA1 sample.

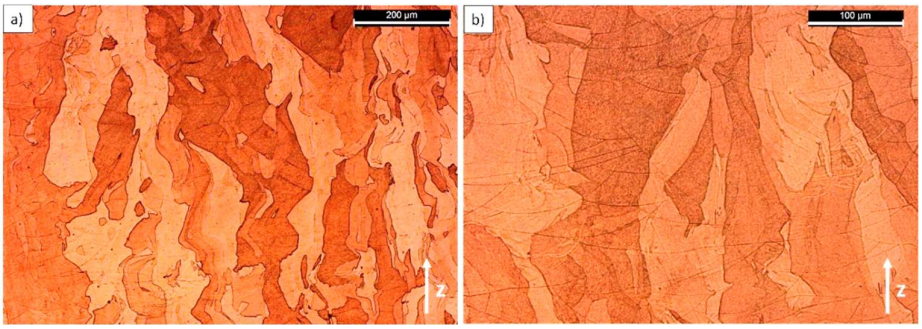

Figure 83. OM images of the DA1 sample microstructure at a) 100X and b) 200X.

This condition exhibits columnar grains aligned parallel to the building direction (z), like those found in the AB condition. The grains appear slightly smaller and shorter compared to the AB ones, reaching sizes as large as 80 µm, and the melt pools, although still visible, began to disappear.

An overview of the microstructure at higher magnification is illustrated in Figure 84.

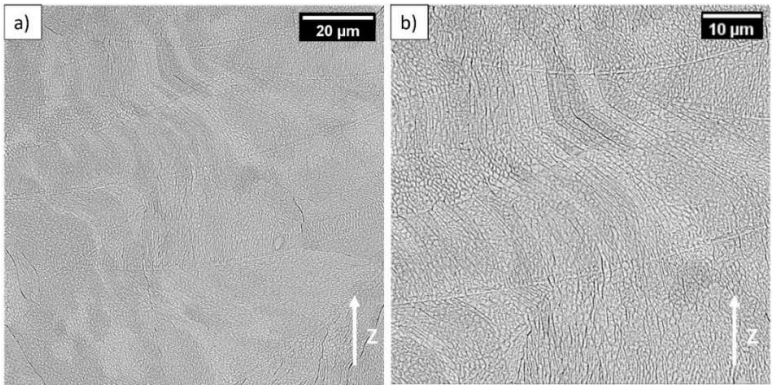

Figure 84. BSE SEM images of the DA1 sample after etching at different magnifications a) 2500X and b) 4000X.

The SEM BSE images reveal the presence of melt pools and grain boundaries traversing multiple melt pools along the construction axis (z), consistent with observations in AB samples. The most notable distinction between these two conditions is the disappearance of cellular dendrites, which are prominently visible in the AB condition but less reliably discernible in the DA1 one.

In order to assess the elemental distribution within the sample, EDS analysis on the Z plane is presented in Figure 85.

The EDS SEM map illustrates a uniform dispersion of Cu, Ni, Si, and Cr throughout the entire sample, with no apparent variation in their concentrations along the grain boundaries or the boundaries of the melt pool. No observable precipitates are present in this condition.

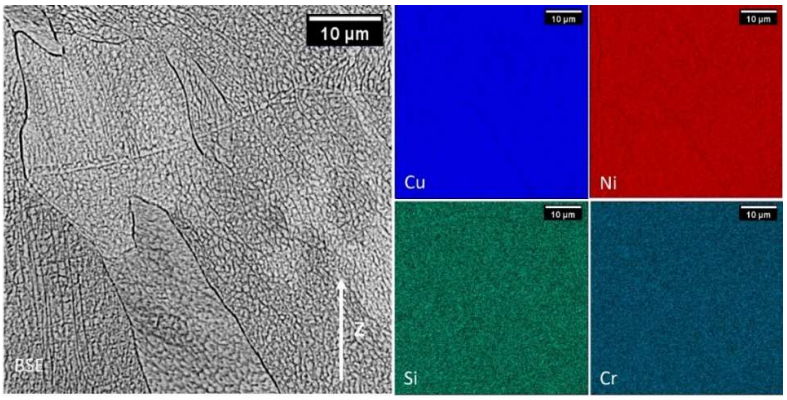

Figure 85. EDS SEM map of a CuNi2SiCr sample in the DA1 condition produced by Printsharp machine.

7.4.3.2 Direct aged 6 hours (DA6) sample

In Figure 86 is reported the microstructure obtained with the optical microscope of the DA6 sample.

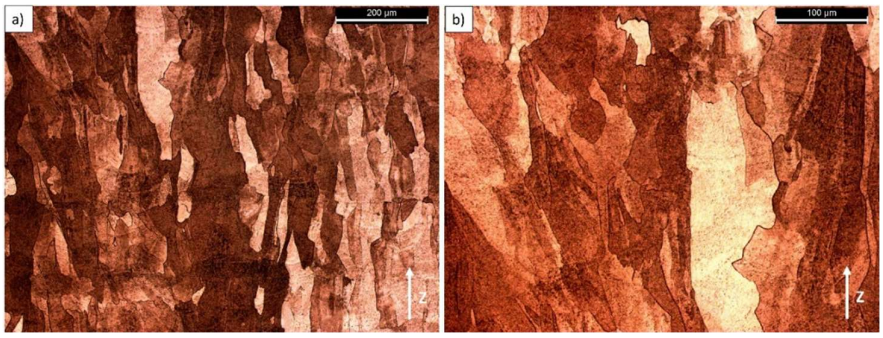

Figure 86. OM images of the DA6 sample sample at a) 100X and b) 200X.

This condition exhibits columnar grains aligned parallel to the building direction (z), like those found in the AB and DA1 condition. The grains are visibly smaller and shorter compared to the AB and the DA1 ones, reaching sizes as large as 50 µm, and the melt pools, are completely disappeared.

An overview of the microstructure at higher magnification is illustrated in Figure 87.

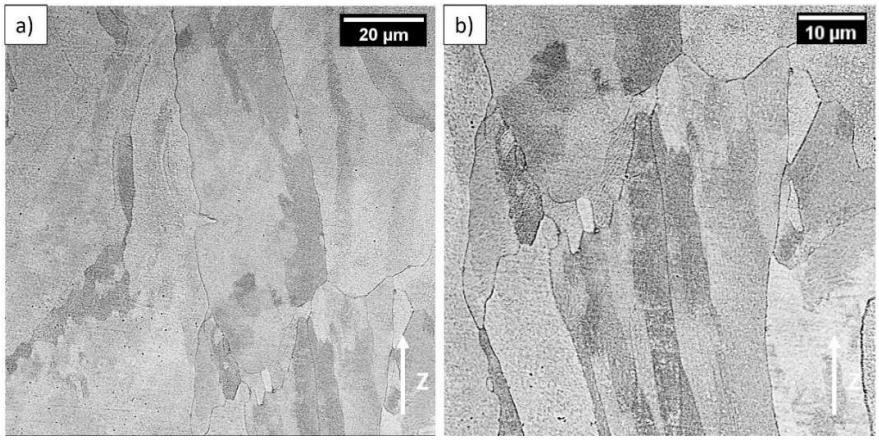

Figure 87. BSE SEM images of the DA6 sample after etching at different magnifications a) 2500X and b) 4000X.

The SEM BSE images show the absence of melt pools compared to previous conditions and the emergence of smaller grains, attributed to the formation of new subgrains within the existing columnar grains aligned with the build direction.

To assess the elemental distribution within the sample, EDS analysis on the Z plane is presented in Figure 88.

The EDS SEM map demonstrates a consistent dispersion of Cu and Cr throughout the entire sample, without notable variation in their concentrations along the grain boundaries. In contrast, Ni was present throughout the entire sample, but with a higher concentration, along with Si, at the grain boundaries. Precipitates composed of these two elements were found, identifiable as the Ni_2Si phase. This observation is consistent with the evolution of the XRD and DSC patterns presented earlier, thereby confirming the previously posited hypothesis.

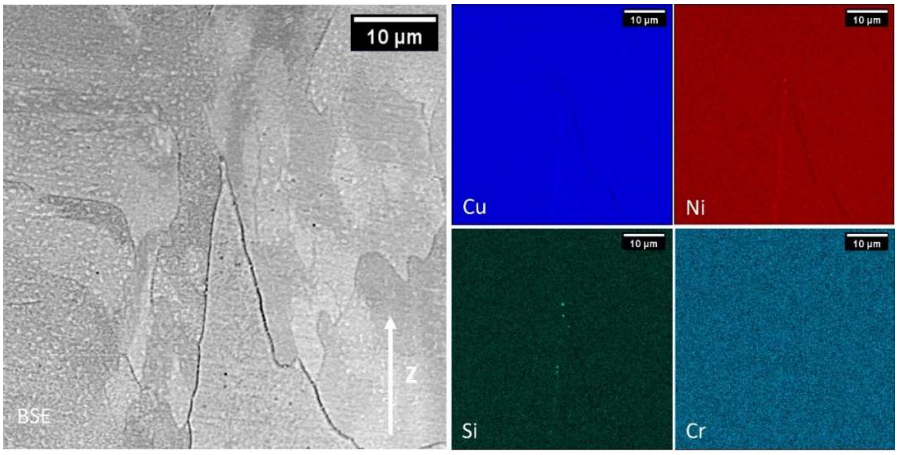

Figure 88. EDS SEM map of a CuNi2SiCr sample in the DA6 condition produced by Printsharp machine.

7.4.3.3 Short solutioned (SHT) sample

In Figure 89 is reported the microstructure obtained with the optical microscope of the SHT sample.

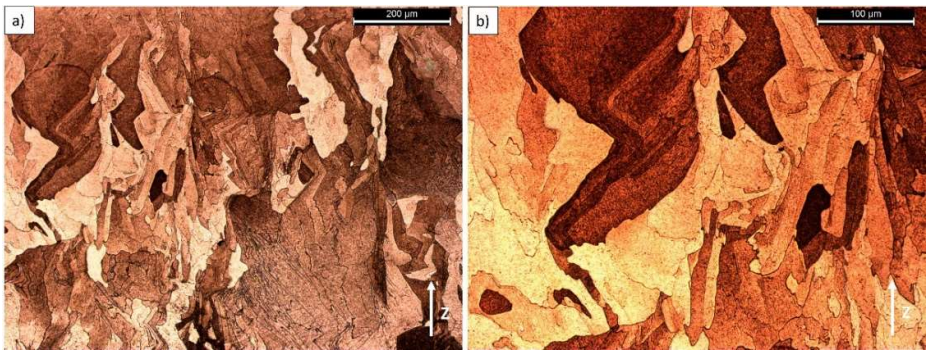

Figure 89. OM images of the SHT sample at a) 100X and b) 200X.

This condition exhibits columnar grains aligned parallel to the building direction (z), but with smaller size than the AB condition, reaching sizes as large as 70 µm. It is worth to also note the presence of some small equiaxial grains due to the solution heat treatment of 15 minutes and the absence of melt pools.

An overview of the microstructure at higher magnification is illustrated in Figure 90.

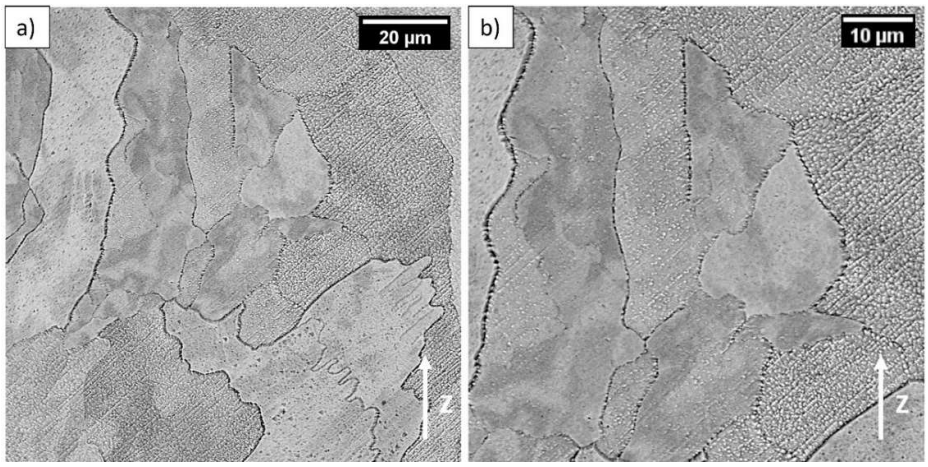

Figure 90. BSE SEM images of the SHT sample after etching at different magnifications a) 2500X and b) 4000X.

The SEM BSE images show columnar grains composed of small subgrains and the presence of some equiaxial grains, consistent with observations from the OM images. Another significant distinction between the AB and SHT conditions is the

absence of cellular dendrites, which are prominently visible in the AB condition but are indiscernible in the SHT one.

To assess the elemental distribution within the sample, EDS analysis on the Z plane is presented in Figure 91.

The EDS SEM map illustrates a uniform dispersion of Cu and Ni throughout the entire sample, with no significant variation in their concentrations along the grain boundaries. Conversely, Si and Cr were present throughout the entire sample, but exhibited a higher concentration at the grain boundaries. Precipitates composed of these two elements could be identified as the Cr_3Si phase. This observation aligns with the evolution of the XRD and DSC patterns presented earlier, confirming the previously proposed hypothesis.

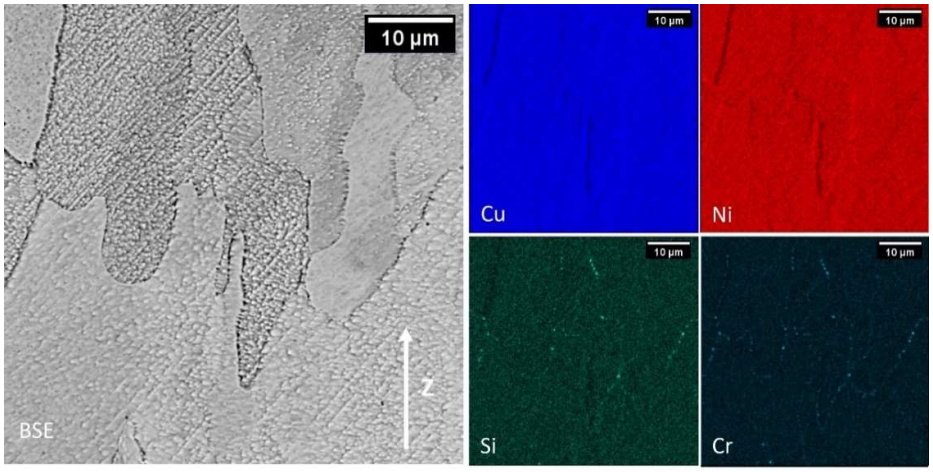

Figure 91. EDS SEM map of a CuNi2SiCr sample in the SHT condition produced by Printsharp machine.

7.4.3.4 Short T6 1 hour (S-T6-1) sample

In Figure 92 is reported the microstructure obtained with the optical microscope of the S-T6-1 sample.

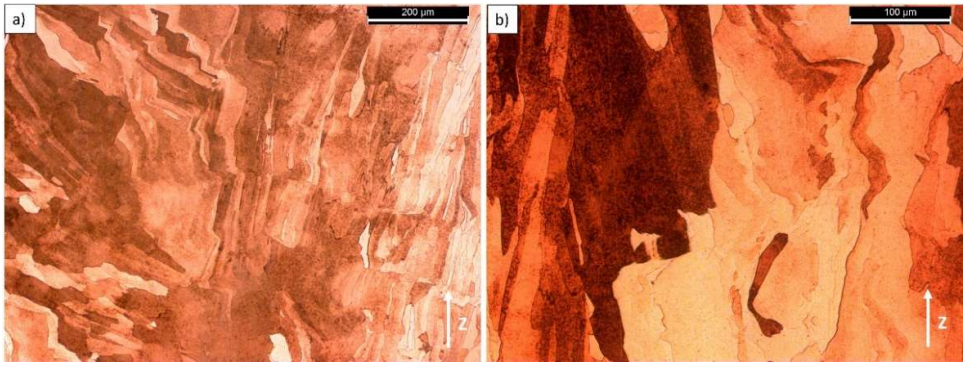

Figure 92. OM images of the S-T6-1 sample at a) 100X and b) 200X.

This condition exhibits columnar grains aligned parallel to the building direction (z) and some equiaxial grains, but with smaller size than the SHT condition, reaching sizes as large as 45 µm. This behavior aligns with what was observed about the grain reduction in the DA1 sample respect to the AB one. The aging treatment performs a grain refinement leading to smaller grains.

An overview of the microstructure at higher magnification is illustrated in Figure 93.

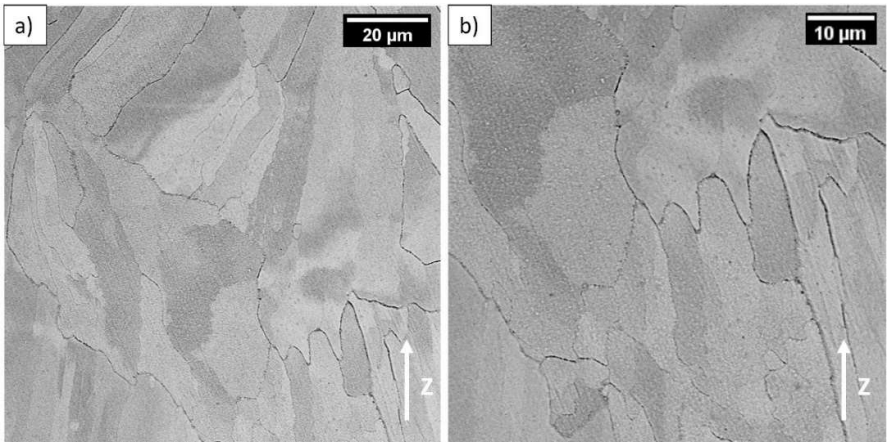

Figure 93. BSE SEM images of the S-T6-1 sample after etching at different magnifications a) 2500X and b) 4000X.

The SEM BSE images show columnar grains composed of small subgrains and the presence of some equiaxial grains, consistent with observations from the OM images. The grain size is visible smaller than the SHT condition.

To assess the elemental distribution within the sample, EDS analysis on the Z plane is presented in Figure 94.

The EDS SEM map demonstrates a uniform dispersion of Cu and Ni throughout the entire sample, with no significant variation in their concentrations along the grain boundaries. Conversely, Si and Cr were present throughout the entire sample but exhibited a higher concentration at the grain boundaries, mirroring the findings in the SHT condition. Precipitates composed of these two elements could be identified as the Cr_3Si phase, consistent with observations in the SHT condition.

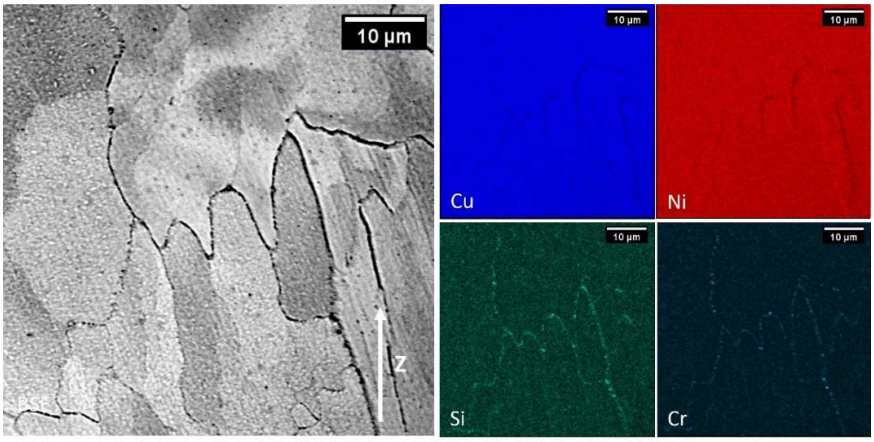

Figure 94. EDS SEM map of a CuNi2SiCr sample in the S-T6-1 condition produced by Printsharp machine.

7.4.3.5 Short T6 6 hours (S-T6-6) sample

In Figure 95 is reported the microstructure obtained with the optical microscope of the S-T6-6 sample.

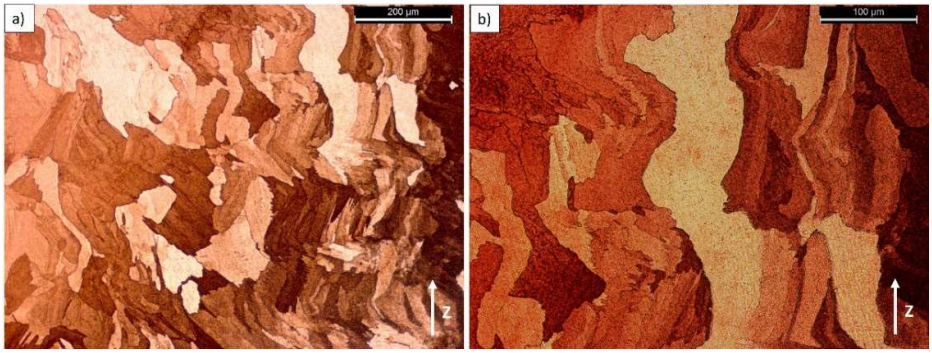

Figure 95. OM images of the S-T6-6 sample at a) 100X and b) 200X.

This condition exhibits columnar grains aligned parallel to the building direction (z) and some equiaxial grains, but with smaller size than the SHT condition and comparable with the S-T6-1 one, reaching sizes as large as 30 µm.

An overview of the microstructure at higher magnification is illustrated in Figure 96.

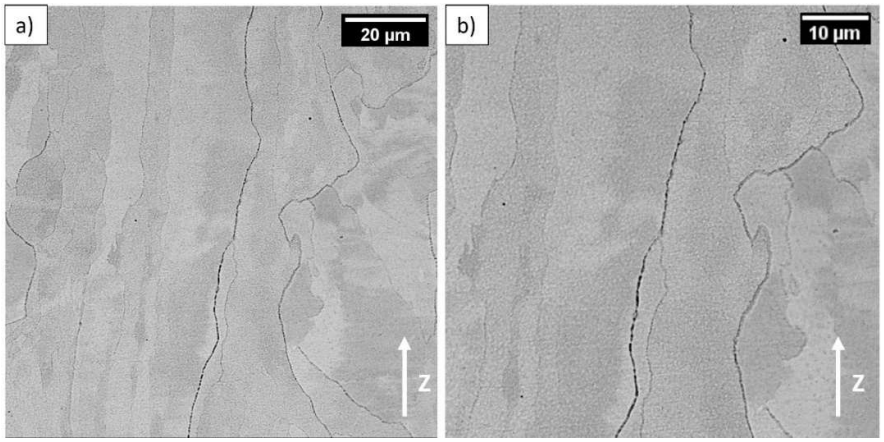

Figure 96. BSE SEM images of the S-T6-6 sample after etching at different magnifications a) 2500X and b) 4000X.

The SEM BSE images show a very similar microstructure to the S-T6-1 condition. This microstructure presents columnar grains composed of small subgrains with the presence of some equiaxial grains, consistent with observations from the OM images. The grain size is visible smaller than the SHT condition and comparable with the S-T6-1 one.

To assess the elemental distribution within the sample, EDS analysis on the Z plane is presented in Figure 97.

The EDS SEM map reveals a uniform dispersion of Cu and Ni throughout the entire sample, with no significant variation in their concentrations along the grain boundaries. Conversely, Si and Cr were present throughout the entire sample but exhibited a higher concentration at the grain boundaries, consistent with observations in the SHT and S-T6-1 conditions. Precipitates composed of these two elements could be identified as the Cr3Si phase, aligning with observations in the previous two conditions. However, no precipitates of Ni and Si were found in this condition, which contrasts with the findings obtained in the DA6 condition and does not provide confirmation of the peak at 45.5° in the S-T6-6 XRD pattern, which is indicative of the Ni_2Si phase.

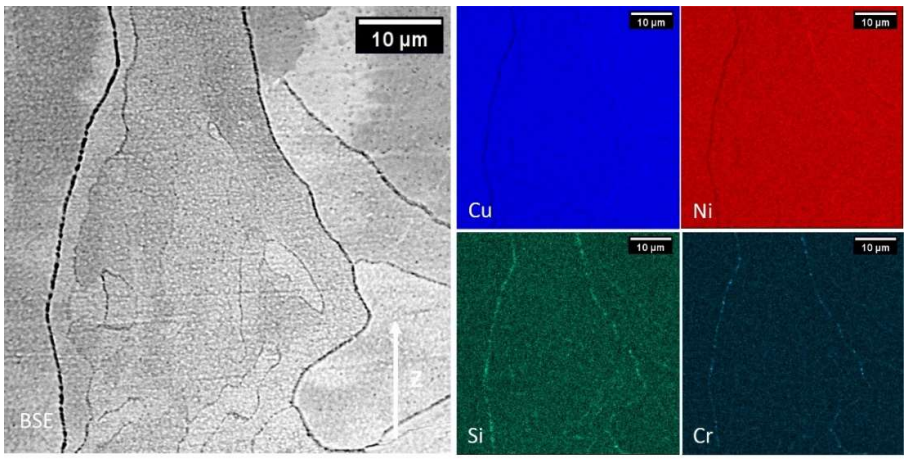

Figure 97. EDS SEM map of a CuNi2SiCr sample in the S-T6-6 condition produced by Printsharp machine.

7.4.4 EBSD comparison

To better understand the evolution of the grains size and the grain orientation throughout the different steps of these two heat treatments, EBSD analysis were performed.

In Figure 98 is proposed a EBSD comparison among the AB, DA1, DA6, S-T6-1 and S-T6-6 conditions, with the representation of the different grains in

random colors in the left column (a-c-e-g-i) and of the inverse pole figure on Z axis (IPF-Z) in the right column (b-d-f-h-j).

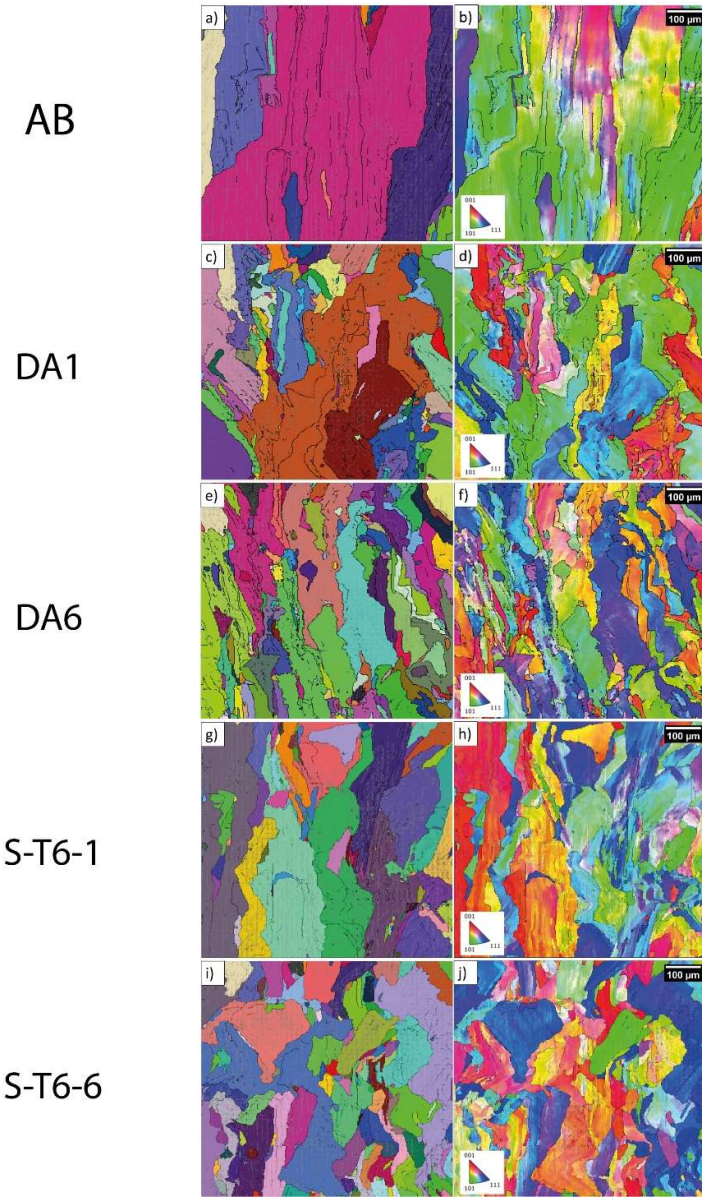

Figure 98. EBSD analysis of Printsharp CuNi2SiCr samples in AB (a, b), DA1 (c, d) DA6 (e, f), S-T6-1 (g, h) and S-T6-6 (i, j) conditions. Figures a), c), e), g) and i) represent grains in random color and figures b), d), f), h) and j) represent the inverse pole figure on Z-axis (IPF-Z).

From this image, it is evident that increasing the duration of the aging heat treatment resulted in a reduction in grain size. The numerical results of the average fitted ellipse major diameter (length of the grains) are summarized in Figure 99.

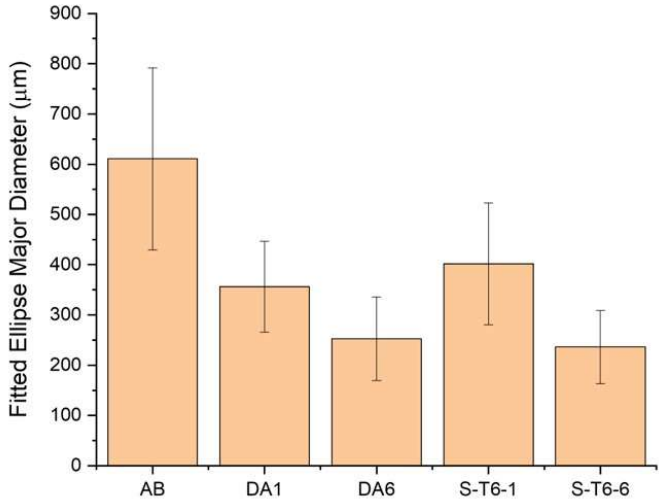

Figure 99. Average of the fitted ellipse major diameter (length of the grains) for each heat treatment condition.

The AB condition exhibited a mean grain length of 610 ± 181 μm, which gradually decreased to 252 ± 83 μm in the DA6 one. A similar trend was observed during the aging process of the S-T6 heat treatment, with grains reaching comparable lengths. The high standard deviation is due to the presence of grains with significant differences in size.

The reduction in grain size is attributed to the heat treatment conducted at 540°C. This temperature exceeds the recrystallization temperature, which is approximately 450°C (723 K), leading to a formation of new set of strain-free and equiaxial grains, as observed in the evolution of those heat treatments.

Furthermore, EBSD analysis enables the observation of grain orientation through IPF-Z images. It is evident that in the AB condition, there is a pronounced texture of grain orientation along the (101) direction. However, this specific orientation is absent in the other conditions.

7.4.5 Mechanical and electrical properties

Tensile and electrical tests were carried out on the samples from batches 3 and 4 (Figure 38), which were produced by the Printsharp machine.

The mechanical and electrical properties are summarized in Figure 100.

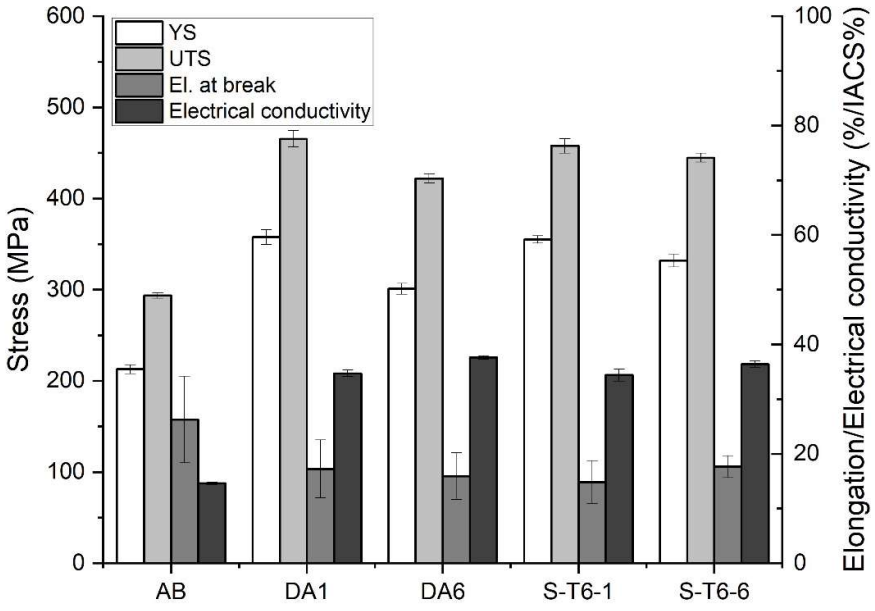

Figure 100. Mechanical and electrical properties of the CuNi2SiCr samples produced by Printsharp machine in AB, DA1, DA6, S-T6-1 and S-T6-6 conditions.

The AB condition presented the lowest Yield Strength (YS), Ultimate Tensile Strength (UTS), and electrical conductivity of all the conditions, with values of 213 ± 5 MPa, 294 ± 3 MPa, and 14.6% IACS, respectively. It showed also the highest elongation at break with a value of 26%. This alloy is normally used in a heat-treated condition because it is a precipitation hardening alloy, so there are no references in the literature for the as-cast properties. These results can be compared with those obtained by Ventura et al. [86], and for the as-built condition they a very similar.

As expected, DA1 and S-T6-1 showed the highest YS and UTS values. DA1 exhibited YS and UTS values of 358 ± 8 MPa and 466 ± 9 MPa, respectively, while S-T6-1 exhibited YS and UTS values of 355 ± 4 MPa and 458 ± 8 MPa, respectively. Both conditions presented very similar elongation at break, around

16%, which is lower than that of the AB condition. Moreover, they exhibited an electrical conductivity of 34.5% IACS, which is more than double that of the AB condition and slightly higher than the results obtained by Ventura et al. [86] in the same condition. This increase in electrical conductivity is due to the precipitation of solute atoms, which interrupt the copper matrix reducing the electrical conductivity, from the matrix during the aging heat treatment. Moreover, the obtained mechanical properties of the heat-treated samples are not comparable to those obtained by Ventura et al. [86] due to the different geometries used for the tensile samples.

The DA6 and S-T6-6 conditions presented slightly lower mechanical properties compared to the DA1 and S-T6-1 conditions maintaining the same elongation at break, but with a slight increase in electrical conductivity, reaching values around 37% IACS.

No significant differences were observed between the direct aging and short T6 heat treatments. After 1 hour of aging, they presented comparable mechanical and electrical properties. However, after 6 hours, direct aging exhibited slightly lower mechanical properties and slightly higher electrical conductivity.

7.4.6 Discussion

Based on the obtained results, starting from hardness values of 104 ± 3 HV for the AB condition and 86 ± 4 HV for the SHT one, the heat treatments that yielded the best hardness values were DA1 and S-T6-1, with 190 ± 6 HV and 185 ± 7 HV, respectively.

The XRD and DSC analyses revealed the precipitation of Ni_2Si from the matrix during the aging treatment at 540°C, observed in both DA and S-T6 heat treatments. Additionally, in the DA6 sample, precipitates of Ni and Si were observed through EDS analysis, which was not observed in the S-T6-6 sample. These precipitates are responsible for the increase in hardness compared to the AB and the SHT conditions [150].

During the SHT heat treatment at 930°C, the precipitation of Cr_3Si was observed. According to the DSC analysis, this phase began to precipitate around 630°C, and its presence in the samples was confirmed by both XRD and EDS analyses. These precipitates were also found in the S-T6-1 and S-T6-6 conditions after the aging heat treatment.

The aging heat treatment led to a reduction in grain size. Increasing the duration of the aging heat treatment resulted in a further reduction in grain size with the appearance of equiaxial grains. The width of the grains changed from 170 μm for the AB condition to 50 μm for the DA6 one, and from 70 μm for the SHT condition to 30 μm for the S-T6-6. This behavior was confirmed also by the EBSD analysis which measured the mean length of the grains. The length of the grains changed from 610 ± 181 μm for the AB condition to 252 ± 83 μm for the DA6 one. The grain refinement is attributed to the heat treatment performed at 540°C, which exceeds the recrystallization temperature of approximately 450°C (723 K). This process leads to the formation of a new set of strain-free and equiaxial grains, which fracture the columnar grains into smaller grains. Consequently, the replacement of the 'old' columnar grains, laden with residual stresses, by the 'new' strain-free and equiaxial grains results in a reduction in internal stresses, ultimately contributing to a decrease in hardness compared to the peak aged conditions.

Furthermore, the EBSD analysis highlighted the high texturing of the AB condition along the (101) direction, a behavior that was absent in the other conditions.

The tensile tests confirmed the observations from the hardness tests. The AB condition showed the lowest mechanical and electrical properties, with YS, UTS, and electrical conductivity values of 213 ± 5 MPa, 294 ± 3 MPa, and 14.6% IACS, respectively, but had the highest elongation at break at 26%. The highest mechanical properties were achieved by the DA1 and S-T6-1 conditions. DA1 exhibited YS and UTS values of 358 ± 8 MPa and 466 ± 9 MPa, respectively, while S-T6-1 exhibited YS and UTS values of 355 ± 4 MPa and 458 ± 8 MPa, respectively. In these conditions, the electrical conductivity increased to 34.5% IACS. Increasing the aging time led to a slight increase in electrical conductivity and a slight decrease in mechanical properties. No significant differences were observed between direct aging and short T6 heat treatments. After 1 hour of aging, they exhibited comparable mechanical and electrical properties. However, after 6 hours, direct aging showed slightly lower mechanical properties and slightly higher electrical conductivity. All these results align well with those obtained by Ventura et al. [86], except for the YS and UTS of the heat-treated samples, which cannot be compared due to the different shapes of the tested tensile specimens.

7.5 Densification with HIP

The HIP heat treatment was performed on samples from both batches 1 and 2, produced using the Concept machine (low-power red laser samples).

7.5.1 Relative density

The relative density of the HIPped samples was determined using the gas-pycnometer employed in the other sections. These results were plotted alongside the average relative density of the initial AB samples as a function of the HIPping time. The graph is visible in Figure 101.

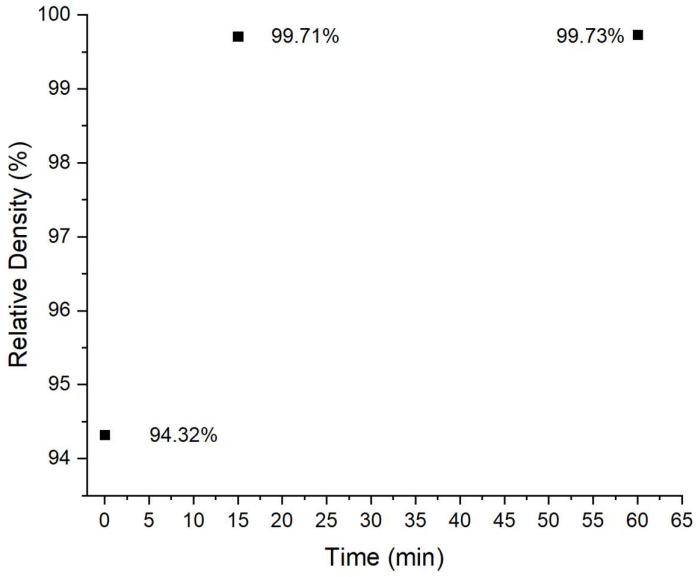

Figure 101. Relative density vs time of HIP process.

This graph shows the significant increase in relative density of the samples following the HIPping treatment, reaching an impressive value of 99.71% after 15 minutes and then stabilizing at 99.73% after 60 minutes.

To validate the relative densities measured by pycnometer, image analyses were conducted, and the results are reported in Figure 102.

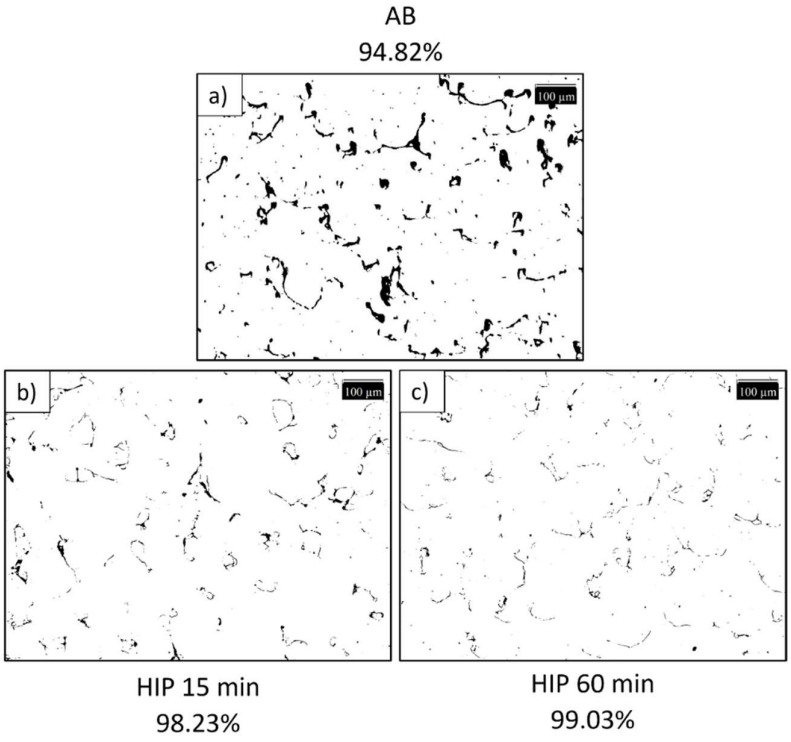

Figure 102. OM relative density comparison between a) AB, b) HIP 15 minutes and c) 60 minutes conditions.

In Figure 102a, it is evident that the initial relative density of approximately 94% is confirmed. However, upon comparing the results of the image analysis of the HIPped samples, which yielded 98.23% for the HIP 15-minute samples and 99.03% for the HIP 60-minute samples, with those obtained by the pycnometer, it becomes apparent that the calculated relative density by the pycnometer was slightly overestimated. This discrepancy could be attributed to open porosities within the samples that the pycnometer ignores but are evaluated through image analysis. The HIPping process can only affect closed porosities, meaning that during this process, all open porosities remain unaffected by densification. Figure 102b and c also demonstrate that the HIPping performed on these samples did not close the porosities, although it did reduce their size. It is plausible to hypothesize that by conducting HIPping for a longer duration, a significant portion of the porosities could be eliminated.

7.5.2 Microstructure and compositional analysis

The study of the microstructure involved the use of an optical microscope (OM), a scanning electron microscope (SEM), and the 40th Etchant in ASTM E407 Standard (5 grams of $FeCl_3$ + 16 mL HCl + 60 ml C_2H_5OH) to reveal grains.

The initial investigation was conducted at low magnification using the optical microscope. In Figure 103, a comparison between the microstructure of the sample HIPped for 15 minutes (Figure 103a) and for 60 minutes (Figure 103b) is presented.

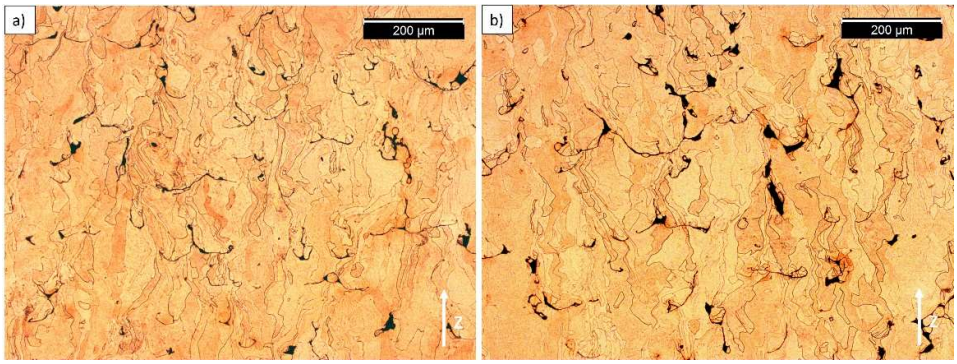

Figure 103. Microstructure after HIP process of the Concept samples a) for 15 minutes and b) 60 minutes (OM 100X).

The microstructure of these samples is remarkably similar. The heat treatment removed the characteristic melt pools of the AB condition and resulted in a large portion of columnar grains with sizes up to 80 µm. This value agrees with the grain size of a similar CuNiSi alloy processed by casting and subjected to the T6 heat treatment, but in that case, it exhibited equiaxed grains [133]. However, the grains during the HIP heat treatment began to recrystallize, and it is possible to observe some small equiaxed grains within the columnar grains.

The second investigation was effectuated at higher magnification using the same SEM employed for the other characterizations. The comparison between the two condition is shown in Figure 104.

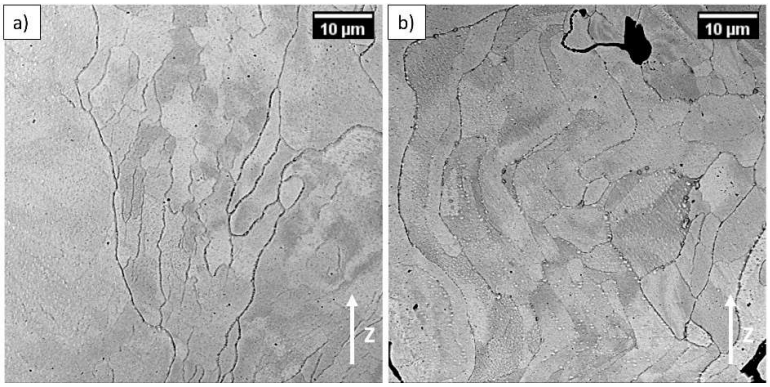

Figure 104. BSE images of the Concept samples after a) 15 minutes and b) 60 minutes of HIP heat treatment at 4000X.

Figure 104a, representing a magnification of the HIP 15 minutes sample, clearly shows a columnar grain that has begun to recrystallize, containing numerous subgrains within itself. Conversely, within the HIP 60 minutes sample, it is evident how the subgrains have grown due to the longer heat treatment at the solubilization temperature. Moreover, it is possible to note the presence of precipitates at the grain boundaries.

To evaluate the element distribution in the samples and to identify the precipitates at the grain boundaries, EDS analyses on the Z plane are reported in Figure 105 and Figure 106.

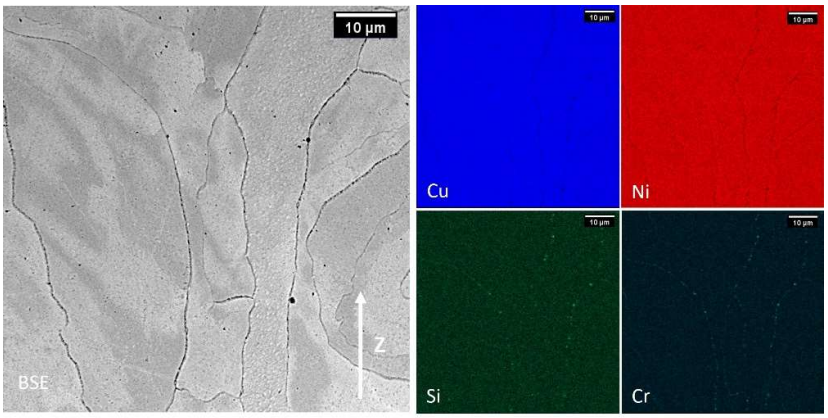

Figure 105. EDS SEM map of a CuNi2SiCr sample produced by Concept machine after 15 minutes of HIP.

The EDS SEM map of the HIP 15 minutes sample (Figure 105) reveals a uniform distribution of Cu and Ni throughout the sample with some variation near the grain boundaries. In contrast, Si and Cr are concentrated at the grain boundaries in small precipitates. This observation aligns with findings from the SHT, S-T6-1, and S-T6-6 heat treatments, confirming the precipitation of chromium and silicon that occurs during the solubilization heat treatment.

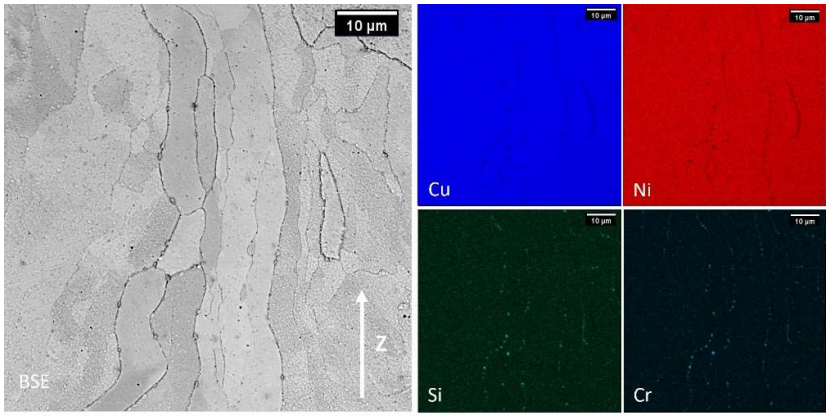

Figure 106. EDS SEM map of a CuNi2SiCr sample produced by Concept machine after 60 minutes of HIP.

The EDS SEM map of the HIP 60 minutes sample (Figure 106) confirms once again confirms what was previously observed, emphasizing larger precipitates of Si and Cr compared to the HIP 15 minutes sample. This is attributed to the longer heat treatment at the solubilization temperature, as already observed with the growth of the grains.

7.5.3 Hardness

A preliminary study of the mechanical properties of these samples were conducted measuring the hardness of the HIPped samples using a Vickers microhardness machine. In Figure 107 is reported the comparison between the hardness value of the SHT, HIP 15 minutes and HIP 60 minutes. The HIP 15 minutes sample exhibited a hardness value of 68 ± 8, which is lower than the AB hardness value, whereas the HIP 60 minutes sample showed a hardness value of 83 ± 10, which is comparable to it.

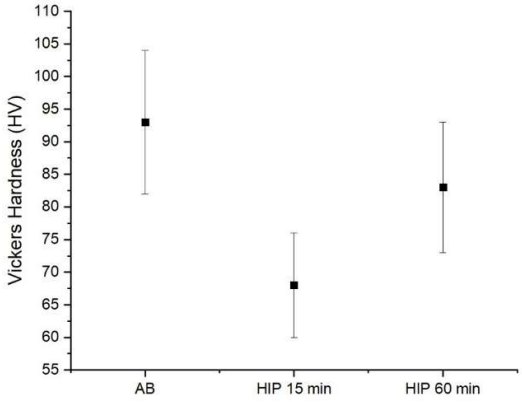

Figure 107. Hardness comparison between AB, HIP 15 minutes and HIP 60 minutes conditions.

7.5.4 Discussion

Based on the results obtained, it is possible to conclude that the HIPping process effectively reduced the porosities and significantly increased the relative density of the samples, reaching a value close to 99% from an initial 94%. However, the presence of defects such as cracks and unmelted particles still persists within the samples, indicating the necessity to optimize the duration of the HIP process. Nevertheless, these findings remain very promising. Conducting the HIPping process for 15 minutes alone is insufficient to achieve full density in the part, while simultaneously utilizing it for solutioning.

The microstructure of the samples revealed the absence of the characteristic melt pools of the AB condition and the presence of a large portion of columnar grains. However, these grains began to recrystallize, and it is possible to observe some small equiaxed grains within the columnar grains. Moreover, precipitates of Si and Cr were observed at the grain boundaries. Equiaxial grains and precipitates are larger in the HIP 60 minutes samples than the HIP 15 minutes one.

Finally, the hardness value of the HIP 15 minutes sample, at 68 ± 8, is lower than the AB hardness value, whereas the hardness value of the HIP 60 minutes sample, at 83 ± 10, is comparable to it.

Chapter 8

Conclusions and prospects

In this thesis, the processability, microstructure, and properties of pure copper and the CuNi2SiCr alloy produced by various powder bed fusion technologies were investigated. One of the primary objectives of this study was to optimize process parameters to achieve fully dense samples, while also comparing the resulting microstructure and properties across different technologies. Furthermore, optimizing the post-process heat treatment for CuNi2SiCr led to improved mechanical properties.

The main results obtained can be summarized as follows:

- Full dense samples of pure copper were successfully produced via EB-PBF. Optimal relative density, reaching around 99.3%, was achieved at a VED of approximately 80 J/mm^3, with few defects such as gas porosities. The microstructure revealed columnar grains aligned parallel to the growth direction, accompanied by the presence of melt pools. Grain length extended up to millimeters, notably exceeding that of the L-PBF process, owing to the distinctive thermal dynamics of EB-PBF which sustains elevated temperatures throughout, promoting extensive grain growth. This thermal history also influenced hardness, with resulting values of 54 ± 9 HV comparable to those of casted annealed pure copper.
- Porous samples of CuNi2SiCr were printed utilizing the low-power red laser machine. The highest relative density, approximately 97.52 ±

0.73%, was achieved with a VED of around 400 J/mm^3. The microstructure showed columnar grains aligned parallel to the growth direction, alongside the presence of melt pools. However, numerous defects, including lack of fusion, unfused particles, and cracks, were evident within the samples. These defects stem from insufficient laser power, hindering proper and complete fusion of the powder and resulting in the formation of porous samples. These porosities detrimentally affect both mechanical and electrical properties.

- Full dense samples of CuNi2SiCr were printed using the medium-power red laser machine. Optimal relative density, reaching approximately 99.7%, was achieved at a VED of around 316 J/mm^3, with few defects such as gas porosities and sporadic lack of fusion. The range of VED required for fully dense samples is narrower compared to the optimal range identified with the low-power red laser machine, attributed to variations in laser power. Below a certain threshold, the laser fails to fully melt the powder. The microstructure exhibited columnar grains aligned parallel to the growth direction, accompanied by the presence of melt pools, consistent with observations made in the low-power samples but with larger sizes due to the larger spot of the laser equipped on the medium-power red laser machine.
- Full dense samples of CuNi2SiCr were fabricated using the low-power green laser machine, achieving an optimal relative density of approximately 99.7% at a VED of around 275 J/mm^3. The range of VED required for fully dense samples is nearly within the optimal range identified for the medium-power red laser machine but slightly lower. This variance is attributed to the greater material absorption at the green laser compared to the red laser, owing to the distinct laser wavelengths. The high relative density corresponds to a minimal occurrence of defects, consisting primarily of gas porosities. The microstructure of the samples comprises columnar grains aligned parallel to the growth direction, accompanied by the presence of melt pools, consistent with observations made in the low-power samples.
- The highest hardness values for the CuNi2SiCr alloy in the as built condition were obtained with samples produced by the medium-power red laser and low-power green laser, measuring 104 ± 3 HV and 100 ± 4 HV, respectively. In contrast, samples produced with low-power red laser exhibited lower hardness values of 93 ± 11 HV due to the presence of numerous porosities within the samples.

- The heat treatments that resulted in the highest mechanical properties were DA1 and S-T6-1. DA1 exhibited YS and UTS values of 358 ± 8 MPa and 466 ± 9 MPa, respectively, while S-T6-1 exhibited YS and UTS values of 355 ± 4 MPa and 458 ± 8 MPa, respectively. The DA6 and S-T6-6 conditions exhibited slightly lower mechanical properties compared to the DA1 and S-T6-1 conditions, but they achieved the highest electrical conductivity value of 37% IACS. No significant differences were observed between direct aging and short T6 heat treatments.
- During the aging heat treatment, there was a noticeable reduction in grain size, with increasing duration leading to further grain refinement and the appearance of equiaxial grains. This grain refinement is attributed to the heat treatment performed at 540°C, exceeding the recrystallization temperature of approximately 450°C, which facilitates the formation of a new set of strain-free and equiaxial grains.
- The HIPping process effectively diminished porosities and notably enhanced the relative density of the samples, nearing 99% from an initial 94%. Nonetheless, the presence of defects like cracks and unmelted particles persists, underscoring the need to optimize the duration of the HIP process. Merely conducting the HIPping process for 15 minutes is inadequate for attaining full density in the part, especially when simultaneously employing it for solutioning treatment.

Future work in this area could involve the study of different process parameters to modify the internal microstructure with specific textures and the thermal properties after heat treatments. Additionally, deeper microstructural analyses could be conducted using a transmission electron microscope (TEM) to evaluate precipitates and their dimensions, enabling correlation of precipitate size with reinforcement behavior. Further studies can be conducted on the HIP process to achieve full densification of the samples, with a focus on correlating this densification with the assessment of their mechanical and electrical properties.

References

1. F42 Committee *Terminology for Additive Manufacturing Technologies,*; ASTM International;
2. Aboulkhair, N.T.; Everitt, N.M.; Ashcroft, I.; Tuck, C. Reducing Porosity in AlSi10Mg Parts Processed by Selective Laser Melting. *Addit. Manuf.* **2014**, *1–4*, 77–86, doi:10.1016/j.addma.2014.08.001.
3. Blakey-Milner, B.; Gradl, P.; Snedden, G.; Brooks, M.; Pitot, J.; Lopez, E.; Leary, M.; Berto, F.; Du Plessis, A. Metal Additive Manufacturing in Aerospace: A Review. *Mater. Des.* **2021**, *209*, 110008, doi:10.1016/j.matdes.2021.110008.
4. Kruth, J.P.; Wang, X.; Laoui, T.; Froyen, L. Research Article Lasers and Materials in Selective Laser Sintering. *Assem. Autom.* **2003**, *23*.
5. Yang, L.; Hsu, K.; Baughman, B.; Godfrey, D.; Medina, F.; Menon, M.; Wiener, S. *Additive Manufacturing of Metals: The Technology, Materials, Design and Production*; Springer series in advanced manufacturing / series editor, D. T. Pham; Springer International Publishing: Netherlands, 2017; ISBN 978-3-319-55128-9.
6. Gibson, I.; Rosen, D.; Stucker, B. *Additive Manufacturing Technologies: 3D Printing, Rapid Prototyping, and Direct Digital Manufacturing*; Springer New York: New York, NY, 2015; ISBN 978-1-4939-2112-6.
7. Dev Singh, D.; Arjula, S.; Raji Reddy, A. Functionally Graded Materials Manufactured by Direct Energy Deposition: A Review. *Mater. Today Proc.* **2021**, *47*, 2450–2456, doi:10.1016/j.matpr.2021.04.536.
8. Frazier, W.E. Metal Additive Manufacturing: A Review. *J. Mater. Eng. Perform.* **2014**, *23*, 1917–1928, doi:10.1007/s11665-014-0958-z.
9. Ding, D.; Pan, Z.; Cuiuri, D.; Li, H. Wire-Feed Additive Manufacturing of Metal Components: Technologies, Developments and Future Interests. *Int. J. Adv. Manuf. Technol.* **2015**, *81*, 465–481, doi:10.1007/s00170-015-7077-3.
10. Osipovich, K.; Kalashnikov, K.; Chumaevskii, A.; Gurianov, D.; Kalashnikova, T.; Vorontsov, A.; Zykova, A.; Utyaganova, V.; Panfilov, A.; Nikolaeva, A.; et al. Wire-Feed Electron Beam Additive Manufacturing: A Review. *Metals* **2023**, *13*, 279, doi:10.3390/met13020279.

11. Herzog, D.; Seyda, V.; Wycisk, E.; Emmelmann, C. Additive Manufacturing of Metals. *Acta Mater.* **2016**, *117*, 371–392, doi:10.1016/j.actamat.2016.07.019.

12. Gruber, K.; Smolina, I.; Kasprowicz, M.; Kurzynowski, T. Evaluation of Inconel 718 Metallic Powder to Optimize the Reuse of Powder and to Improve the Performance and Sustainability of the Laser Powder Bed Fusion (LPBF) Process. *Materials* **2021**, *14*, 1538, doi:10.3390/ma14061538.

13. Megahed, S.; Aniko, V.; Schleifenbaum, J.H. Electron Beam-Melting and Laser Powder Bed Fusion of Ti6Al4V: Transferability of Process Parameters. *Metals* **2022**, *12*, 1332, doi:10.3390/met12081332.

14. Aversa, A.; Marchese, G.; Manfredi, D.; Lorusso, M.; Calignano, F.; Biamino, S.; Lombardi, M.; Fino, P.; Pavese, M. Laser Powder Bed Fusion of a High Strength Al-Si-Zn-Mg-Cu Alloy. *Metals* **2018**, *8*, 300, doi:10.3390/met8050300.

15. *ASM Handbook. Volume 24: Additive Manufacturing Processes / Volume Editors: David L. Bourell (University of Texas at Austin), William Frazier (Pilgrim Consulting LLC), Howard Kuhn (University of Pittsburgh), Mohsen Seifi (ASTM International)*; Bourell, D.L., Frazier, W., Kuhn, H., Seifi, M., ASM International, Eds.; ASM International: Materials Park, Ohio, 2020; ISBN 978-1-62708-288-4.

16. Tolochko, N.K.; Khlopkov, Y.V.; Mozzharov, S.E.; Ignatiev, M.B.; Laoui, T.; Titov, V.I. Absorptance of Powder Materials Suitable for Laser Sintering. *Rapid Prototyp. J.* **2000**, *6*, 155–161, doi:10.1108/13552540010337029.

17. Alphonso, W.E.; Bayat, M.; Hattel, J.H. Comparison between Green and Infrared Laser in Laser Powder Bed Fusion of Pure Copper through High Fidelity Numerical Modelling at Meso-Scale. **2022**, doi:10.13140/RG.2.2.18214.60482.

18. Von Lintel, H.; Evsiutkina, E.; Haase, C.; Krupp, U.; Jahns, K. Copper Alloys for Additive Manufacturing: Laser Powder Bed Fusion of CuCr1Zr by Using a Green Qcw-Laser. *Eur. J. Mater.* **2022**, 1–17, doi:10.1080/26889277.2022.2115945.

19. Cheng, B.; Shrestha, S.; Chou, K. Stress and Deformation Evaluations of Scanning Strategy Effect in Selective Laser Melting. *Addit. Manuf.* **2016**, *12*, 240–251, doi:10.1016/j.addma.2016.05.007.

20. Spierings, A.B.; Starr, T.L.; Wegener, K. Fatigue Performance of Additive Manufactured Metallic Parts. *Rapid Prototyp. J.* **2013**, *19*, 88–94, doi:10.1108/13552541311302932.

21. Su, X.; Yang, Y. Research on Track Overlapping during Selective Laser Melting of Powders. *J. Mater. Process. Technol.* **2012**, *212*, 2074–2079, doi:10.1016/j.jmatprotec.2012.05.012.

22. Carter, L.N.; Martin, C.; Withers, P.J.; Attallah, M.M. The Influence of the Laser Scan Strategy on Grain Structure and Cracking Behaviour in SLM Powder-Bed Fabricated Nickel Superalloy. *J. Alloys Compd.* **2014**, *615*, 338–347, doi:10.1016/j.jallcom.2014.06.172.

23. Mercelis, P.; Kruth, J.-P. Residual Stresses in Selective Laser Sintering and Selective Laser Melting. *Rapid Prototyp. J.* **2006**, *12*, doi:10.1108/13552540610707013.

24. Kruth, J.P.; Froyen, L.; Van Vaerenbergh, J.; Mercelis, P.; Rombouts, M.; Lauwers, B. Selective Laser Melting of Iron-Based Powder. *J. Mater. Process. Technol.* **2004**, *149*, 616–622, doi:10.1016/j.jmatprotec.2003.11.051.

25. Kempen, K.; Thijs, L.; Vrancken, B.; Buls, S.; Humbeeck, J.V. Lowering Thermal Gradients in Selective Laser Melting by Pre-Heating the Baseplate.

26. Attar, H.; Calin, M.; Zhang, L.C.; Scudino, S.; Eckert, J. Manufacture by Selective Laser Melting and Mechanical Behavior of Commercially Pure Titanium. *Mater. Sci. Eng. A* **2014**, *593*, 170–177, doi:10.1016/j.msea.2013.11.038.

27. Ferrar, B.; Mullen, L.; Jones, E.; Stamp, R.; Sutcliffe, C.J. Gas Flow Effects on Selective Laser Melting (SLM) Manufacturing Performance. *J. Mater. Process. Technol.* **2012**, *212*, 355–364, doi:10.1016/j.jmatprotec.2011.09.020.

28. Legutko, S. Additive Techniques of Manufacturing Functional Products from Metal Materials. *IOP Conf. Ser. Mater. Sci. Eng.* **2018**, *393*, 012003, doi:10.1088/1757-899X/393/1/012003.

29. Bol, E.; Ramulu, M. Dimensional Accuracy of Electron Beam Powder Bed Fusion with Ti-6Al-4V. *Designs* **2023**, *7*, 53, doi:10.3390/designs7020053.

30. Gong, X.; Anderson, T.; Chou, K. Review on Powder-Based Electron Beam Additive Manufacturing Technology. *Manuf. Rev.* **2014**, *1*, 2, doi:10.1051/mfreview/2014001.

31. Fu, Z.; Körner, C. Actual State-of-the-Art of Electron Beam Powder Bed Fusion. *Eur. J. Mater.* **2022**, *2*, 54–116, doi:10.1080/26889277.2022.2040342.

32. Murr, L.E.; Gaytan, S.M.; Ramirez, D.A.; Martinez, E.; Hernandez, J.; Amato, K.N.; Shindo, P.W.; Medina, F.R.; Wicker, R.B. Metal Fabrication by Additive Manufacturing Using Laser and Electron Beam Melting

Technologies. *J. Mater. Sci. Technol.* **2012**, *28*, 1–14, doi:10.1016/S1005-0302(12)60016-4.

33. Chowdhury, S.; Yadaiah, N.; Prakash, C.; Ramakrishna, S.; Dixit, S.; Gupta, L.R.; Buddhi, D. Laser Powder Bed Fusion: A State-of-the-Art Review of the Technology, Materials, Properties & Defects, and Numerical Modelling. *J. Mater. Res. Technol.* **2022**, *20*, 2109–2172, doi:10.1016/j.jmrt.2022.07.121.

34. Gu, D.; Shen, Y. Balling Phenomena in Direct Laser Sintering of Stainless Steel Powder: Metallurgical Mechanisms and Control Methods. *Mater. Des.* **2009**, *30*, 2903–2910, doi:10.1016/j.matdes.2009.01.013.

35. Gu, D.; Hagedorn, Y.-C.; Meiners, W.; Meng, G.; Batista, R.J.S.; Wissenbach, K.; Poprawe, R. Densification Behavior, Microstructure Evolution, and Wear Performance of Selective Laser Melting Processed Commercially Pure Titanium. *Acta Mater.* **2012**, *60*, 3849–3860, doi:10.1016/j.actamat.2012.04.006.

36. Dai, D.; Gu, D. Thermal Behavior and Densification Mechanism during Selective Laser Melting of Copper Matrix Composites: Simulation and Experiments. *Mater. Des.* **2014**, *55*, 482–491, doi:10.1016/j.matdes.2013.10.006.

37. Jia, Q.; Gu, D. Selective Laser Melting Additive Manufacturing of Inconel 718 Superalloy Parts: Densification, Microstructure and Properties. *J. Alloys Compd.* **2014**, *585*, 713–721, doi:10.1016/j.jallcom.2013.09.171.

38. Gui, Y.; Aoyagi, K.; Bian, H.; Chiba, A. Detection, Classification and Prediction of Internal Defects from Surface Morphology Data of Metal Parts Fabricated by Powder Bed Fusion Type Additive Manufacturing Using an Electron Beam. *Addit. Manuf.* **2022**, *54*, 102736, doi:10.1016/j.addma.2022.102736.

39. Monroy, K.; Delgado, J.; Ciurana, J. Study of the Pore Formation on CoCrMo Alloys by Selective Laser Melting Manufacturing Process. *Procedia Eng.* **2013**, *63*, 361–369, doi:10.1016/j.proeng.2013.08.227.

40. Wang, Y.; Bergström, J.; Burman, C. Characterization of an Iron-Based Laser Sintered Material. *J. Mater. Process. Technol.* **2006**, *172*, 77–87, doi:10.1016/j.jmatprotec.2005.09.004.

41. Xiao, R.; Zhang, X. Problems and Issues in Laser Beam Welding of Aluminum–Lithium Alloys. *J. Manuf. Process.* **2014**, *16*, 166–175, doi:10.1016/j.jmapro.2013.10.005.

42. Wang, W.; Ning, J.; Liang, S.Y. Analytical Prediction of Balling, Lack-of-Fusion and Keyholing Thresholds in Powder Bed Fusion. *Appl. Sci.* **2021**, *11*, 12053, doi:10.3390/app112412053.

43. Vastola, G.; Pei, Q.X.; Zhang, Y.-W. Predictive Model for Porosity in Powder-Bed Fusion Additive Manufacturing at High Beam Energy Regime. *Addit. Manuf.* **2018**, *22*, 817–822, doi:10.1016/j.addma.2018.05.042.

44. Cunningham, R.; Zhao, C.; Parab, N.; Kantzos, C.; Pauza, J.; Fezzaa, K.; Sun, T.; Rollett, A.D. Keyhole Threshold and Morphology in Laser Melting Revealed by Ultrahigh-Speed x-Ray Imaging. *Science* **2019**, *363*, 849–852, doi:10.1126/science.aav4687.

45. Li, Y.; Yang, H.; Lin, X.; Huang, W.; Li, J.; Zhou, Y. The Influences of Processing Parameters on Forming Characterizations during Laser Rapid Forming. *Mater. Sci. Eng. A* **2003**, *360*, 18–25, doi:10.1016/S0921-5093(03)00435-0.

46. Qiu, C.; Panwisawas, C.; Ward, M.; Basoalto, H.C.; Brooks, J.W.; Attallah, M.M. On the Role of Melt Flow into the Surface Structure and Porosity Development during Selective Laser Melting. *Acta Mater.* **2015**, *96*, 72–79, doi:10.1016/j.actamat.2015.06.004.

47. Cao, X.; Jahazi, M.; Immarigeon, J.P.; Wallace, W. A Review of Laser Welding Techniques for Magnesium Alloys. *J. Mater. Process. Technol.* **2006**, *171*, 188–204, doi:10.1016/j.jmatprotec.2005.06.068.

48. Ramasamy, S.; Albright, C.E. CO2 and Nd:YAG Laser Beam Welding of 6111-T4 Aluminum Alloy for Automotive Applications. *J. Laser Appl.* **2000**, *12*, 101–115, doi:10.2351/1.521923.

49. *Copper and Copper Alloys*; Davis, J.R., ASM International, Eds.; ASM specialty handbook; ASM International: Materials Park, OH, 2001; ISBN 978-0-87170-726-0.

50. Jiang, Q.; Zhang, P.; Yu, Z.; Shi, H.; Wu, D.; Yan, H.; Ye, X.; Lu, Q.; Tian, Y. A Review on Additive Manufacturing of Pure Copper. *Coatings* **2021**, *11*, 740, doi:10.3390/coatings11060740.

51. Hust, J.G.; Lankford, A.B. *Thermal Conductivity of Aluminium, Copper, Iron and Tungsten for Temperatures from 1 K to the Melting Point*; US. Nat. Bureau Stand.: Boulder, CO, 1984;

52. BS EN 13601:2021 Copper and Copper Alloys. Copper Rod, Bar and Wire for General Electrical Purposes.

53. Klassert, A.; Tikana, L. Copper and Copper–Nickel Alloys – an Overview. In *Corrosion Behaviour and Protection of Copper and Aluminium Alloys in Seawater*; Elsevier, 2007; pp. 47–61 ISBN 978-1-84569-241-4.

54. Monzen, R.; Watanabe, C. Microstructure and Mechanical Properties of Cu–Ni–Si Alloys. *Mater. Sci. Eng. A* **2008**, *483–484*, 117–119, doi:10.1016/j.msea.2006.12.163.

55. Gruber, S.; Stepien, L.; López, E.; Brueckner, F.; Leyens, C. Physical and Geometrical Properties of Additively Manufactured Pure Copper Samples Using a Green Laser Source. *Materials* **2021**, *14*, 3642, doi:10.3390/ma14133642.

56. Sobotova, L.; Badida, M. Laser Marking as Environment Technology. *Open Eng.* **2017**, *7*, 303–316, doi:10.1515/eng-2017-0030.

57. Tran, T.Q.; Chinnappan, A.; Lee, J.K.Y.; Loc, N.H.; Tran, L.T.; Wang, G.; Kumar, V.V.; Jayathilaka, W.A.D.M.; Ji, D.; Doddamani, M.; et al. 3D Printing of Highly Pure Copper. *Metals* **2019**, *9*, 756, doi:10.3390/met9070756.

58. Lodes, M.A.; Guschlbauer, R.; Körner, C. Process Development for the Manufacturing of 99.94% Pure Copper via Selective Electron Beam Melting. *Mater. Lett.* **2015**, *143*, 298–301, doi:10.1016/j.matlet.2014.12.105.

59. El-Wardany, T.I.; She, Y.; Jagdale, V.N.; Garofano, J.K.; Liou, J.J.; Schmidt, W.R. Challenges in Three-Dimensional Printing of High-Conductivity Copper. *J. Electron. Packag.* **2018**, *140*, 020907, doi:10.1115/1.4039974.

60. Jadhav; Dadbakhsh; Vleugels; Hofkens; Puyvelde; Yang; Kruth; Humbeeck; Vanmeensel Influence of Carbon Nanoparticle Addition (and Impurities) on Selective Laser Melting of Pure Copper. *Materials* **2019**, *12*, 2469, doi:10.3390/ma12152469.

61. Jadhav, S.D.; Dhekne, P.P.; Dadbakhsh, S.; Kruth, J.-P.; Van Humbeeck, J.; Vanmeensel, K. Surface Modified Copper Alloy Powder for Reliable Laser-Based Additive Manufacturing. *Addit. Manuf.* **2020**, *35*, 101418, doi:10.1016/j.addma.2020.101418.

62. Roccetti Campagnoli, M.; Galati, M.; Saboori, A. On the Processability of Copper Components via Powder-Based Additive Manufacturing Processes: Potentials, Challenges and Feasible Solutions. *J. Manuf. Process.* **2021**, *72*, 320–337, doi:10.1016/j.jmapro.2021.10.038.

63. Sing, S.L.; Lam, L.P.; Zhang, D.Q.; Liu, Z.H.; Chua, C.K. Interfacial Characterization of SLM Parts in Multi-Material Processing: Intermetallic Phase Formation between AlSi10Mg and C18400 Copper Alloy. *Mater. Charact.* **2015**, *107*, 220–227, doi:10.1016/j.matchar.2015.07.007.

64. Zhang, D.Q.; Liu, Z.H.; Chua, C.K. Investigation on Forming Process of Copper Alloys via Selective Laser Melting. In; 2013; pp. 285–289 ISBN 978-1-138-00137-4.

65. Liu, Z.H.; Zhang, D.Q.; Sing, S.L.; Chua, C.K.; Loh, L.E. Interfacial Characterization of SLM Parts in Multi-Material Processing: Metallurgical Diffusion between 316L Stainless Steel and C18400 Copper Alloy. *Mater. Charact.* **2014**, *94*, 116–125, doi:10.1016/j.matchar.2014.05.001.

66. Uhlmann, E.; Tekkaya, A.E.; Kashevko, V.; Gies, S.; Reimann, R.; John, P. Qualification of CuCr1Zr for the SLM Process. **2016**, doi:10.17877/DE290R-16984.

67. Wallis, C.; Buchmayr, B. Effect of Heat Treatments on Microstructure and Properties of CuCrZr Produced by Laser-Powder Bed Fusion. *Mater. Sci. Eng. A* **2019**, *744*, 215–223, doi:10.1016/j.msea.2018.12.017.

68. Buchmayr, B.; Panzl, G.; Walzl, A.; Wallis, C. Laser Powder Bed Fusion – Materials Issues and Optimized Processing Parameters for Tool Steels, AlSiMg- and CuCrZr-Alloys. *Adv. Eng. Mater.* **2017**, *19*, 1600667, doi:10.1002/adem.201600667.

69. Popovich, A.; Sufiiarov, V.; Polozov, I.; Borisov, E.; Masaylo, D.; Orlov, A. Microstructure and Mechanical Properties of Additive Manufactured Copper Alloy. *Mater. Lett.* **2016**, *179*, 38–41, doi:10.1016/j.matlet.2016.05.064.

70. Zhang, S.; Zhu, H.; Zhang, L.; Zhang, W.; Yang, H.; Zeng, X. Microstructure and Properties in QCr0.8 Alloy Produced by Selective Laser Melting with Different Heat Treatment. *J. Alloys Compd.* **2019**, *800*, 286–293, doi:10.1016/j.jallcom.2019.06.018.

71. Zhang, S.; Zhu, H.; Zhang, L.; Zhang, W.; Yang, H.; Zeng, X. Microstructure and Properties of High Strength and High Conductivity Cu-Cr Alloy Components Fabricated by High Power Selective Laser Melting. *Mater. Lett.* **2019**, *237*, 306–309, doi:10.1016/j.matlet.2018.11.118.

72. Uchida, S.; Kimura, T.; Nakamoto, T.; Ozaki, T.; Miki, T.; Takemura, M.; Oka, Y.; Tsubota, R. Microstructures and Electrical and Mechanical Properties of Cu-Cr Alloys Fabricated by Selective Laser Melting. *Mater. Des.* **2019**, *175*, 107815, doi:10.1016/j.matdes.2019.107815.

73. Momeni, S.; Guschlbauer, R.; Osmanlic, F.; Körner, C. Selective Electron Beam Melting of a Copper-Chrome Powder Mixture. *Mater. Lett.* **2018**, *223*, 250–252, doi:10.1016/j.matlet.2018.03.194.

74. Chen, Y.; Ren, S.; Zhao, Y.; Qu, X. Microstructure and Properties of CuCr Alloy Manufactured by Selective Laser Melting. *J. Alloys Compd.* **2019**, *786*, 189–197, doi:10.1016/j.jallcom.2019.01.179.

75. Mašek, J.; Koutny, D.; Popela, R. Thermal Conductivity of Cu7.2Ni1.8Si1Cr Copper Alloy Produced via SLM and Ability of Thin-Wall Structure Fabrication.; January 1 2019; pp. 119–129.

76. Palousek, D.; Kocica, M.; Pantelejev, L.; Klakurkova, L.; Celko, L.; Koutny, D.; Kaiser, J. SLM Process Parameters Development of Cu-Alloy Cu7.2Ni1.8Si1Cr. *Rapid Prototyp. J.* **2018**, *25*, 266–276, doi:10.1108/RPJ-06-2017-0116.

77. Kratochvilova, V.; Vlasic, F.; Mazal, P.; Palousek, D. Fatigue Behaviour Evaluation of Additively and Conventionally Produced Materials by Acoustic Emission Method. *Procedia Struct. Integr.* **2017**, *5*, 393–400, doi:10.1016/j.prostr.2017.07.187.

78. Zhang, D.Q.; Liu, Z.H.; Li, S.; Muzzammil, Muhd.; Wong, C.H.; Chua, C.K. Selective Laser Melting: On the Study of Microstructure of K220. In Proceedings of the Proceedings of the 1st International Conference on Progress in Additive Manufacturing; Research Publishing Services, 2014; pp. 176–184.

79. Fu, T.; Yeong, W.Y.; Chen, S. SELECTIVE LASER MELTING OF COPPER BASED ALLOY ON STEEL: A PRELIMINARY STUDY.; May 16 2016.

80. Tiberto, D.; Klotz, U.E.; Held, F.; Wolf, G. Additive Manufacturing of Copper Alloys: Influence of Process Parameters and Alloying Elements. *Mater. Sci. Technol.* **2019**, *35*, 969–977, doi:10.1080/02670836.2019.1600840.

81. Zhou, Y.; Zeng, X.; Yang, Z.; Wu, H. Effect of Crystallographic Textures on Thermal Anisotropy of Selective Laser Melted Cu-2.4Ni-0.7Si Alloy. *J. Alloys Compd.* **2018**, *743*, 258–261, doi:10.1016/j.jallcom.2018.01.335.

82. Ventura, A.P.; Marvel, C.J.; Pawlikowski, G.; Bayes, M.; Watanabe, M.; Vinci, R.P.; Misiolek, W.Z. The Effect of Aging on the Microstructure of Selective Laser Melted Cu-Ni-Si. *Metall. Mater. Trans. A* **2017**, *48*, 6070–6082, doi:10.1007/s11661-017-4363-8.

83. Zhang, G.; Chen, C.; Wang, X.; Wang, P.; Zhang, X.; Gan, X.; Zhou, K. Additive Manufacturing of Fine-Structured Copper Alloy by Selective Laser Melting of Pre-Alloyed Cu-15Ni-8Sn Powder. *Int. J. Adv. Manuf. Technol.* **2018**, *96*, 4223–4230, doi:10.1007/s00170-018-1891-3.

84. Stašić, J.; Trtica, M.; Rajkovic, V.; Ružić, J.; Božić, D. Laser Sintering of Cu–Zr–ZrB2 Composite. *Appl. Surf. Sci.* **2014**, *321*, 353–357, doi:10.1016/j.apsusc.2014.10.021.

85. Mao, Z.; Zhang, D.Z.; Wei, P.; Zhang, K. Manufacturing Feasibility and Forming Properties of Cu-4Sn in Selective Laser Melting. *Materials* **2017**, *10*, 333, doi:10.3390/ma10040333.

86. Ventura, A.P.; Wade, C.A.; Pawlikowski, G.; Bayes, M.; Watanabe, M.; Misiolek, W.Z. Mechanical Properties and Microstructural Characterization of Cu-4.3 Pct Sn Fabricated by Selective Laser Melting. *Metall. Mater. Trans. A* **2017**, *48*, 178–187, doi:10.1007/s11661-016-3779-x.

87. Scudino, S.; Unterdörfer, C.; Prashanth, K.G.; Attar, H.; Ellendt, N.; Uhlenwinkel, V.; Eckert, J. Additive Manufacturing of Cu–10Sn Bronze. *Mater. Lett.* **2015**, *156*, 202–204, doi:10.1016/j.matlet.2015.05.076.

88. Syed-Khaja, A.; Perez, P.P.; Franke, J. Production and Characterization of High-Temperature Substrates through Selective Laser Melting (SLM) for Power Electronics. In Proceedings of the 2016 IEEE CPMT Symposium Japan (ICSJ); November 2016; pp. 255–258.

89. Deng, C.; Kang, J.; Feng, T.; Feng, Y.; Wang, X.; Wu, P. Study on the Selective Laser Melting of CuSn10 Powder. *Materials* **2018**, *11*, 614, doi:10.3390/ma11040614.

90. Mao, Z.; Zhang, D.Z.; Jiang, J.; Fu, G.; Zhang, P. Processing Optimisation, Mechanical Properties and Microstructural Evolution during Selective Laser Melting of Cu-15Sn High-Tin Bronze. *Mater. Sci. Eng. A* **2018**, *721*, 125–134, doi:10.1016/j.msea.2018.02.051.

91. Zhang, S.; Zhu, H.; Hu, Z.; Zeng, X.; Zhong, F. Selective Laser Melting of Cu 10Zn Alloy Powder Using High Laser Power. *Powder Technol.* **2019**, *342*, 613–620, doi:10.1016/j.powtec.2018.10.002.

92. Yang, C.; Zhao, Y.J.; Kang, L.M.; Li, D.D.; Zhang, W.W.; Zhang, L.C. High-Strength Silicon Brass Manufactured by Selective Laser Melting. *Mater. Lett.* **2018**, *210*, 169–172, doi:10.1016/j.matlet.2017.09.011.

93. Mahale, T. Electron Beam Melting of Advanced Materials and Structures. **2009**.

94. Hayes, C.; Brown, E.; Kappes, B. Characterization of Selective Laser Melted GRCop-84. In *2018 Joint Propulsion Conference*; AIAA Propulsion and Energy Forum; American Institute of Aeronautics and Astronautics, 2018.

95. Onuike, B.; Bandyopadhyay, A. Bond Strength Measurement for Additively Manufactured Inconel 718- GRCop84 Copper Alloy Bimetallic Joints. *Addit. Manuf.* **2019**, *27*, 576–585, doi:10.1016/j.addma.2019.04.003.

96. Onuike, B.; Heer, B.; Bandyopadhyay, A. Additive Manufacturing of Inconel 718—Copper Alloy Bimetallic Structure Using Laser Engineered Net Shaping (LENS^{TM}). *Addit. Manuf.* **2018**, *21*, 133–140, doi:10.1016/j.addma.2018.02.007.

97. Gradl, P.; Protz, C.; Greene, S.; Ellis, D.; Lerch, B.; Locci, I. Development and Hot-Fire Testing of Additively Manufactured Copper Combustion Chambers for Liquid Rocket Engine Applications.; July 10 2017.

98. Pobel, C.R.; Lodes, M.A.; Körner, C. Selective Electron Beam Melting of Oxide Dispersion Strengthened Copper. *Adv. Eng. Mater.* **2018**, *20*, 1800068, doi:10.1002/adem.201800068.

99. Gradl, P.; Mireles, O.; Andrews, N. Introduction to Additive Manufacturing for Propulsion Systems. 2019.

100. Protz, C.; Bowman, R.; Cooper, K.; Fikes, J.; Taminger, K.; Wright, B. Additive Manufacturing of Low Cost Upper Stage Propulsion Components.; Huntsville, AL, September 3 2014.

101. Misra, A.K.; Grady, J.E.; Carter, R. Additive Manufacturing of Aerospace Propulsion Components. 2015.

102. Ellis, D.L. *GRCop-84: A High-Temperature Copper Alloy for High-Heat-Flux Applications*; 2005;

103. Suresh, T.; Landes, S.; Letcher, T.; Prasad, A.; Gradl, P.; Ellis, D. Nanomechanical Characterization of Additive Manufactured GRCop-42 Alloy Developed by Directed Energy Deposition Methods. In Proceedings of the Volume 4: Advances in Aerospace Technology; American Society of Mechanical Engineers: Virtual, Online, November 16 2020; p. V004T04A003.

104. Gradl, P.R.; Protz, C.S.; Cooper, K.; Ellis, D.; Evans, L.J.; Garcia, C. GRCop-42 Development and Hot-Fire Testing Using Additive Manufacturing Powder Bed Fusion for Channel-Cooled Combustion Chambers. In Proceedings of the AIAA Propulsion and Energy 2019 Forum; American Institute of Aeronautics and Astronautics: Indianapolis, IN, August 19 2019.

105. Cooper, K.G.; Lydon, J.L.; LeCorre, M.D.; Jones, Z.C.; Scannapieco, D.S.; Ellis, D.L.; Lerch, B.A. Three-Dimensional Printing GRCop-42. 20.

106. Gustmann, T.; Neves, A.; Kühn, U.; Gargarella, P.; Kiminami, C.S.; Bolfarini, C.; Eckert, J.; Pauly, S. Influence of Processing Parameters on the Fabrication of a Cu-Al-Ni-Mn Shape-Memory Alloy by Selective Laser Melting. *Addit. Manuf.* **2016**, *11*, 23–31, doi:10.1016/j.addma.2016.04.003.

107. Marchezini Mazzer, E.; Kiminami, C.; Gargarella, P.; Cava, R.; Basilio, L.; Bolfarini, C.; Botta, W.; Eckert, J.; Gustmann, T.; Pauly, S. Atomization and Selective Laser Melting of a Cu-Al-Ni-Mn Shape Memory Alloy. *Mater. Sci. Forum* **2014**, *802*, 343–348, doi:10.4028/www.scientific.net/MSF.802.343.

108. Gargarella, P.; Kiminami, C.; Marchezini Mazzer, E.; Cava, R.; Basilio, L.; Bolfarini, C.; Botta, W.; Eckert, J.; Gustmann, T.; Pauly, S. Phase Formation, Thermal Stability and Mechanical Properties of a Cu-Al-Ni-Mn Shape Memory Alloy Prepared by Selective Laser Melting. *Mater. Res.* **2015**, *18*, doi:10.1590/1516-1439.338914.

109. Gustmann, T.; dos Santos, J.M.; Gargarella, P.; Kühn, U.; Van Humbeeck, J.; Pauly, S. Properties of Cu-Based Shape-Memory Alloys Prepared by

Selective Laser Melting. *Shape Mem. Superelasticity* **2017**, *3*, 24–36, doi:10.1007/s40830-016-0088-6.

110. Jadhav, S.D.; Dadbakhsh, S.; Goossens, L.; Kruth, J.-P.; Van Humbeeck, J.; Vanmeensel, K. Influence of Selective Laser Melting Process Parameters on Texture Evolution in Pure Copper. *J. Mater. Process. Technol.* **2019**, *270*, 47–58, doi:10.1016/j.jmatprotec.2019.02.022.

111. Guan, J.; Zhang, X.; Jiang, Y.; Yan, Y. Insights into Fabrication Mechanism of Pure Copper Thin Wall Components by Selective Infrared Laser Melting. *Rapid Prototyp. J.* **2019**, *25*, 1388–1397, doi:10.1108/RPJ-06-2018-0143.

112. Jadhav, S.D.; Goossens, L.R.; Kinds, Y.; Hooreweder, B.V.; Vanmeensel, K. Laser-Based Powder Bed Fusion Additive Manufacturing of Pure Copper. *Addit. Manuf.* **2021**, *42*, 101990, doi:10.1016/j.addma.2021.101990.

113. Jadhav, S.D.; Vleugels, J.; Kruth, J.; Van Humbeeck, J.; Vanmeensel, K. Mechanical and Electrical Properties of Selective Laser-melted Parts Produced from Surface-oxidized Copper Powder. *Mater. Des. Process. Commun.* **2020**, *2*, doi:10.1002/mdp2.94.

114. Ikeshoji, T.-T.; Nakamura, K.; Yonehara, M.; Imai, K.; Kyogoku, H. Selective Laser Melting of Pure Copper. *JOM* **2018**, *70*, 396–400, doi:10.1007/s11837-017-2695-x.

115. Yan, X.; Chang, C.; Dong, D.; Gao, S.; Ma, W.; Liu, M.; Liao, H.; Yin, S. Microstructure and Mechanical Properties of Pure Copper Manufactured by Selective Laser Melting. *Mater. Sci. Eng. A* **2020**, *789*, 139615, doi:10.1016/j.msea.2020.139615.

116. Colopi, M.; Demir, A.G.; Caprio, L.; Previtali, B. Limits and Solutions in Processing Pure Cu via Selective Laser Melting Using a High-Power Single-Mode Fiber Laser. *Int. J. Adv. Manuf. Technol.* **2019**, *104*, 2473–2486, doi:10.1007/s00170-019-04015-3.

117. Colopi, M.; Caprio, L.; Demir, A.G.; Previtali, B. Selective Laser Melting of Pure Cu with a 1 kW Single Mode Fiber Laser. *Procedia CIRP* **2018**, *74*, 59–63, doi:10.1016/j.procir.2018.08.030.

118. Silbernagel, C.; Gargalis, L.; Ashcroft, I.; Hague, R.; Galea, M.; Dickens, P. Electrical Resistivity of Pure Copper Processed by Medium-Powered Laser Powder Bed Fusion Additive Manufacturing for Use in Electromagnetic Applications. *Addit. Manuf.* **2019**, *29*, 100831, doi:10.1016/j.addma.2019.100831.

119. Lykov, P.A.; Safonov, E.V.; Akhmedianov, A.M. Selective Laser Melting of Copper. *Mater. Sci. Forum* **2016**, *843*, 284–288, doi:10.4028/www.scientific.net/MSF.843.284.

120. Huang, J.; Yan, X.; Chang, C.; Xie, Y.; Ma, W.; Huang, R.; Zhao, R.; Li, S.; Liu, M.; Liao, H. Pure Copper Components Fabricated by Cold Spray (CS) and Selective Laser Melting (SLM) Technology. *Surf. Coat. Technol.* **2020**, *395*, 125936, doi:10.1016/j.surfcoat.2020.125936.

121. Stoll, T.; Trautnitz, P.; Schmiedeke, S.; Franke, J.; Travitzky, N. Process Development for Laser Powder Bed Fusion of Pure Copper. In Proceedings of the Laser 3D Manufacturing VII; SPIE, March 2 2020; Vol. 11271, pp. 24–38.

122. Singh, A.; Caprio, L.; Previtali, B.; Demir, A.G. Processability of Pure Cu by LPBF Using a Ns-Pulsed Green Fiber Laser. *Opt. Laser Technol.* **2022**, *154*, 108310, doi:10.1016/j.optlastec.2022.108310.

123. Wagenblast, P.; Myrell, A.; Thielmann, M.; Scherbaum, T.; Coupek, D. Additive Manufacturing with Green Disk Lasers. In Proceedings of the Laser 3D Manufacturing VII; Helvajian, H., Gu, B., Chen, H., Eds.; SPIE: San Francisco, United States, March 2 2020; p. 18.

124. de Terris, T.; Baffie, T.; Ribière, C. Comparison of Two Different Methods to Manufacture Pure Copper by Laser-Powder Bed Fusion (L-PBF). *Ferr. Mater.*

125. Raab, S.J.; Guschlbauer, R.; Lodes, M.A.; Körner, C. Thermal and Electrical Conductivity of 99.9% Pure Copper Processed via Selective Electron Beam Melting: Conductivities of Pure SEBM-Copper. *Adv. Eng. Mater.* **2016**, *18*, 1661–1666, doi:10.1002/adem.201600078.

126. Guschlbauer, R.; Burkhardt, A.K.; Fu, Z.; Körner, C. Effect of the Oxygen Content of Pure Copper Powder on Selective Electron Beam Melting. *Mater. Sci. Eng. A* **2020**, *779*, 139106, doi:10.1016/j.msea.2020.139106.

127. Guschlbauer, R.; Momeni, S.; Osmanlic, F.; Körner, C. Process Development of 99.95% Pure Copper Processed via Selective Electron Beam Melting and Its Mechanical and Physical Properties. *Mater. Charact.* **2018**, *143*, 163–170, doi:10.1016/j.matchar.2018.04.009.

128. Gamzina, D.; Luhmann, N.C.; Ledford, C.; Horn, T.; Karakaut, I.; Lin, L.; Frigola, P. Additive Vacuum Electronics: Electron Beam Melting of Copper. In Proceedings of the 2017 Eighteenth International Vacuum Electronics Conference (IVEC); IEEE: London, April 2017; pp. 1–2.

129. Ledford, C.; Rock, C.; Carriere, P.; Frigola, P.; Gamzina, D.; Horn, T. Characteristics and Processing of Hydrogen-Treated Copper Powders for EB-PBF Additive Manufacturing. *Appl. Sci.* **2019**, *9*, 3993, doi:10.3390/app9193993.

130. Ledford, C.; Rock, C.; Tung, M.; Wang, H.; Schroth, J.; Horn, T. Evaluation of Electron Beam Powder Bed Fusion Additive Manufacturing of High

Purity Copper for Overhang Structures Using In-Situ Real Time Backscatter Electron Monitoring. *Procedia Manuf.* **2020**, *48*, 828–838, doi:10.1016/j.promfg.2020.05.120.

131. Frigola, P.; Harryson, O.A.; West, H.A.; Aman, R.L.; Rigsbee, J.M. Fabricating Copper Components with Electron Beam Melting. **2014**, 5.
132. De Terris, T.; Baffie, T.; Ribière, C. Additive Manufacturing of Pure Copper: A Review and Comparison of Physical, Microstructural, and Mechanical Properties of Samples Manufactured with Laser-Powder Bed Fusion (L-PBF), Electron Beam Melting (EBM) and Metal Fused Deposition Modelling (MFDM) Technologies. *Int. J. Mater. Form.* **2023**, *16*, 32, doi:10.1007/s12289-023-01755-2.
133. Semboshi, S.; Sato, S.; Iwase, A.; Takasugi, T. Discontinuous Precipitates in Age-Hardening CuNiSi Alloys. *Mater. Charact.* **2016**, *115*, 39–45, doi:10.1016/j.matchar.2016.03.017.
134. B09 Committee Test Methods for Flow Rate of Metal Powders Using the Hall Flowmeter Funnel.
135. B09 Committee Test Method for Apparent Density of Free-Flowing Metal Powders Using the Hall Flowmeter Funnel.
136. B09 Committee Test Method for Tap Density of Metal Powders and Compounds.
137. B09 Committee Test Method for Metal Powder Skeletal Density by Helium or Nitrogen Pycnometry.
138. Concept Laser_MlabFamily_machine | GE Additive Available online: https://www.ge.com/additive/additive-manufacturing/machines/dmlm-machines/mlab-family.
139. Print Sharp 250 | Prima Additive Available online: https://www.primaadditive.com/it/tecnologie/powder-bed-fusion/print-sharp-250 (accessed on 14 September 2023).
140. Print Green 150 | Prima Additive Available online: https://www.primaadditive.com/it/tecnologie/powder-bed-fusion/print-green-150.
141. Freemelt ONE: The 3D Printer for Materials R&D Available online: https://freemelt.com/freemelt-one/.
142. Edens, W.W.; Ingerson, Q.F. Copper-Nickel-Silicon-Chromium Alloy Having Improved Electrical Conductivity 1980.
143. Vanzetti, M.; Virgillito, E.; Aversa, A.; Manfredi, D.; Bondioli, F.; Lombardi, M.; Fino, P. Short Heat Treatments for the F357 Aluminum Alloy

Processed by Laser Powder Bed Fusion. *Materials* **2021**, *14*, 6157, doi:10.3390/ma14206157.

144. Suvorova, A.A.; Korostelev, A.B.; Goslavskii, O.V. Hot Isostatic Pressing Temperature Effect on Chromium-Zirconium Copper Alloy Structure and Properties. *At. Energy* **2021**, *130*, 285–289, doi:10.1007/s10512-021-00810-y.

145. E04 Committee *Practice for Microetching Metals and Alloys*; ASTM International;

146. Fiji: ImageJ, with "Batteries Included" Available online: https://fiji.sc/.

147. Standard Test Methods for Vickers Hardness and Knoop Hardness of Metallic Materials Available online: https://www.astm.org/e0092-17.html (accessed on 4 June 2023).

148. Standard Test Methods for Tension Testing of Metallic Materials Available online: https://www.astm.org/e0008_e0008m-21.html.

149. Sanchez, J.C.; Murr, L.E.; Staudhammer, K.P. Effect of Grain Size and Pressure on Twinning and Microbanding in Oblique Shock Loading of Copper Rods. *Acta Mater.* **1997**, *45*, 3223–3235, doi:10.1016/S1359-6454(97)00018-9.

150. Meng, X.; Xie, G.; Xue, W.; Fu, Y.; Wang, R.; Liu, X. The Precipitation Behavior of a Cu-Ni-Si Alloy with Cr Addition Prepared by Heating-Cooling Combined Mold (HCCM) Continuous Casting. *Materials* **2022**, *15*, 4521, doi:10.3390/ma15134521.

151. Cheng, J.Y.; Tang, B.B.; Yu, F.X.; Shen, B. Evaluation of Nanoscaled Precipitates in a Cu–Ni–Si–Cr Alloy during Aging. *J. Alloys Compd.* **2014**, *614*, 189–195, doi:10.1016/j.jallcom.2014.06.089.

152. Salvan, C.; Briottet, L.; Baffie, T.; Guetaz, L.; Flament, C. CuCrZr Alloy Produced by Laser Powder Bed Fusion: Microstructure, Nanoscale Strengthening Mechanisms, Electrical and Mechanical Properties. *Mater. Sci. Eng. A* **2021**, *826*, 141915, doi:10.1016/j.msea.2021.141915.

153. Su, Z.; Zhu, Z.; Zhang, Y.; Zhang, H.; Xiao, Q. Recrystallization Behavior of a Pure Cu Connection Interface with Ultrasonic Welding. *Metals* **2020**, *11*, 61, doi:10.3390/met11010061.

154. Zinkle, S.J.; Kulcinski, G.L.; Mansur, L.K. Radiation-Enhanced Recrystallization in Copper Alloys. *J. Nucl. Mater.* **1986**, *141–143*, 188–192, doi:10.1016/S0022-3115(86)80034-4.

155. Bourezg, Y.I.; Abib, K.; Azzeddine, H.; Bradai, D. Kinetics of Cr Clustering in a Cu-Cr-Zr Alloy Processed by Equal-Channel Angular Pressing: A DSC Study. *Thermochim. Acta* **2020**, *686*, 178550, doi:10.1016/j.tca.2020.178550.